Extensible Modeling of Compressed Air Energy Storage Systems

by

Siddharth Atul Kakodkar

A thesis
presented to the University of Waterloo
in fulfillment of the
thesis requirement for the degree of
Master of Applied Science
in
Mechanical Engineering

Waterloo, Ontario, Canada, 2018

AUTHOR'S DECLARATION

I hereby declare that I am the sole author of this thesis. This is a true copy of the thesis, including any required final revisions, as accepted by my examiners.

I understand that my thesis may be made electronically available to the public.

Abstract

There is a growing number of renewable energy sources that can supply power to the electrical grid. These renewable sources of energy are intermittent in nature and therefore the transition from using fossil fuels to green renewables requires the use of energy storage technologies to maintain and regulate a reliable supply of electricity. Energy storage technologies play a key role in allowing energy providers to provide a steady supply of electricity by balancing the fluctuations caused by sources of renewable energy. Compressed Air Energy Storage (CAES) is a promising utility scale energy storage technology that is suitable for long-duration energy storage and can be used to integrate renewable energy (such as Wind energy) to the electrical grid. CAES technologies can be broadly classified into 3 types: Diabatic-CAES (D-CAES), Adiabatic-CAES (A-CAES) and Isothermal-CAES (I-CAES).

The author first performs a review on the different types of energy storage available today and a literature review on of CAES system level models, Turbomachinery models, and cavern models. After the gaps in literature are identified, the author then develops a flexible and extensible model of an A-CAES system, which can be used a CAES plant designer to obtain a first order thermodynamic evaluation of a particular plant configuration. The developed model is scalable, modular and can be connected to a control strategy. The model is able to capture time dependent losses and part load behavior of turbomachinery. The modeling methodology is focused around keeping the model extensible, i.e. components and their fidelity can be easily altered for the model's future growth. The components modeled are the compressor, the turbine, the induction motor, the generator, and a thermal energy storage device to the make the CAES plant adiabatic. The model is created using the Matlab/Simulink® software, which is commonly used tool for modeling.

The A-CAES plant model was simulated for 23.3 hours comprising of 12.47 hours of charging using a mass flow rate of 107.5 kg/s, 8 hours of storage and 2.83 hours of discharge using a mass flow rate of 400 kg/s. The maximum and minimum cavern pressures were 72 bar and 42 bar respectively. The obtained round trip efficiency is 76.24%. Additionally, the turbine start-up time was found to be 760 seconds. The compressor train average efficiency was calculated as 70%, the expansion train average efficiency was calculated as 81% and the TES efficiency was calculated as 91%. The models simulated the behavior of an A-CAES plant accurately with the compressor and turbine showing a close resemblance to their performance maps. The results indicate that Adiabatic-

CAES is a promising and emerging technology. However, further research and development is required beyond this thesis; specifically, in the area of thermal energy storage and management. Finally, the author makes recommendations on how to further improve upon the achieved objectives in this work.

Acknowledgements

I owe a lot to the many people who helped me during my years at the University of Waterloo.

I would first like to thank my supervisor, Dr. Roydon Fraser for mentoring me and allowing me to pursue my interest in both energy systems and hybrid vehicles. I will always be grateful for your unlimited advice and guidance for both my undergraduate 4th year design project, and my graduate studies. I will never forget Dr. Fraser's amazing ability to bring out the best in me, even during the most difficult times. An immeasurable and raucous thank you to you, Dr. Fraser.

I would like to thank my best pal Sunny Akbar Abdul Rehman Tajani for reading and helping me edit this thesis for grammar. You are the *greastest.*

I am grateful to all my team mates at the University of Waterloo Alternate Fuels Team, especially Ramin Shaikhi, Patrick DiGioacchino, and Cole Powers. It was both, an honor and a privilege to work alongside amazing engineers like you. I will always remember our struggles and triumphs together.

I would also like to thank my friends Vivek Jain, Mohamed Chaviwala, Ankit Kumar, Sagar Sachdeva, Rukma Jhildiyal, Brinda Mathew, Ashwin Patro, Urvashi Pal, Sohil Bhambri, and Yasir Qureshi for supporting me throughout my masters program. Thank you for being friends with me, and staying by my side through all my years at university. For this, I will always be grateful.

A special mention goes to Jorge Gonzalez. Thank you for all your help and support.

Last but not least, I would like to thank my mother, Sarita Kakodkar, my father, Atul Kakodkar, and my sister, Simran Kakodkar; for their infinite love and support.

Dedication

To Mumma, Baba, and Simmy. This is for you.

Table of Contents

List of Figures

List of Tables

List of Symbols

A	Area [m^2]
C_p	Specific Heat at Constant Pressure [J/(kg K)]
C_v	Specific Heat at Constant Volume [J/(kg K)]
F	Friction Factor, Force [N]
h_c	Convective heat transfer coefficient [$Wm^{-2}K^{-1}$]
h	Specific Enthalpy [J/kg]
H	Total Enthalpy [J]
I	Moment of Inertia [Kg m^2]
k	Specific Heats Ratio, Square Fit Coefficient
m	Mass [Kg]
$\dot{m}$	Mass Flow Rate [Kg/s]
P	Power [W]
p	Pressure [Pa, bar]
P_r	Pressure Ratio
$\dot{Q}$	Heat Transfer Rate [W]
R	Gas Constant[J/(kg K)]
r	Radius [m]
T	Torque [Nm], Temperature [°C]
t	Time [s, hours]
U	Angular Speed [rad/s]
u	Axial Velocity [m/s], internal energy [J]
V	Velocity [m/s], Volume[m^3]
$\dot{W}_s$	Shaft Power [W]
α	Angle [rad]
η	Efficiency [%]
ρ	Density [kg/m^3]
ω	Angular Speed [rad/s]

Φ	Flow Coefficient
k_r	Thermal Conductivity of rock [$Wm^{-2}K^{-1}$]
Z	Gas compressibility factor
i'_{dr}	D Axis Rotor Current [A]
i_{ds}	D Axis Stator Current [A]
i'_{qr}	Q Axis Rotor Current [A]
i_{qs}	Q Axis Stator Current [A]
L'_{lr}	Rotor Leakage Inductance [H]
L_{ls}	Stator Leakage Inductance [H]
L_m	Magnetizing Inductance [H]
L_m	Magnetizing Inductance [H]
L'_r	Total Rotor Inductance [H]
L_s	Total Stator Inductance [H]
L_s	Total Stator Inductance [H]
p	Number of Pole Pairs
R'_r	Rotor Resistance [ohm]
R_s	Stator Resistance[ohm]
T_e	Electromagnetic Torque [Nm]
T_m	Shaft Mechanical Torque [Nm]
V'_{dr}	D Axis Rotor Voltage [V]
V_{ds}	D Axis Stator Voltage [V]
V'_{qr}	Q Axis Rotor Voltage [V]
V_{qs}	Q Axis Stator Voltage [V]
ϕ'_{dr}	D Axis Rotor Flux [Vs]
ϕ_{ds}	D Axis Stator Flux [Vs]
ϕ'_{qr}	Q Axis Rotor Flux [Vs]
ϕ_{qs}	Q Axis Stator Flux [Vs]

ω_m	Rotor Angular Velocity [rad/s]
ω_r	Electrical Angular Velocity [rad/s]

Suffixes

1	Compressor Inlet, ambient
2	Compressor outlet
3	After TES, entering cavern
4	Exiting cavern, before TES
5	Turbine inlet, after TES
6	Turbine outlet, ambient
isen	*Isen*tropic Process
θ	Tangential
c	Cavern
i	Cavern inlet
e	Cavern outlet
R	Rock
RW	Cavern wall

List of Abbreviations

AC	Alternating current
A-CAES	Adiabatic - Compressed Air Energy Storage
CAS	Compressed Air Storage
CAES	Compressed Air Energy Storage
C-HyPES	Closed Cycle Hydro Pneumatic Energy Storage
D-CAES	Diabatic - Compressed Air Energy Storage
DC	Direct current
ES	Energy Storage
I-CAES	Isothermal - Compressed Air Energy Storage
NaS	Sodium sulfur
rpm	Revolutions per minute
SMES	Superconducting magnetic energy storage
SOC	State of charge
TES	Thermal Energy Storage
O-HyPES	Open Cycle Hydro Pneumatic Energy Storage

Chapter 1
Introduction

In this chapter, the intermittency of renewables to the electrical will be discussed and why there is a need for low carbon energy storage. The different types energy storage technologies available today will also be discussed along with Compressed Air Energy Storage (CAES), its different configurations (diabatic, adiabatic, and isothermal), and why it is worth considering. Furthermore, the Macintosh and Huntorf plants will be reviewed. CAES technology in its current state will be compared with the existing energy storage alternatives. Finally, the thesis objectives and its constituent chapters are stated.

With an increasing human population and demand for higher quality of life, the global electricity consumption is on the rise. The global production of electricity in 2013 reached 23,000TWh per year. Of this, natural gas and other fossil fuels accounted for 68% whereas renewable sources contributed less than 6% [1]. Since the usage of fossil fuels for electricity production comes with associated environmental costs such as climate change, there is an added emphasis for renewables and green technologies to contribute a greater amount to energy production. The main difficulty associated with integrating renewable technologies to the grid is their inherit intermittency. An intermittent energy source can be defined as a source of energy that is not continuously and easily available for conversion into electricity. The intermittency for renewables is mainly caused because of the unavailability of the natural phenomena that causes the generation of energy for that particular renewable source. Table 1 below summarizes the causes for intermittency for various different renewable energy sources. Today, in order to ensure power plants produce the right amount of electricity at the right time to consistently and reliably meet the demand, grid operators utilize a three phase planning process. The amount of electricity supply available is scheduled one day prior, and then balanced with demand on an hour-by-hour and second-by-second basis. Due to the grid having very little storage capacity, a balance must always be maintained between the electricity demanded and supplied. If this balance is not maintained properly, problems such as grid blackout, grid instability, and loss of quality of supplied power may occur [2]. Short term and long term energy storage is considered as one of the prominent solutions to these problems. Energy storage and they can interact with the grid in different ways is discussed in the next subsection.

Table 1 - Intermittency Causes for various Renewable Energy Sources [3]

Number	Name of Renewable Energy Source	Cause of Intermittency
1	Wind	• Wind availability • Wind current concentration • Wind speed • Temperature of Air
2	Hydro	• Water current • Seasonal variations • Precipitation levels
3	Solar	• Amount of diffuse solar radiation • Seasonal variations • Weather conditions • Sun's energy concentration
4	Geothermal	• Uncontrolled drop of temperature • Steam and heat levels

1.1 Energy Storage

Energy storage (ES) technologies play a key role in overcoming the issue of intermittency without a significant carbon footprint. This is accomplished by converting electricity into stored energy in some medium through a conversion device or process. Then, through the same or different conversion device or process, the stored energy is converted back into electricity, losing some energy in the round trip due to process irreversibilities. The goal is capture energy produced at one time, for use at a later time. This is illustrated on the next page on Figure 1.

Figure 1 - Energy Storage Concept [12]

The lack of wide scale adoption of energy storage can be commonly attributed to high costs for energy storage. Whether or not a particular energy storage technology is feasible depends, in part, on if the adoption of the energy storage technology can economically justify the costs and produce an adequate profit [4]. Questions such as "What are the costs?", "What is the expected equipment efficiency?", "How much storage is required to match a given intermittent source?", "How will the energy storage system interact with the grid (load following, peak shaving, arbitrage, spinning reserve, etc.)?"; are to be answered. Factors such as the local regulatory framework, and the time structure of power to be supplied must be taken into account. A full economic model is, however, is beyond the scope of this work. From [5,6, and 18], efficient energy storage solutions provide the following benefits to power utilities:

- Efficient use of renewable energy
- Voltage profile reduction
- Distribution losses reduction
- Renewable energy contribution is maximized
- Improved demand and generation match
- Transmission losses reduction
- Reduction of greenhouse gas emissions
- Improved reliability in the power system
- Reduced stress on the generating system to provide for peak loads

In addition to the above mentioned benefits, an energy storage technology can also provide ancillary services. Ancillary services are defined as "Those services necessary to support the transmission of electric power from seller to purchaser, given the obligations of control areas and transmitting utilities within those control areas, to maintain reliable operations of the interconnected

transmission system." [7]. Table 2, on the next page, defines and summarizes the various different ancillary services that can be provided by an energy storage system to the electrical grid.

Table 2 - Ancillary services and their description

Number	Name of Ancillary Service	Description
1	Frequency regulation	Frequency regulation control refers to the need to ensure that the grid frequency stays within a specific range of the nominal frequency. [8]
2	Load following	Load following refers to balancing the power supplied as the demand for electricity fluctuates through the day (15 minutes to 1 day) [9]
3	Black start	Capability of restarting without consuming electricity from the grid [12]
4	Spinning reserve	The reserve capacity to compensate for unexpected loss in power generation (typically less than 15 minutes) [18]
5	Non-spinning reserve	The reserve capacity to compensate for unexpected loss in power generation (typically greater than 15 minutes) [18]
6	Time shifting/Arbitrage	Store energy when its price is low and discharge energy when its price is high [18]
7	Peak Shaving	Peak shaving is a technique that is used to reduce electrical power consumption during periods of maximum demand on the power utility [10].

By acquiring the capability of storing energy over time, energy providers would need to build power plants with the capacity to meet the average demand for electricity, and not peak demand [27]. This is illustrated on the next page on Figure 2. In the subsequent sections, the various different kinds of energy storage technologies adopted around the world will be discussed along with their advantages and disadvantages.

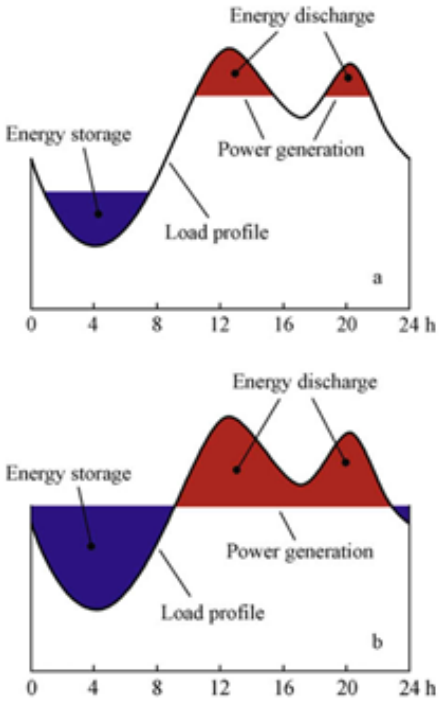

Figure 2 - Load profile of electricity provider showing role of energy storage [18]

1.2 Mechanical Energy Storage

Mechanical energy storage is a means of storing energy in the form of kinetic or potential energy by using a mechanical practice such as compression or rotation [11]. Compressed Air Energy Storage, presented in section 1.6 is also considered as a form of mechanical energy storage. It is worth noting that Adiabatic-CAES (ACAES) utilizes a Thermal Energy Storage (TES) component, while Diabatic-CAES (DCAES) utilizes chemical energy in the form of fuel. The different forms of a CAES system are discussed in section 1.6. The approaches discussed in this section are Flywheel Energy storage and Pumped Hydro Storage.

1.2.1 Flywheel Energy Storage

A flywheel can be described as a rotating disk or wheel, of high mass that can store electrical energy in the form of kinetic energy (rotational mechanical energy). Depending on the speed of rotation, flywheels can be broadly classified into low speed and high speed flywheels. Low speed flywheels operate at speeds lower than 10,000 revolutions per minute (rpm) and provide a shorter energy storage period with high power capacities; while high speed flywheels operate at speeds above 10,000

rpm and provide a longer energy storage period with lower power capacities [13, 14]. Figure 3 below illustrates the cross-sectional view of a flywheel. An electric motor consumes power, and is used to accelerate the flywheel via a shaft when charging. The rotation of the shaft is responsible for transferring angular momentum to the rotor, which is the energy storage component. When discharging, the same electric motor acts as a generator and a deceleration of the rotor is translated into electrical energy. The stored electrical energy is proportional to the mass of the flywheel multiplied by the square of its angular velocity [16].

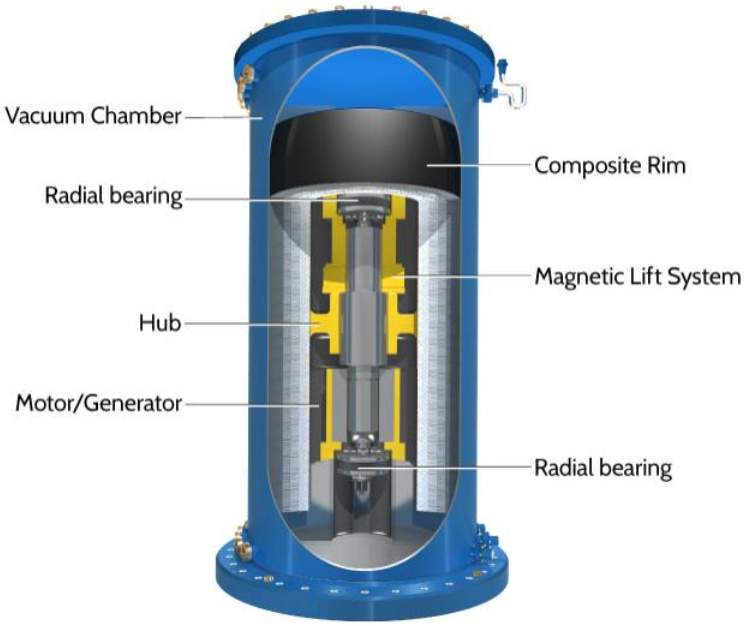

Figure 3 - Flywheel cross section [15]

As an energy storage device, the flywheel was designed to improve power quality by regulating short voltage disturbances, due to its fast response time of less than one second [17,18]. Some of the other key advantages of flywheels are: long lifetime, high number of discharge cycles, environmental friendliness, high round trip efficiency (80-85%), and low life cycle cost [13,14,19]. The main disadvantage associated with flywheels is the incurred energy losses due to bearing friction and windage when attempting long term energy storage. Flywheels typically produce power in the range of a few kW for a couple of hours to 1200 kW for a few seconds [16]. The typical investment cost for a flywheel is 130-500 USD/kW [20].

1.2.2 Pumped Hydro Energy Storage

Pumped hydro energy storage is a commercially proven and mature long term energy storage technology, providing over 95% of the world's current energy storage capacity [16]. There are over 300 pumped hydro plants operating globally [19].

A Pumped hydro plant consists of two water reservoirs located at different elevations, a pump unit to move water from the lower reservoir to the upper reservoir, and a turbine to produce electricity. Energy is stored at Pumped Hydro plant by making use of off-peak electricity to pump water from a lower reservoir to one located at higher elevation. While discharging, water from upper reservoir is allowed to flow downhill while driving a generator in order to produce electricity. In this way, electrical energy can be stored in the form of hydraulic potential energy; and is depicted on the next page in Figure 4. The power produced is proportional to the mass flow rate of water and head of the system. Pumped Hydro plants can be classified into three main categories [24]:

- Closed Loop: comprises of two reservoirs separated by geographic elevation, neither of which are connected to another water body
- Semi-open Loop: comprises of one artificial reservoir and one modified natural water body, such as a lake or a river impoundment, with continuous through flow
- Open System: comprises of two reservoirs where there is continuous flow of water between the upper and lower reservoirs

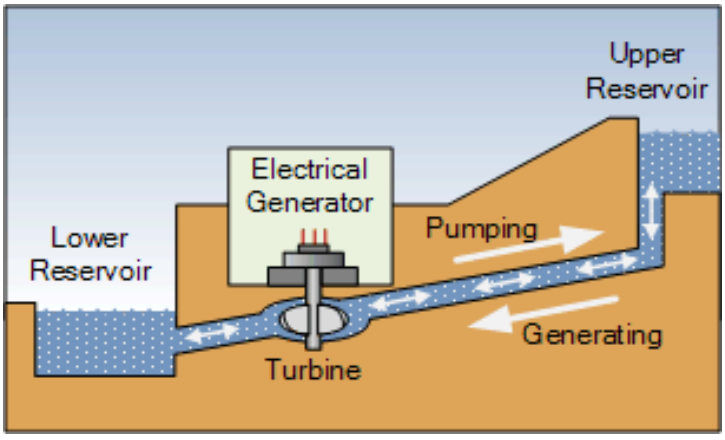

Figure 4 - Pumped Hydro Energy Storage [21]

Pumped hydro plants have severable notable advantages and disadvantages. They have a round trip efficiency range of 70-85% [13,22] and can typically provide power in the range of 100 – 3000 MW

[18]. They also have a relatively short start up time of a few seconds, when on standby; and 10 minutes when completely shut down [22]. Pumped Hydro plants have a flexible operating range, have low operation and maintenance costs, and can be utilized for frequency control, non-spinning reserve, load following and time shifting [23].

Among their disadvantages, Pumped Hydro plants require a long lead time for construction (typically around 10 years) [18], a long construction time, and have a high investment cost of 500-4600 USD/kW [20]. Additionally, the geographical locations that are favorable for Pumped Hydro Storage are scarce, attributing to the fact that Pumped Hydro Energy Storage is an old and desirable energy storage practice. Another limiting factor in the adoption of Pumped Hydro Storage is the environmental damage (large amount of deforestation, acquiring an adequate supply of water, etc.) associated with the construction and operation of a plant.

1.3 Electro-chemical Energy Storage (Batteries)

In Electro-chemical energy storage systems, electrical energy is stored in the form of chemical energy, through either a reversible or non-reversible chemical reaction. The system typically comprises of a large battery that is made up of smaller modules containing repeating units called cells, as shown on Figure 5 below. Its main components are: an anode, a cathode, the electrolyte and an enclosure. During discharge, chemical reactions occur at the cathode and anode that create a flow of electrons through an electric circuit. Electro-chemical energy storage can be classified into four categories namely: primary cell or battery, secondary cell or battery, reserve cell and fuel cell [25,26].

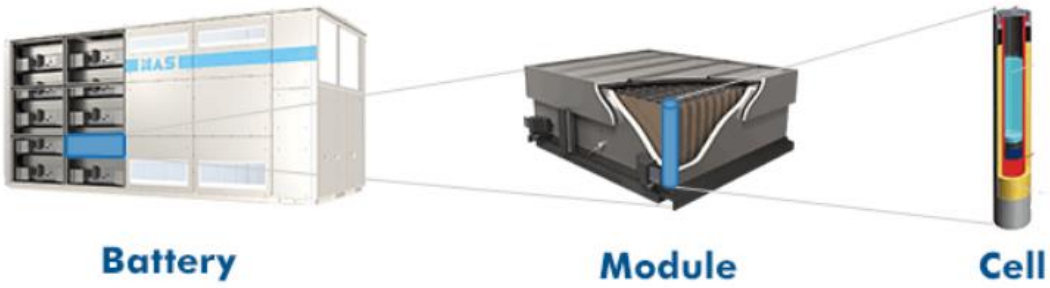

Figure 5 - Battery made up of cells [28]

- A primary battery is non-rechargeable, contains a cathode and anode, and make use of an electrolyte, which is either aqueous or non-aqueous, and enclosed inside a separator or absorbent material.
- Secondary batteries contain the same constituent building blocks as primary batteries, but fundamentally differ because they are rechargeable. To allow for charging, a current can be passed through the circuit that is opposite to the direction of the current during discharge. Secondary batteries use both aqueous and non-aqueous electrolytes.
- Reserve batteries are a type of primary battery used for long term energy storage. They are made without an electrolyte and can be reliably stored under a large variety of conditions. The electrolyte is added just prior to battery discharge
- A fuel cell can produce electricity by using an external supply of a fuel (such as hydrogen) from the anode and an oxidizing agent from the cathode, which react in the presence of an electrolyte. As long as the supply of fuel and oxidizing agent are not exhausted, a fuel cell can continue to operate for a very long period of time. A fuel cell is designed to consume "chemical 1", and produce electricity and "chemical 2"; and can be reversed to consume electricity and "chemical 2", to produce "chemical 1" [18,25,26]

In the subsequent sub-sections, three types of secondary battery energy storage technologies are discussed namely: Sodium-sulfur batteries, Lithium-ion batteries, and Lead acid batteries.

1.3.1 Sodium-sulfur (NaS) battery

A sodium sulfur (NaS) battery consists of molten sulfur at the anode (positive electrode) and molten sodium at the cathode (negative electrode), separated by a solid beta alumina ceramic electrolyte [16]. This is shown on the next page on Figure 6. NaS batteries have a round trip efficiency of 75% and can be used for about 2500-4500 charge cycles before disposal. The typical charge time is about 6-7 hours, with no self-discharge [19]. NaS batteries can provide a power output of 1 to 10 MW for 4-6 hours [28,29]. The typical investment cost of NaS battery is 1420-2500 EUR/kW [18]

NaS batteries are used in commercial electrical energy storage, primarily for grid stabilization and power quality management, because they have a fast (a few milliseconds) response time [19]. One constraint to overcome when using NaS batteries is their operating temperature, of 300-350°C. This requires an initial heat supply, however, once the operating temperature is reached, the heat produced from the chemical reaction during discharge is sufficient to keep the process running [34].

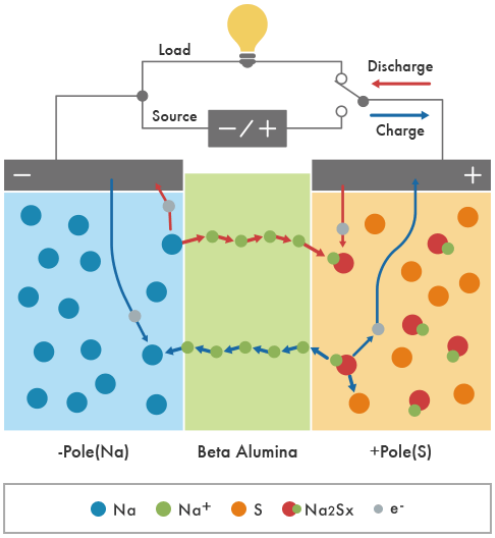

Figure 6 - NaS Battery [28]

1.3.2 Lithium-ion battery

Lithium ion batteries were first proposed in the 1960s, and then commercially produced by Sony in 1990 after Bell Labs developed a workable graphite anode as an alternative to the lithium metal [18]. The cathode is made of a lithiated metal oxide ($LiCoO_2$, $LiMO_2$, etc.), the anode is made of graphitic carbon, and the electrolyte is made of lithium salts [18,30].

Although Lithium ion batteries dominate the market for portable electronics and medical devices [31], they can be used in smaller energy storage applications. They have a very high round trip efficiency of 85-98% [19] and have a high energy density range of 90-190 Wh/Kg [32]. This property, combined with a low self-discharge rate, makes Lithium-ion batteries a very attractive energy storage option for electric vehicles [33]. Lithium-ion batteries can be used for 1000-10000 charge cycles [19] and its power output is 1kW-1MW for a discharge time of 1-4 hours [16]. Lithium-ion batteries have several disadvantages that prevent their usage in large scale energy storage applications [16]. They require additional safety circuits to protect against overcharging, which are expensive [19, 34], and their lifetime is significantly reduced when operating at high temperatures or when discharged beyond a certain extent [16].

1.3.3 Lead acid battery

Lead Acid batteries were invented in 1859 and are the oldest and most widely used secondary batteries for household, as well as industrial applications. A lead acid battery is made up of lead-

dioxide, which acts as the positive electrode; and metallic lead, which acts as the negative electrode. The electrolyte made of 37% (5.99 Molar) sulfuric acid [18]. The round trip efficiency of a lead acid battery is 70-90% and its investment cost is 300-600 USD/kWh. This makes lead acid batteries a popular choice in some automotive, power quality, and spinning reserve applications [18]. They can also achieve a power output of 0-30 MW [25]. However, there are certain disadvantages associated with using Lead acid batteries, such as their low energy density of 30Wh/Kg [32]; and low cycle life of 500-1000 charge cycles [18]. They also require a thermal management system because they cannot perform well at low temperatures [18].

1.4 Chemical Energy Storage

Chemical energy is stored in the form of chemical bonds within and between atoms and molecules of substances. This energy can be released when the substance undergoes a chemical reaction, often resulting in the substance changing forms, or transforming into an entirely new substance. Chemical fuels such as coal, gasoline, hydrogen, butane, ethanol, etc. are responsible for carrying chemical energy [25]. Alternatively, chemical energy can be released by electron transfer reactions for the direct electricity generation [35]. The Electro-chemical technologies discussed in section 1.3 also fall under a category of chemical energy storage, however, the following subsections will discuss chemical energy storage from the perspective of fuels, specifically hydrogen and methane. Chemicals such as Butanol and Ethanol are also considered for energy storage however since they are produced through techniques such as fermentation of biomass, they are not considered as electrical energy storage. Methane is discussed because it is 3 times cheaper to store relative to hydrogen [37].

1.4.1 Hydrogen

Hydrogen is an abundant, transportable, non-toxic and versatile energy carrier, with an energy density of 142 kJ/Kg, which is higher than other hydrocarbon based fuels [36]. Hydrogen can be produced by a process known as electrolysis using off-peak electricity. It can also be produced from coal, biological materials, natural gas and heavy oils [37]. Figure 7 on the next page illustrates the electrolysis process, which is the process by which water breaks down into hydrogen and oxygen gas with the help of an electric current.

The hydrogen produced through the above mentioned methods can be stored physically, in gas or liquid phase, or by using material based storage. In the gas phase, hydrogen can be stored in high pressure vessels or salt caverns at pressures of 300-700 bar. Hydrogen storage in the liquid phase

requires cryogenic cooling because of its low boiling point of -252°C. Material based hydrogen storage is done on metal hydrides or sorbent materials [25,38].

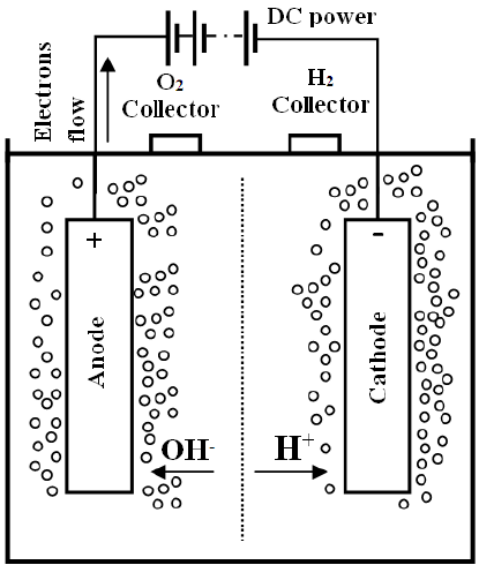

Figure 7 - Electrolysis of Water [38]

Stored hydrogen can be used to generate electricity by being burnt in an internal combustion engine or a turbine. It can also be used in fuel cells, which have a higher efficiency [25]. The typical round trip efficiency of hydrogen storage is about 20-45% [19]. The typical power output is 1-500 MW [16] and the typical investment cost is high, about 1000-2000 USD/kW [39].

1.4.2 Methane

Methane is one of the chemical compounds that is considered for energy storage applications. When liquefied, methane is easy to store and transport. Since methane has a higher energy density and higher boiling point relative to hydrogen, it becomes 3 times cheaper to store than hydrogen [37].

Methane is typically produced by Sabatier's reaction, which is a two-step reaction involving hydrogen gas and carbon dioxide. In the first step, carbon dioxide reacts with hydrogen to produce carbon monoxide and water. In the second step, carbon monoxide reacts with hydrogen to produce methane and more water. The reaction requires a supply of carbon dioxide, making the reaction expensive, and a temperature range of 200 -750°C. The efficiency of the reaction is 70-85% [16] and the round trip efficiency from hydrogen production is 20-30% [37].

1.5 Electrical Energy Storage

In this section, methods to store energy in the form of electrical energy will be discussed. They can largely be classified into two categories: electrostatic (capacitors and supercapacitors) and magnetic (or current) energy storage [25]. The technologies in particular that are discussed in this section are Superconducting magnetic energy storage (SMES) and Supercapacitors.

1.5.1 Superconducting magnetic energy storage (SMES)

Superconducting magnetic energy storage (SMES) systems store energy in the form of an electric current that is passed through a coil made from superconducting material. The energy is stored in the circulating electrical current with almost zero loss [18]. A superconducting material exhibits zero electrical resistance when cooled below a critical temperature [40]. The coil must be immersed in liquid helium inside a vacuum insulated cryostat in order to remain in a superconducting state. The key components of a SMES system are: the superconducting coil, a cryogenic refrigerator system, a vacuum insulated vessel, and an AC/DC converter; as shown below in figure 8. The conducting coil is typically made of niobium-titanium, and the coolant can be liquid helium at 4.2 K, or super fluid helium at 1.8 K [18].

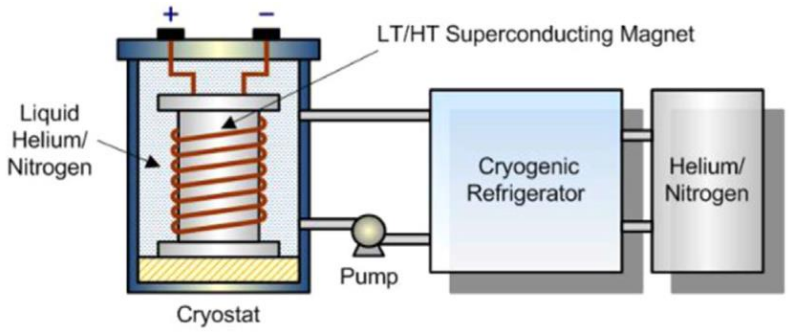

Figure 8 - Components of a Superconducting magnetic energy storage system[41]

SMES systems have a high round trip efficiency of up to 95% and can produce a power output of 1-10MW. They also have a fast response time and long lifetime (30 years); making them an ideal option to improve the power quality in the gird [16,23].

Some of the disadvantages associated with SMES systems are their high capital investment (about 7200 USD/kW) and high self-discharge rate of about 10-15% per day [23]. Furthermore, there are negative environmental consequences of having such strong electromagnetic fields generated [16].

1.5.2 Supercapacitors

Supercapacitors and capacitors are the most direct and literal approach to storing electrical energy [25]. In its simplest form, a capacitor is made of two metallic plates separated by a non-conducting layer, known as the dielectric. When charging, one of the plates is charged using electricity from a direct current source. An opposite sign charge is then induced on the second plate [18]. In a supercapacitor, the dielectric is replaced with an electrolyte solution in between the two conducting plates, usually about 1 molecule thick; and is the means by which supercapacitors store energy. The electrodes are made from porous carbon and have a high surface area of up to 2000 m^2 per gram of carbon. Due to this, supercapacitors are able to have very high capacitances (relative to conventional capacitors) and store large quantities of energy [18,25]. Figure 9 on the next page illustrates the structure of a supercapacitor.

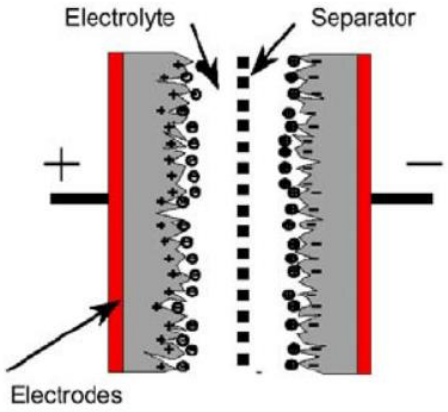

Figure 9 - Structure of a supercapacitor[42]

When compared to traditional batteries, Supercapacitors have a lower energy density but have a higher power density; and operate with round trip efficiency of 80-95% with about 5% daily self-discharge [19,43]. This means the stored energy must be used quickly in order to not accumulate large losses, making supercapacitors not ideal for long term energy storage. However, they have a fast response time, and can produce a power output of 100-250 kW, making them an ideal option for frequency regulation [16]. Additionally, supercapacitors have a long lifetime, being able to operate for over 100000 charge cycles [16]. The investment cost for supercapacitors is 6000 USD/kWh [23].

1.6 Compressed Air Energy Storage (CAES)

Compressed Air Energy Storage (CAES) is a form of mechanical energy storage. Apart from Pumped Hydro Energy Storage, CAES is one of the few desirable energy storage options that has a power output on a similar scale (100-1000 MW) [12]. In this section, Compressed Air Energy Storage, a brief history, and its different variations will be covered.

1.6.1 A Brief History

Compressed air, as an energy carrier, has been used in the manufacturing industry for many years. It is used for purposes such as drilling, carving, cleaning, etc. Fundamentally, the idea to store electrical energy in the form of compressed air dates back to the early 1940s [44]. However, at the time, the need to store the energy in the electrical grid was lacking. In the 1960s, the introduction of baseload power generation in the form of nuclear power and lignite coal fired power, lead to the formation of an economic case for storing off-peak power [45]. It was realized that inexpensive off-peak power could be stored and used later during the hours of peak load; and the stored power would be generated using the same baseload power plants. Where applicable, this gap was bridged using pumped hydro energy storage [45].

In 1969, the decision to develop and build the first CAES plant in northern Germany was taken. The plant would be named “Huntorf”. The suitable geology for underground salt caverns and the need for grid energy storage were the driving factors. Additionally, this CAES plant would be capable of providing black start for the German electrical grid [45,46].

After the inception of the Huntorf plant in Germany, there was a rise in the interest levels for CAES in the mid-1970s [44]. The US Department of Energy initiated an R&D and pre-demonstration program for CAES in the late 1970s, at the end of which, Diabatic-CAES (D-CAES) was considered technically feasible [47]. In 1991, the first CAES plant in the US was built in Alabama at the McIntosh site [48]. A detailed review of both the McIntosh and Huntorf plants is presented in sections 1.6.4 and 1.6.5 of this work respectively.

Despite the rising interests and initiatives for CAES, there have not been any large scale CAES plants that have been constructed after the McIntosh plant. A few decades ago, the driving factors behind the development and deployment of CAES were black start capability and the economic optimization of transferring baseload power to peak hours. Today, the main driving factor are the

balancing of intermittency from renewable energy sources, and providing different ancillary services [45]. Figure 10 below shows the timeline of CAES inception and development through the years.

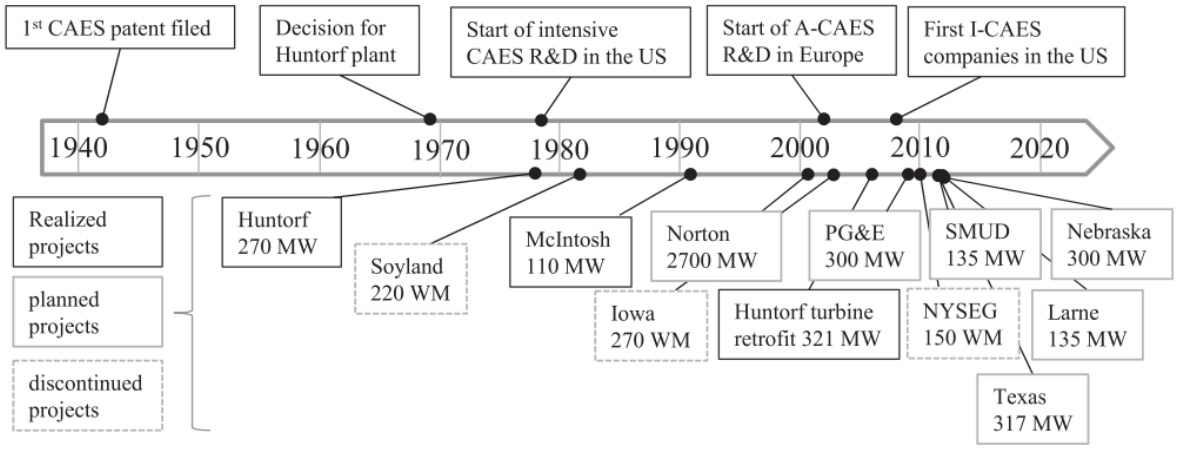

Figure 10 - CAES Development timeline [45]

1.6.2 Basic Principles of CAES

A CAES plant comprises of the following components:

- Electric motor and generator
- Multi-stage compressor train
- Above ground or underground compressed air storage (CAS)
- Expander train
- Piping and fittings
- Control system

At a conceptual level, the basic principles of CAES are simple. Electricity from the grid is used to drive an electric motor, which in turn, drives a compressor to pressurize ambient air. This pressurized air is then stored in a container of large volume; and can be released when needed. Electrical energy is stored in the form of potential energy of pressurized air. Power is generated by the expansion of the compressed air through an air turbine, which is connected to a generator. Figure 11 on the next page illustrates this.

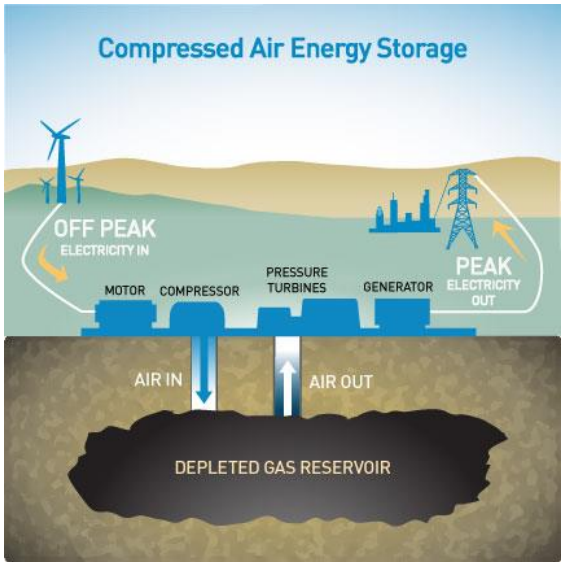

Figure 11 - Generic Compressed Air Energy Storage Diagram [49]

There are a variety of CAES concepts that exist today. These are at different stages of development, have different strengths and weaknesses, and are aimed at different applications. Broadly speaking, CAES technologies can be classified into 3 types: Diabatic-CAES (D-CAES), Adiabatic-CAES (A-CAES) and Isothermal-CAES (I-CAES). Figure 12 shows the different CAES technologies.

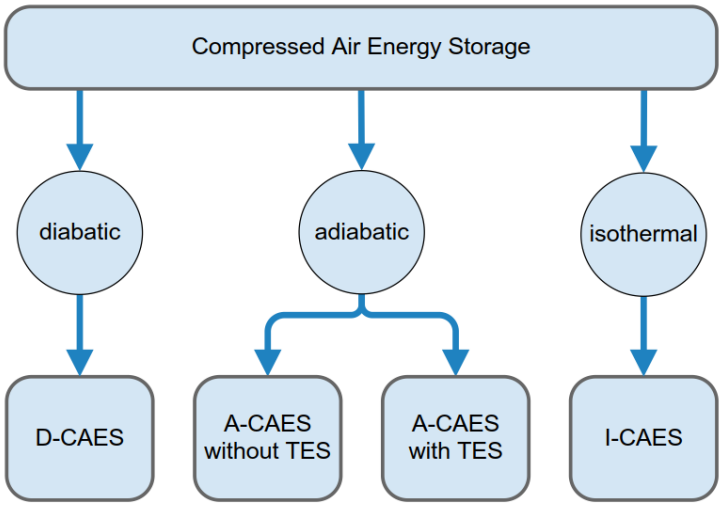

Figure 12 - Classification of CAES technologies [45]

The main principle used to distinguish between the different CAES types is how the heat is handled during compression and before the expansion of air. In the subsequent paragraphs, these technologies are discussed along with how the heat is handled in each configuration.

1.6.1 Diabatic-CAES

D-CAES is the only type of CAES that has been realized on a large scale [45]. Figure 13 below shows the schematic of a D-CAES plant. When a D-CAES plant is in charging mode, ambient air is compressed by a compressor that is electrically driven. The air is cooled using intercoolers in between compression stages. After the air exits the compressor it is cooled further before it enters the compressed air storage (CAS) device. The removed heat is not re-used in the process further and can be considered waste. The heat removed enables the safe operation of the CAS and reduces the specific work of higher order compressor stages. When in discharge mode, air is removed from the CAS and heated in a combustion chamber with the help of burning a fuel such as natural gas. After being heated, the air is allowed to expand and drive a turbine that is connected to a generator and can produce electricity [50].

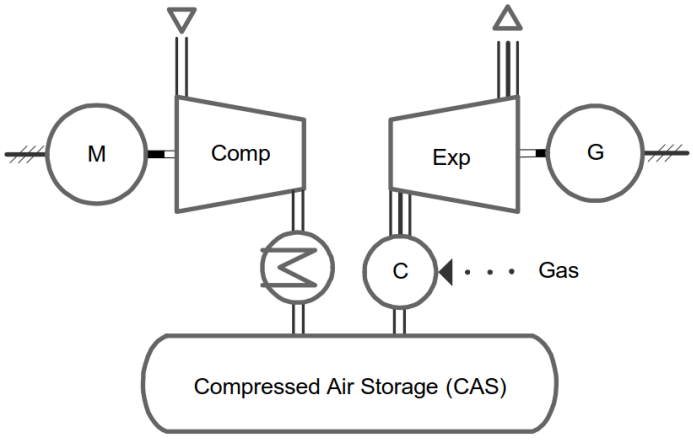

Figure 13 - Diabatic-CAES [50]

1.6.2 Adiabatic-CAES

A-CAES is similar to D-CAES in this operation. However, in an A-CAES plant, after the air is compressed, the heat from compression is not wasted, but is stored. In one type of A-CAES, the heat is stored in a thermal energy storage (TES) device. The same heat is then used to reheat the air before expansion in the turbine. In this way, the need for combustion and the usage of fuel in the process is completely eliminated. There is also a second type of A-CAES that does not use a TES. Here, the compressed air is used for both, potential energy storage as well as thermal energy storage. Again, no fuel is used in the entire process. However, the imposed requirement of the CAS to be able to sustain large temperatures and pressures leads to large initial costs and safety considerations. Thus far, no A-CAES systems have been realized on a commercial scale [50]. Only laboratory scale A-CAES

systems exist currently [51]. Figure 14 below, shows the schematic of A-CAES plants with and without a TES. There is a type of CAES system which combines the use of a combustion chamber and TES, called hybrid CAES [52].

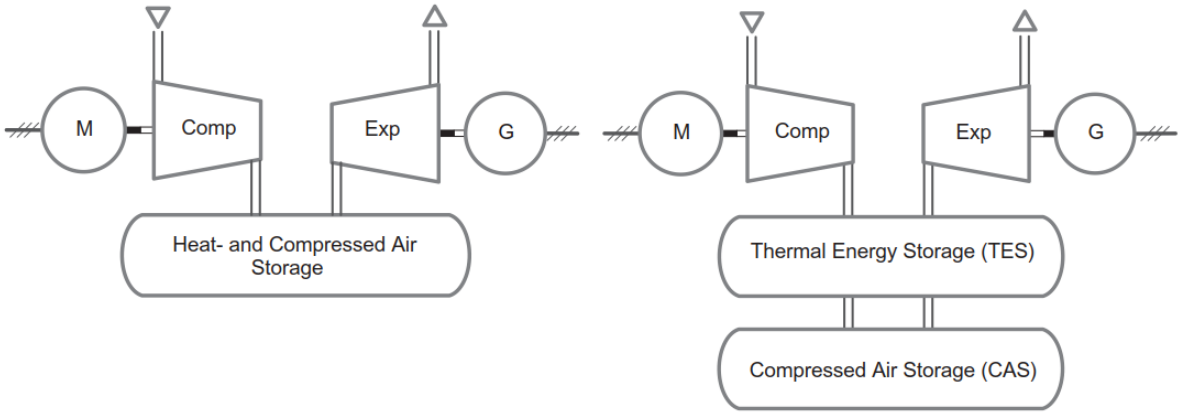

Figure 14 - A-CAES with and without TES [50]

1.6.3 Isothermal-CAES

I-CAES plants attempt to prevent the rise in temperature during the compression or charging process and the drop in temperature during the expansion or discharge process. All I-CAES concepts developed thus far are based on piston machinery. This is because piston machinery can perform a relatively slow compression or expansion process, which provides more time to facilitate heat transfer within the machinery itself. All I-CAES concepts, such as Closed Cycle Hydro Pneumatic Energy Storage (C-HyPES) and Open Cycle Hydro Pneumatic Energy Storage (O-HyPES) are currently only developed at a laboratory scale [45]. Table 3 below provides a comparison of technical parameters for the three types of CAES systems discussed in the previous subsections.

Table 3 - Comparison of technical parameters of different CAES types [45,50]

Parameter	**Diabatic**	**Adiabatic**	**Isothermal**
Round trip efficiency (%)	0.54	0.7	0.38
Energy density (kWh/m^3)	2-15	0.5-20	1-25
Startup time (min)	10-15	5-15	<1
Power output range	5MW-1GW	1MW-1GW	5kW-1GW
Development Status	Application/Demonstration	Research/Demonstration	Research

1.6.4 Huntorf

The Huntorf plant began operating in 1978 and was the first CAES plant in the world and is a D-CAES system. When charging, ambient air is compressed to a pressure of 72 bar using two turbo-compressor units with intercooling between them. The CAS devices are two solution mined salt caverns, with a cumulative volume of 310,000 m^3. Having two caverns allows for continued plant operation, even when maintenance work is to be performed on one of the caverns. For safety reasons, the caverns are cycled between 46 and 72 bar. When discharging, the air leaving the cavern is first throttled down to 42 bar with the help of valves before entering the high pressure combustion chamber and high pressure turbine. Throttling the air pressure results in a loss of energy but allows for the constant pressure efficient operating of the turbine. Air is expanded to about 10 bar after the high pressure turbine. After this, the air is heated again in a low pressure combustion chamber and made to expand further in a low pressure turbine [45]. Figure 15 below shows an aerial view of the Huntorf plant.

After 28 years of operation, in 2008, the expansion train of the Huntorf plant was retrofitted. The retrofits allowed for the inlet temperature of the high pressure turbine to be lowered from 550°C to 490°C. Furthermore, the temperature and pressure of the low pressure combustion chamber were increased from 10 bar to 13 bar, and from 825°C to 945°C respectively. This allowed the power output to be increased from 290 MW to 321 MW [53]. Being the first of its kind, the Huntorf plant had implemented within it, some unique features for the first time [53]:

- Compressed air storage in solution mined caverns
- High pressure combustion chamber
- High pressure expansion turbine and gas turbine with fast start up capability
- Power ratio in the motor/generator being one to five

Figure 15 - Huntorf CAES plant [54]

1.6.5 McIntosh

The McIntosh plant was constructed in 1991 in Alabama, USA, 13 years after the construction of the Huntorf plant. It was the second commercial D-CAES plant in the world. The basic arrangement of components is similar to that of Huntorf, however, only one salt cavern, of size 538,000 m^3, is used as the CAS device. The McIntosh plant has multi-stage compression with intercooling and no TES (Thermal Energy Storage) device for heat storage. The plant also uses an exhaust-heat recuperator, which uses the heat from the air exiting the low pressure expander, which is at about 370°C, to preheat the air coming out of the cavern [45]. The overall round trip efficiency of the McIntosh plant is 54%, higher than the Huntorf plant, which has a round trip efficiency of 42%. This can be attributed to the recuperator installed at the McIntosh plant as well as the advancement in the technology of the turbomachinery and other components used [45]. Table 4below compares the key parameters between the Huntorf and McIntosh plant.

Table 4 - Comparison between Huntrof and McIntosh [45]

Parameter	**Huntorf**	**McIntosh**
Round trip efficiency (%)	0.42	0.54
Energy content (MWh)	642	2640
Planning – construction – commissioning	1969-1978	1988-1991
Compressor manufacturer	MAN Turbo	Dresser-Rand
Max input power (MW)	60	50
Max charging air flow rate (Kg/s)	108	90
Number of compressor units	2	4
Charging time at full load (hours)	8	38
Cavern pressure range (bar)	42-72	46-75
Cavern volume (m^3)	310,000	538,000
Turbine manufacturer	Alstorm	Dresser-Rand
Max output power (MW)	321	110
Output control range (MW)	100-321	10-110
Startup time – normal/emergency (min)	14/8	12/7
Max mass flow rate (Kg/s)	455	154

1.7 Summary of energy storage technologies

Table 5 below summarizes the various different energy storage technologies covered in this chapter. From the table it can be seen that CAES is a promising long term energy storage technology. Two of the most common drawbacks associated with CAES technology is its low round trip efficiency and the requirement of a suitable site for an underground cavern. However, with the emergence of A-CAES technologies having higher round trip efficiencies and the development of above-ground air storage technologies, these barriers can be overcome in the near future.

Table 5 - Summary of different energy storage technologies [13,14,16-20,22-29,37,39,43]

Technology	**Investment cost**	**Round trip efficiency**	**Scale**	**Storage Periods**	**Usage**
Flywheel Energy Storage	130-500 USD/kW	80-85%	Small scale	Short	Frequency regulation, black start
Pumped Hydro Storage	500-4600 USD/kW	70-85%	Large scale	Long	Load following, frequency regulation, non-spinning reserve, load following, time shifting, peak shaving
Compressed Air Energy Storage	500-1500 USD/kW	42-54%	Large scale	Long	Load following, frequency and voltage regulation, spinning reserve, time shifting, peak shaving, black start
Sodium-Sulfur Battery	1420-2500 EUR/kW	75%	Small scale	Short	Grid stabilization, load following, black start
Lithium-ion Battery	-	80-98%	Small scale	Short/ long	Frequency regulation
Lead acid Battery	300-600 USD/kW	70-90%	Small scale	Short	Grid stabilization, spinning reserve
Hydrogen	1000-2000 USD/kW	20-45%	Large scale	Long	Load following, time shifting, fuel, heating
Methane	-	20-30%	Large scale	Long	Load following, time shifting, heating
Superconducting Magnetic Energy Storage	7200 USD/kW	95%	Small scale	Short	Grid stabilization, load following
Supercapacitors	6000 USD/kW	70-80%	Small scale	Short	Frequency regulation

1.8 Objective

The main objective of this thesis is to develop a flexible and extensible model of a CAES system for bulk applications, that is dynamic and modular. The model must be capable of capturing time dependent losses and part load behavior of turbomachinery. The model can be used a CAES plant designer to obtain an accurate first order thermodynamic evaluation of a proposed CAES plant. For the purposes of this work, the CAS chosen to be modeled is an underground cavern, since it is a proven CAES component for bulk applications. The designer can configure the turbomachinery and cavern as desired, without the need to develop a system of equations to describe the underlying physics. The developed models are scalable, modular and can be connected to a control strategy. The modeling methodology is focused around keeping the model extensible, i.e. components and their fidelity can be easily altered for the model's future growth. The models should be able to accurately simulate the behavior of a CAES plant, or any of its constituent components, for a variety of scenarios.

1.9 Thesis Outline

This thesis is divided into six different chapters.

Chapter 1 provides a motivation for energy storage by discussing the intermittency of renewables to the grid. Furthermore, different energy storage options for the grid discussed, compared and contrasted with CAES.

Chapter 2 comprises of a review of published literature of CAES system level models, Turbomachinery models, and cavern models as well as the methodology incorporated.

Chapter 3 contains the details of the methodology of how the different components of a CAES system are modeled. The solving sequence for each component is also presented.

Chapter 4 details how the different components presented in chapter 3 are connected together in a modular and extensible system-level CAES model.

Chapter 5 presents the results obtained from simulating the models presented in Chapters 3 and 4. Results are obtained for 23.3 hours of simulation comprising a of a charging period followed by a storage and discharge period.

Chapter 6 discusses the main conclusions obtained from this work and makes recommendations for future work.

Chapter 2
Literature Review

In this chapter, the various different CAES models published in literature will be reviewed. Since one aim of this work is to capture transient effects within the system components, dynamic models of turbomachinery and the cavern, which form integral parts of a CAES system, published in literature will also be discussed.

2.1 CAES Modeling

The first CAES program found in literature by the author is from [55], published in 1982. An overall plant model is developed in FORTRAN in order to predict the cycle efficiencies of various CAES plant layouts. One year later, the same author published a paper on the thermodynamic analysis of five different CAES cycles including one A-CAES cycle [56]. The program being stationary in nature, are not able to capture the dynamics effects within the system such as varying turbomachinery efficiencies and storage losses.

The authors in [57] propose a model of a CAES plant for transient stability studies. The components modeled include a compressor, a turbine and an induction machine which acts as the motor and generator. The turbine is modeled as a linear function of the fuel and rotor speed and the compressor is modeled as a reciprocating cylinder with a moving piston. The model is tested on simplified single load machine for a variety of contingency scenarios such as load shedding and load change. In the simulation, rotor shaft dynamics are captured when the plant is charging, and power delivered to the grid is captured when the plant is discharging. The authors conclude that the models can be used for steady state and dynamic analysis. However, pressure and temperature changes in the cavern and their effect on the system are not modeled and included. Furthermore, the models do not account for the masses within the turbomachinery and limit the capability of the CAES plant to only perform voltage control.

In [58], a CAES system connected to a wind farm is modeled using Matlab/Simulink®. The compressor and wind turbine are modeled as steady state machines and an induction motor is dynamically modeled and is mechanically connected by a shaft to the wind turbine. Studies are performed where different torques are applied on the induction motor at different times by the wind farm; and the dynamic response of the induction motor is studied. The results note that the proposed arrangement is applicable to CAES because the electrical torque in the induction motor can be

controlled for positive or negative step changes in the mechanical torque; for charging as well as discharging. There are certain limitations in this work, the key limitation being the absence of a turbine model. Additionally, the thermodynamics of the turbomachinery and their effect on torque is not considered.

In [59], a CAES system is modeled to smoothen the power delivered by a 2MW wind turbine to the grid. The components modeled are the motor, compressor, heat exchanger, turbine and synchronous generator. The overall system is setup such that the wind turbine is connected to the grid through an ac/dc converter, a dc link, and a dc/ac inverter. The CAES system, through the dc link, acts as a buffer for the captured wind energy. The CAES components are modeled using thermodynamic relations, including the air storage. It is found in the results that the power delivered by the hybrid system is greater than the power delivered by the wind turbine by itself. That being said, the motor and generator models were not presented as part of the work and hence their fidelity cannot be determined. Furthermore, the effect of rotating masses in turbomachinery and the charging state of CAES system was not modeled. The interaction between the generator and the ac/dc converter as well as the dc/ac inverter are ignored.

In [60], a dynamic model for a CAES plant and supercapacitor is presented to absorb power from the grid. The methodology for the modeling of the air storage, permanent magnet, synchronous generator, compressor, supercapacitor, converters and control system are presented. The operation is such that the supercapacitor absorbs the difference in power between what is output by the CAES system and the demanded power. An additional algorithm is introduced to enhance the compressor operation by regulating the available pressure in the air storage device. Although the results can be considered reasonable, the simulation is only useful for studying hybrid CAES systems involving supercapacitors. Furthermore, again, the models do not account for the rotating masses within the turbomachinery and their drivers.

In [61], a thermodynamic analysis of a CAES system is presented. Modeling, on the basis of steady state equations, for compressor, air expander, heat recuperator, burner is discussed. The system is setup such that the air expander is in series with the gas turbine. A sensitivity analysis is performed for the system at nominal and off-nominal values. Results show that when the air mass flow rate is at nominal values, and there is partial loading, the efficiency of the air expander and gas turbine drops. Additionally, the efficiency of the air expander and gas turbine remain relatively constant when the input air temperature of the gas turbine is fixed to the nominal value. Lastly, the results show that the

efficiency of the gas turbine shows higher values at nominal conditions as compared to off-nominal conditions. Although the conclusions drawn are reasonable, the proposed system is different from typical CAES systems for bulk applications. Furthermore, the authors did not model an air storage device.

The research performed in [62] shows a dynamic thermodynamic analysis for an A-CAES system. Transient models for the low and high pressure compressor, low and high pressure turbine, packed bed TES, and heat exchangers is presented. Equations to evaluate component level performance and system level performance is presented. It is shown that the thermal front degradation within the TES has an influence on the overall plant efficiency. The model simulates the dynamic performance of a CAES plant for both design and off-design conditions for a number of charge cycles. Absent from this work is the models for the motor and generator. Inertias present in these machines will have an influence on the overall results.

[63], [64], [65], [66] present low fidelity modeling of CAES systems for a number of situations. However, these models are either not dynamic, or make a number of assumptions that reduce the confidence in the conclusions drawn and are hence not incorporated in this work. [67], [68], [69] present CAES modeling for small scale applications. However, the turbomachinery, storage equipment, and electrical equipment used are not feasible for bulk CAES applications and are therefore also not incorporated in this work.

2.2 Turbomachinery Modeling

Modeling turbomachinery components within a CAES system accurately is an important objective in this work. It is important that the models take into account the inertias of rotating masses within the machines and are not developed on the basis of thermodynamic relationships alone. In literature, there is an abundance of models published for modeling gas turbine turbomachinery. These models can be broadly classified into two types: models based on the frequency domain and control theory [70], [71]; and models based on time domain [72], [73], [74]. The models that are created in the time domain use the time-differential versions of momentum, mass and energy conservation as the basis for the model. In order to solve the equations, performance data specific to the turbomachine needs to be obtained. This data is obtained from one of two sources: directly from the manufacturer, or by using compressor and turbine performance maps. These maps are discussed in more detail in section 2.2.1 of this work.

All the available literature on turbomachinery modeling requires that the compressor and turbine are connected by a common shaft. This connection is also built into the developed models of the turbine and compressor and the performance of one of these components has a significant influence on the other. This is not the case for CAES systems, where the turbine and compressor operate independently of each other. Therefore, the turbomachinery models have to be modified slightly in order to better represent CAES operation. This modification is better achieved when working with time domain models in contrast to frequency domain models.

The research presented in [75] models turbomachinery components using performance maps for CAES applications. The models for the compressor, turbine, and generator are presented. The models also make use of a regulating system, which ensures the compressor and turbine operate on a safe region on the performance map without risk of surge or stall. The beta lines approach is used for reading data from the performance maps. The author aims to simulate a charge and discharge cycle of the Huntorf plant and the results are considered reasonable. The models capture the real performance of the turbomachines well for CAES purposes but lack a connection to an air storage device.

2.2.1 Turbomachinery Maps

Turbomachinery maps are a representation of the phenomenon occurring in a turbomachine. They contain all information pertaining to the real operation of the machine and can be used to model its behaviour. They are created typically by the manufacturer of the machine by conducting expensive tests in laboratories. It is for this reason, that these maps are sometimes difficult to acquire, given that they contain information that is considered confidential by the manufacturer. A typical map contains performance data of the turbomachine at different conditions of angular speed, pressure ratio, mass flow rate and its consequence on machine efficiency [75].

Compressor maps are of two types: maps containing information regarding pressure ratio and mass flow rate; and maps containing information regarding mass flow rate and efficiency. Both types of maps contain information for machine angular speed. Figure 16, on the next page, shows a typical compressor map. The first map contains mass flow rate on its x-axis and pressure ratio on its y-axis. The second map contains mass flow rate on its x-axis and isentropic efficiency on its y-axis. Both maps contain curves which represent constant angular speeds that the compressor can operate at. On the first map, the lines of constant angular speed are limited by the stall line on the right hand side, and by the surge line on the left hand side. The surge and stall concepts are explained in section 2.2.2 of this work. It can be noted that the presented compressor maps do not contain information for

speeds below 50% of its nominal speed. This is because the operation of the compressor becomes unstable at these low speeds and it is difficult to obtain useful data. Compressors are designed to operate at speeds higher than 50% of their nominal speed [76]. In literature, compressor maps are also found where all the above mentioned information is represented on one plot. On such a map, the pressure ratio is on the x-axis, mass flow rate is on the y-axis, and lines of constant speed are present. The isentropic efficiency is represented as contours on the map. Figure 17 below provides an example of such a map.

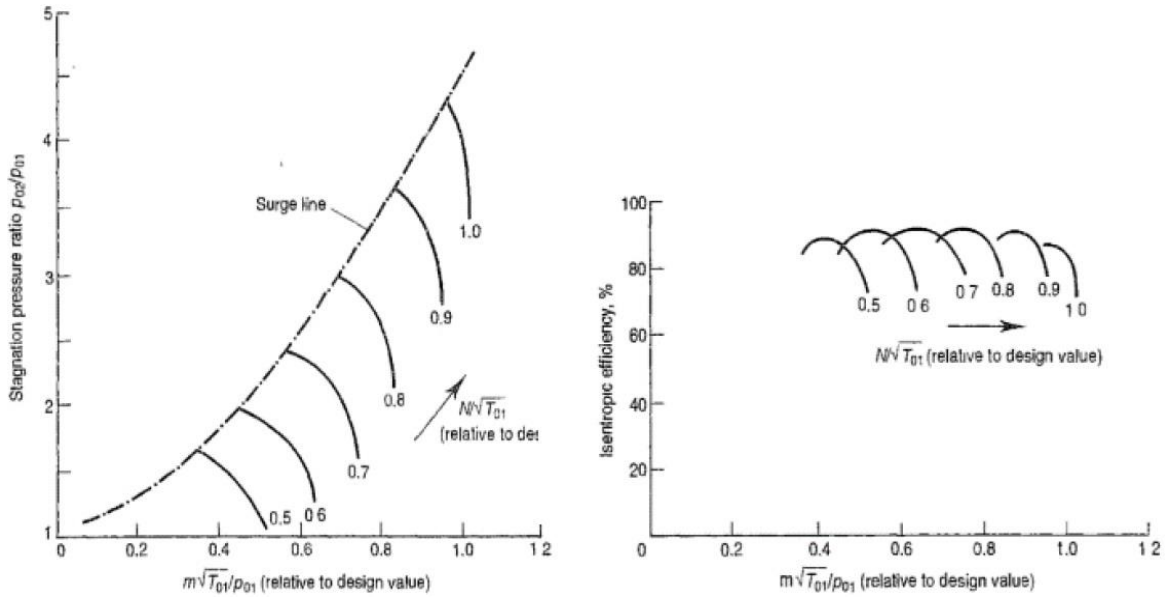

Figure 16 - Typical Compressor Map [77]

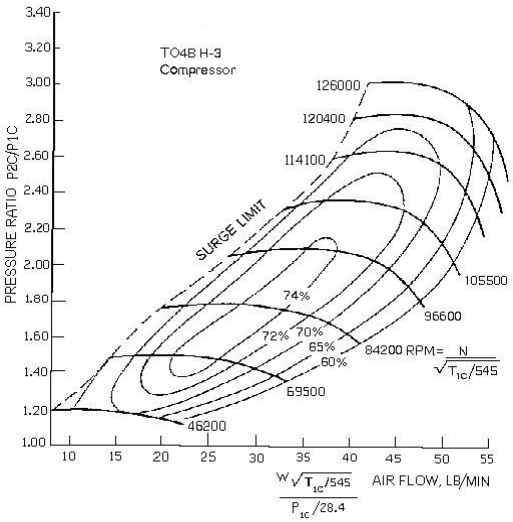

Figure 17 - Compressor map with efficiency contours [78]

Turbine maps, similar to compressor maps, also are of two types: maps containing information regarding pressure ratio and mass flow rate; and maps containing information regarding mass flow rate and efficiency. Turbine maps contain pressure ratio on the x-axis, and mass flow rate and isentropic efficiency on the respective y-axes. Curves of constant speed are also present on the map. Typical turbine maps are shown below in Figure 18. It is important to note that in the turbine map, all the lines of constant speed converge after a certain pressure ratio is attained. This happens because the stator in the turbine gets choked, and therefore, no additional mass flow rate can be added despite an increase in angular speed. The concept of turbine choking is explained later on in section 2.2.2.

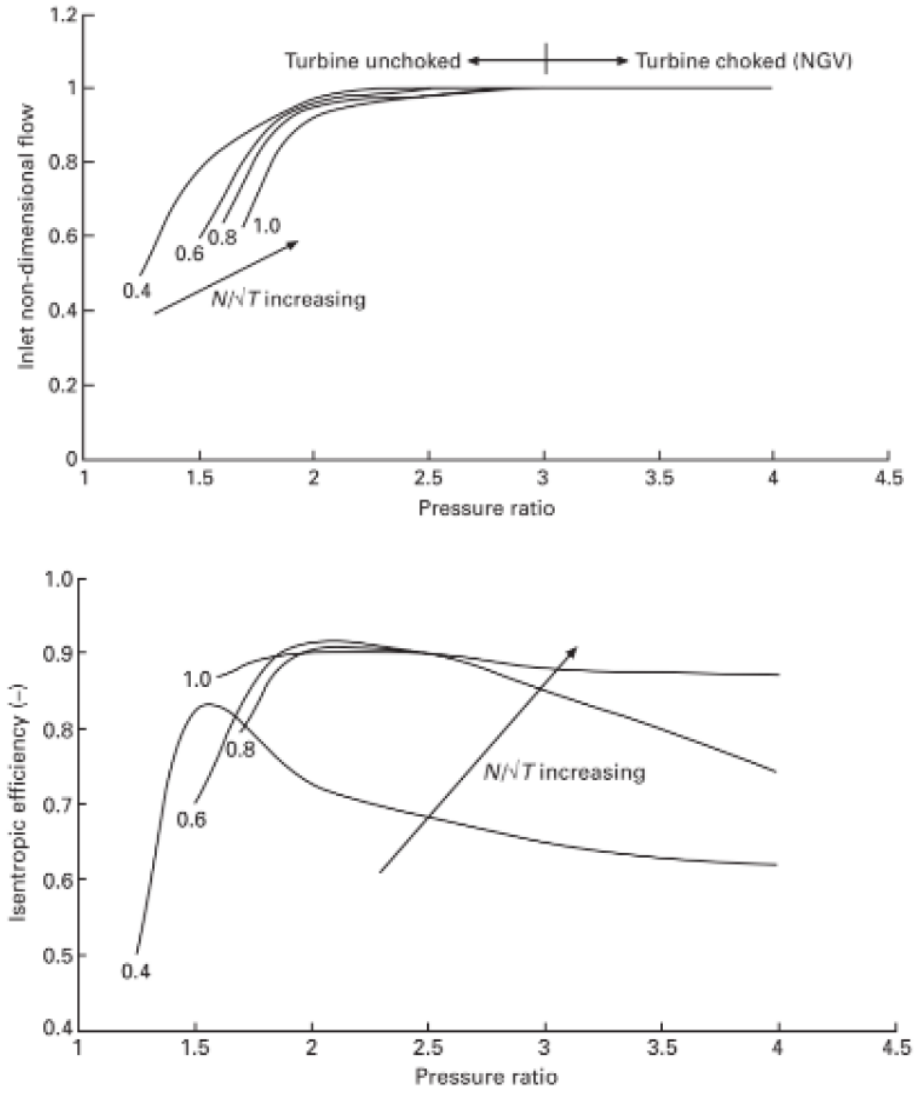

Figure 18 - Typical Turbine Map [79]

2.2.2 Surge, Stall, and Choking

Surge, stall, and choking are phenomena that impose a limitation on compressor operation. Stall can be described as the point where the angle between the compressor's rotor blade and the inlet air becomes too high. This causes the flow of air to separate from the form the surface of the rotor blade due to boundary layer separation; creating turbulent flow in the blade passage. A region of stalled flow moves from blade to blade in the compressor in the same direction as the rotor. This region may grow exponentially with time until a certain size is reached. The rate of growth is determined by the slope of the pressure ratio and mass flow characteristic, for a given constant speed on the compressor map [75,80].

Surge occurs when the surrounding conditions force an increase in compressor pressure ratio for given constant rotor speed. At this point, the stalled compressor blades cannot support the high pressure gradient resulting in an instantaneous breakdown of airflow and a decrease in compressor outlet pressure. Surges can be mild or strong, can cause flow reversal, and are often accompanied by a loud bang. Bleed valves within the compressor must be opened in order to prevent surge from occurring since it can potentially cause severe damage to the machine [75,80].

Choking occurs when the flow passes through the smallest area in the passage, referred to commonly as the throat region. At the throat, when the Mach number becomes sonic, the mass flow rate cannot be increased any further unless the area of the throat region is increased. This condition is referred to as choking and the maximum possible flow rate has been attained [75].

2.3 Cavern Modeling

When reviewing CAES modeling literature, it can be said the modeling of the air storage caverns can be divided into three categories: Models that directly ignore the effect of caverns [56, 57, 61,62], models that assume the temperature in the cavern is constant [60,63], and models that assume the cavern is adiabatic [64,66]. Meaning that there is no heat exchange between the cavern and the surrounding geology. All three assumptions do not take into account the correct heat transfer, and can cause errors in the thermodynamic analysis.

[81] presents a model for a cavern to calculate temperature and pressure variations on the basis of mass and energy conservation equations. The heat transfer by conduction to the surrounding rock is also accounted for. There are two analytical solutions presented: the one that assumes the cavern is isothermal and the average density approximation. The average density approximate solution assumes

that the density of air in the cavern does not vary a lot and can be represented by a constant average value. The model is validated against operational data taken from the Huntorf plant.

2.4 Identified gaps in literature

There is a wide variety of CAES models available in literature. Lacking in the literature are studies into the application of CAES to specific electricity grids each of which have their own consideration in terms of CAES locating, grid infrastructure, and grid management. Also lacking are high-fidelity CAES models capable of capturing system transients such as variable turbine speed-load efficiency, turbomachinery inertia as well the inertias present in their drivers, and of capturing detailed cavern dynamics and heat transfer. It is in the latter area, that the author seeks to make a relevant and novel contribution.

As per the thesis objective, this work aims to model a dynamic and modular A-CAES system. The novelty associated with is work is that the turbomachinery is modeled using performance maps and is connected to a cavern model that can capture pressure and temperature variations. The cavern will be modeled on the basis of mass and energy conservation equations as well as the heat transfer to the surrounding rock, without assuming a constant air density. Also modeled is an induction motor driving the compressor, a generator, and a TES. Each component is modeled as module, giving the overall model a modular nature. Within each module, parameters and fidelity can be easily altered. These models are presented in Chapter 3.

Chapter 3
Modeling a CAES Plant - Modular

This chapter contains the models of components that form an A-CAES system developed as part of this work. Models for the compressor, turbine module, cavern, TES (Thermal Energy Storage), induction motor, and generator are presented. The software used to create the models is Matlab/Simulink®. In the next chapter, further details are provided on how these components are connected together to form the system.

3.1 Compressor Model

The goal of the compressor model is to describe the operational behaviour of a modern axial and centrifugal with variable inlet guide vanes with sufficient fidelity to capture compression, heat transfer, irreversibilities, friction and inertia. The pressure ratio dependency on the air mass flow rate, together with the ability to influence compressor guide vanes, has been taken into account. The model uses maps, as described in section 2.2.1, that capture the real operation of a compressor in terms of efficiency, air mass flow rate, and pressure ratio. The maps used for this model are shown below in Figure 19. The map is scaled to fit CAES applications as described by [75]. A description of the scaling methodology can be found in Appendix A.

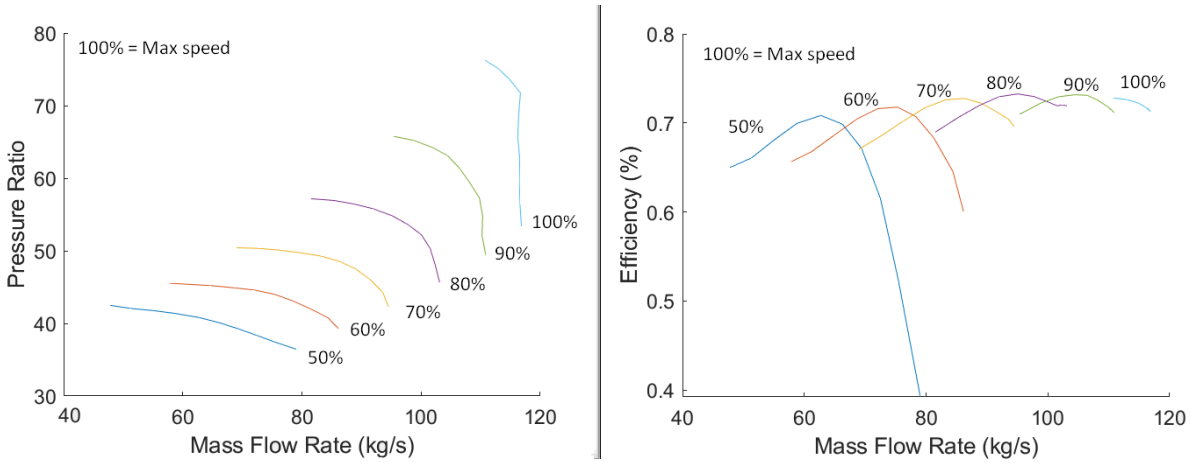

Figure 19 - Scaled NASA 37 Compressor Map

There is an additional valve that regulates the backpressure within the compressor in order to keep the operating point within the surge and stall limits on the map. This valve is not incorporated as part of the model for the sake of model simplicity and to save simulation time. This assumption does not

affect the compressor's operating range on the map, and will not influence its steady state operation. During start up and shutdown, for a very short period, when the compressor is operated below its minimum load, the consumed power and air outlet temperature may vary slightly. Hence, the impact of this assumption on the overall A-CAES model is considered minimal.

In order to connect the thermodynamics of a compressor to its rotational dynamics, equation (1) derived from Newton's second law, as described by [77] is used.

$$\frac{d\omega}{dt} = \frac{Motor\ power - Load\ - Friction\ power}{I * \omega} \tag{1}$$

Where I is the moment of inertia of the compressor and ω is its angular speed. The motor power is the electrical power consumed to the compressor that is supplied by the induction motor. The load is the power required by the motor for the compression process; and can be understood as the force that the air exerts on the compressor blades, which is normal to the force exerted on the air by the rotor. The friction power is the power lost due to mechanical friction created by the impeller, the bearings and other solid components within the compressor. From equation (1) it can be inferred that the net power in the system, divided by the product of angular speed and moment of inertia, will either accelerate or decelerate the compressor. Equations (2), (3) and (4) below show how motor power, load, and friction power are calculated respectively [75,83].

$$Motor\ power = P_{Electric} * \eta_{Motor} \tag{2}$$

$$Load = \dot{m} * \Delta h \tag{3}$$

$$Friction\ power = F * \omega^2 \tag{4}$$

Where $P_{Electric}$ is the power consumed by the induction motor. η_{Motor} is the efficiency of the induction motor. $\dot{m}$ is the mass flow rate of air in the compressor and is assumed to be uniform along the machine. Its value is obtained from the compressor map. Δh is the change in enthalpy as a result of compression and F is the friction factor, provided by the compressor manufacturer. Equations (2), (3) and (4) can be substituted into equation (1) to obtain equation (5) below.

$$\frac{d\omega}{dt} = \frac{(P_{Electric} * \in_{Motor}) - (\dot{m} * \Delta h)\ - (F * \omega^2)}{I * \omega} \tag{5}$$

In order the calculate the Δh term, the temperature at the outlet of the compressor must be calculated. This is done with the help of equation (6) on the next page [83]. Once temperature is

determined, the corresponding enthalpy is calculated using lookup tables containing the property models of air. For this work, air is assumed to behave like an ideal gas.

$$T_2 = T_1 + T_1 \left[\left(\frac{P_2}{P_1} \right)^{\frac{k-1}{k}} - 1 \right] \frac{1}{\eta_{isen}} \tag{6}$$

Where T_1 and P_1 are the ambient temperature and pressure respectively. η_{isen} is the isentropic efficiency of the compressor and is obtained from the compressor performance map. P_2 is the pressure of the air after compression. k is the polytropic index. The model is solved numerically, the required initial conditions and inputs are the ambient temperature and pressure, the compressor friction factor, cavern volume, initial cavern pressure, and a speed setpoint, after which the compressor speed is increased and mass is allowed to enter the machine. For the purposes of this work, the setpoint value is at 1% of the compressors nominal speed.

After the initial conditions have been provided, equation (5) is solved at every time step. The load is zero until the speed setpoint has been reached. Once mass is allowed to flow through the machine, the mass flow rate is determined using the compressor map by taking into account the angular speed of the rotor and the required pressure ratio. Once the mass flow rate has been determined, the isentropic efficiency is calculated using the efficiency map. After this, the compressor outlet temperature is calculated using equation (6). The model operates such that the pressure in the system volume after the compressor and before the TES is first increased to the cavern maximum pressure, before allowing air to enter the TES and the cavern. This is done using a valve. The compressor outlet temperature and angular speed of the current time step is then used to calculate the angular speed of the next time step using equation (5). Figure 20 on the next page provides a flowchart for the compressor model. Once the desirable operating point on the map is reached, mass is allowed to enter the TES and cavern; and the compressor operates there until the cavern reaches its maximum allowed pressure. It is important to note here that the compressor model can be run independently, or as part of the CAES system. The inputs shown in the dotted boxes can be removed and replaced with representative signals from other components of the system.

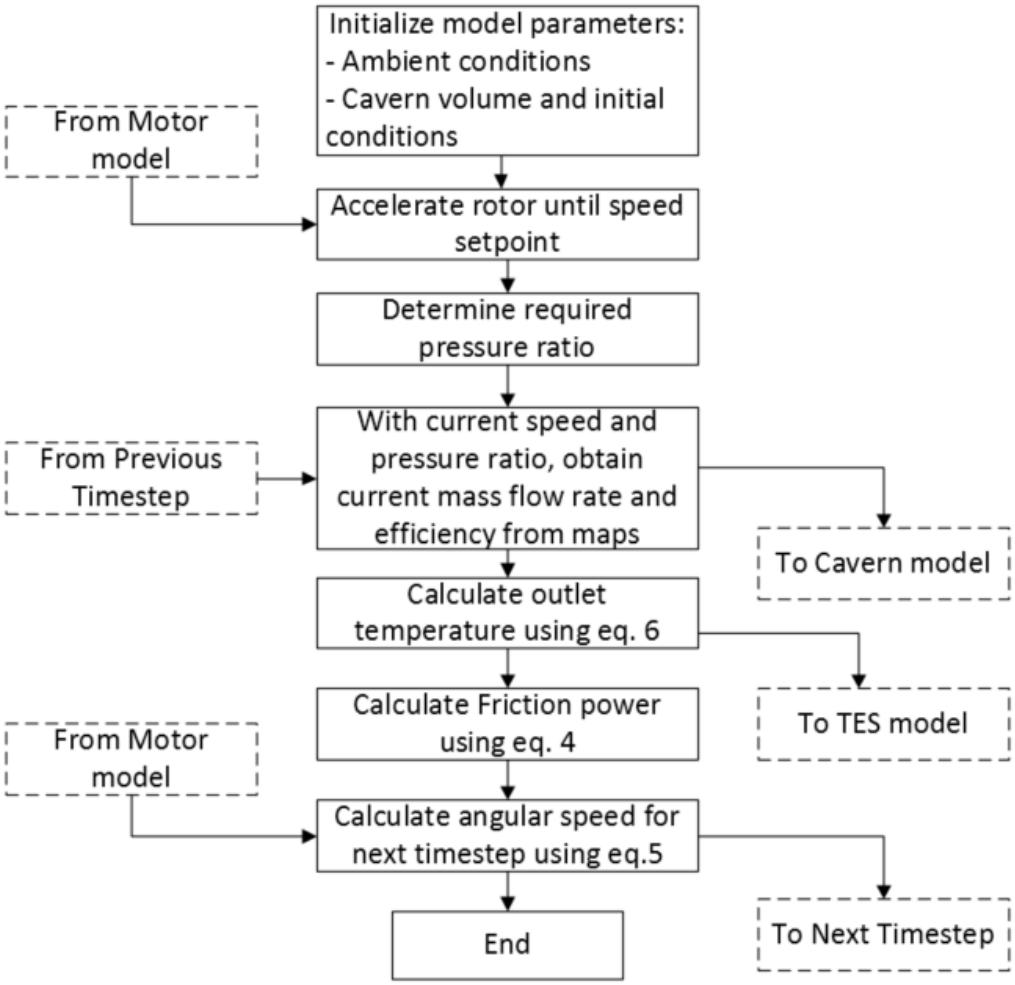

Figure 20 - Compressor model flowchart

3.1.1 Reading maps using beta lines

In literature, there are several methods published for reading data from turbomachinery maps. [84,85] outline methods using artificial neural networks to read and extrapolate turbomachinery map data. [86] published a method for reading data using two variable functions. However, the approach chosen for reading data from maps in this work is the beta lines method. There are two reasons for this, the first being the ease of implementation in Simulink®; and second reason being that it has been demonstrated in [75] to accurately read data from turbomachinery maps for CAES applications.

The beta lines method was created by [87]. In the method, equally spaced parabolic or straight lines, that are parallel to the surge line, are created and made to cover the operating region on the map. Since their equation is known, they can be used to create lookup tables with corresponding map

data [76]. When machine's angular speed and pressure ratio are known, a beta line value is guessed and corrected until it matches both parameters. With the correct beta line value, the corresponding mass flow rate and efficiency is found using interpolation within lookup tables. An illustration of this process can be seen below in Figure 21 and on the next page on Figure 22.

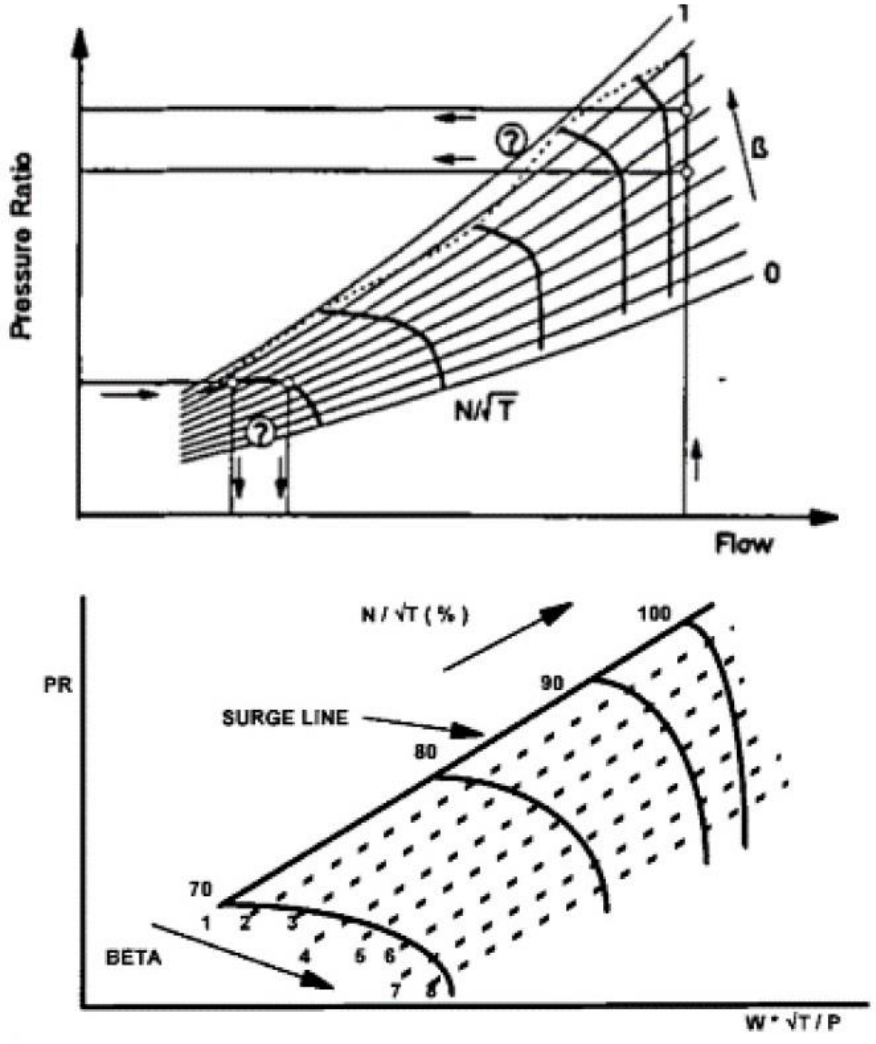

Figure 21 - Parabolic and straight Beta lines on map [76,87]

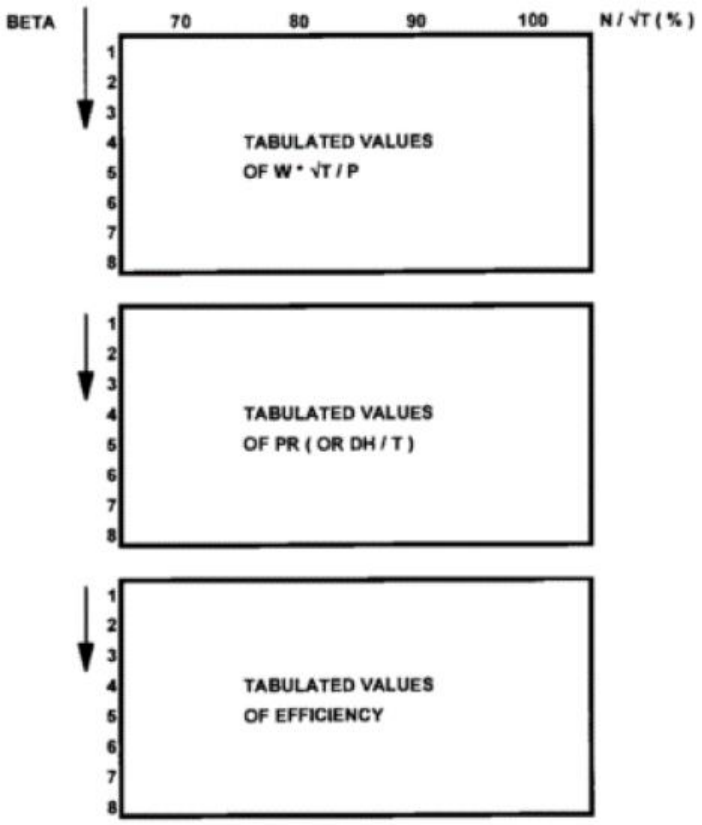

Figure 22 - Lookup tables from Beta lines [76]

In order to create beta lines on the compressor map selected for this work, a parabolic line starting from the origin and intersecting the highest point of each constant speed line is created. The line is created using a polynomial fit for the data points created by the highest points of each constant speed line. Since the line obeys the equation $y = Ax^2 + Bx + \mathrm{C}$, the value of the coefficient B can be increased to create lines that are equally spaced and occupy the operating region on the map. The result is shown on the next page on Figure 23.

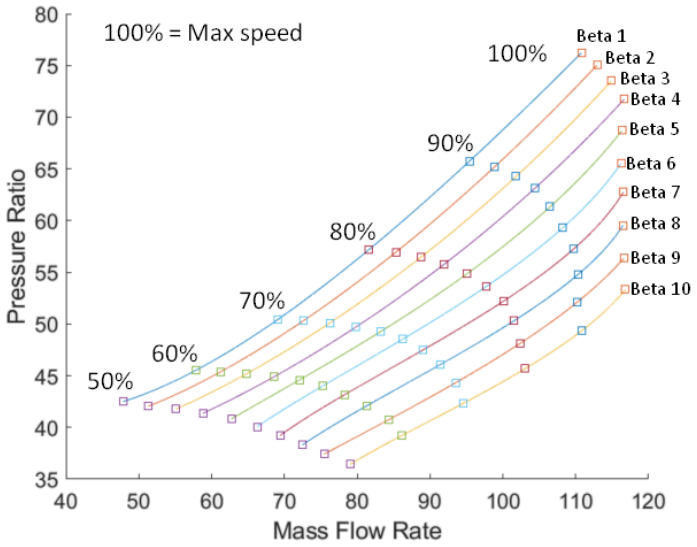

Figure 23 - Beta lines for NASA-37 Compressor

Once the operating region on the map is covered with beta lines, tables containing the data on the map can be formed. Each table contains either pressure values, mass flow rate values, or efficiency values for a corresponding beta line and speed. These tables can then be used as lookup tables in the model. Table 6 and Table 7 below show the tabulated data for the beta lines created on Figure 23.

Table 6 - Pressure ratio Beta lines data for scaled NASA-37 Compressor

		Beta Line Number									
		1	2	3	4	5	6	7	8	9	10
Speed (%)	50	40.81632	42.80277	45.0676	47.61083	50.43244	53.53245	56.91084	60.56762	64.50278	68.71634
	60	40.06455	42.19318	44.49689	46.97568	49.62956	52.45851	55.46254	58.64164	61.99583	65.5251
	70	39.2268	41.36838	43.6283	46.00653	48.50309	51.11797	53.85117	56.70269	59.67254	62.76071
	80	38.32482	40.3766	42.50419	44.70758	46.98678	49.34178	51.77258	54.27919	56.8616	59.51982
	90	37.42875	39.2557	41.15135	43.11571	45.14877	47.25054	49.42102	51.6602	53.96808	56.34467
	100	36.4384	37.95037	39.55365	41.24826	43.03419	44.91144	46.88002	48.93991	51.09113	53.33367

Table 7 - Mass flow rate Beta lines data for scaled NASA-37 Compressor

		Beta Line Number									
		1	2	3	4	5	6	7	8	9	10
Speed (%)	50	59.86956	64.55336	69.91421	75.76981	81.93789	88.23614	94.48228	100.494	106.0891	111.0852
	60	63.24817	67.72745	72.97417	78.74732	84.80586	90.90877	96.81501	102.2836	107.0734	110.9435
	70	66.26121	70.65077	75.80557	81.46301	87.36044	93.23526	98.82482	103.8665	108.0977	111.2557
	80	69.21171	73.62349	78.61014	83.95234	89.43077	94.8261	99.91901	104.4902	108.3203	111.19
	90	72.05041	76.71487	81.52499	86.38587	91.20263	95.8804	100.3243	104.4394	108.1309	111.3039
	100	75.45796	79.02917	83.09658	87.49425	92.05626	96.61666	101.0095	105.0689	108.6289	111.5235

3.1.2 Regulating System

In order to make the simulation more representative of a real compressor's operation, a simple regulating system as described by [75] is connected to the compressor. The goal of the regulating system is to ensure the safe operation of the compressor and prevent it from operating in the surge and stall regions of its map. To achieve this, the map uses two parabolic lines to identify the safe operating region. These lines are then interpreted as equations and compared to the values of the operating point. If the operating point is above the upper limit, the mass flow rate is increased until the operating point is back within specified limits. If the operating point is below the lower limit, the mass flow rate is decreased until the operating point is back within specified limits. The rotational speed of the compressor is adjusted after the mass has been regulated. Figure 24 below illustrates the limits set on the used compressor map.

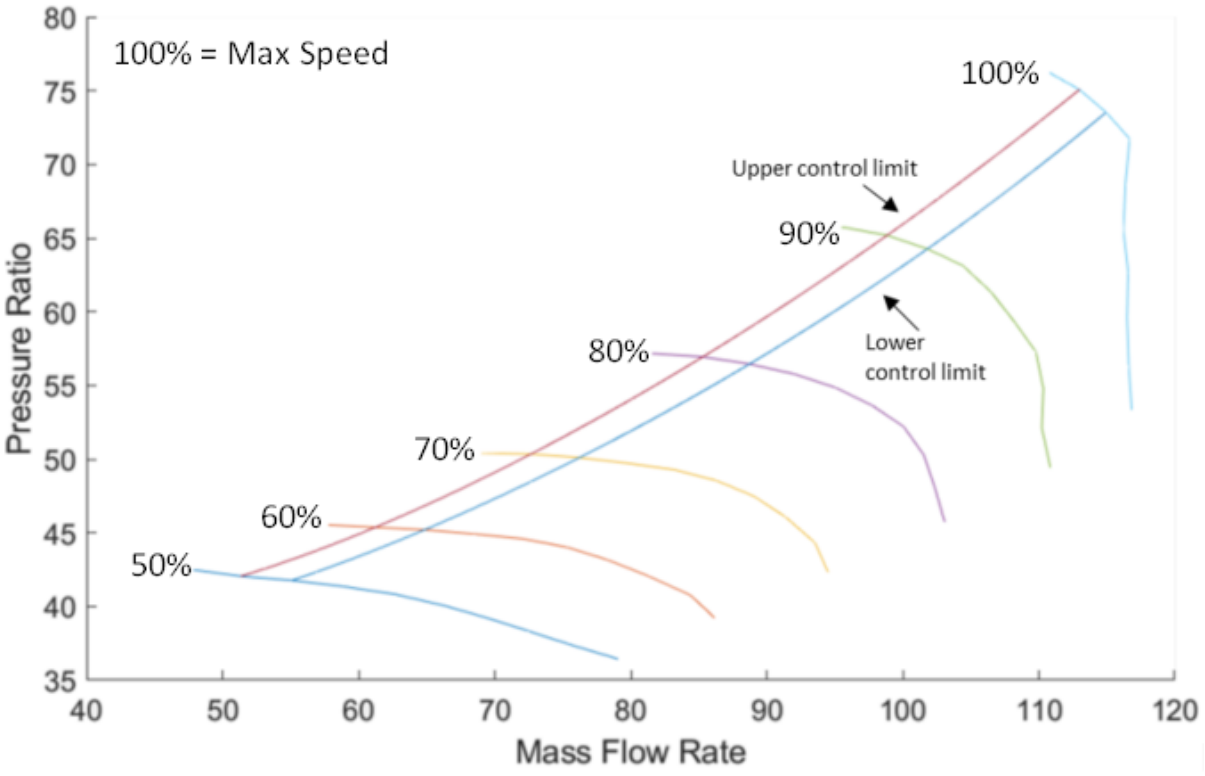

Figure 24 - Compressor map regulating system limits

3.2 Turbine Model

The expansion train of CAES plants is commonly equipped with axial turbines. The turbine model is similar to the compressor model, the governing equations derived from the same conservation laws and the model makes use of maps to describe the real operation of a turbine. However, the expansion is modelled as a semi-steady process: the pressure at the inlet and outlet of the turbine is kept constant. The turbine outlet temperature is determined by its isentropic efficiency. The maps used to simulate the turbine are shown below in Figure 25. The map has been scaled to fit CAES applications as described by [75]. A description of the scaling methodology can be found in Appendix A.

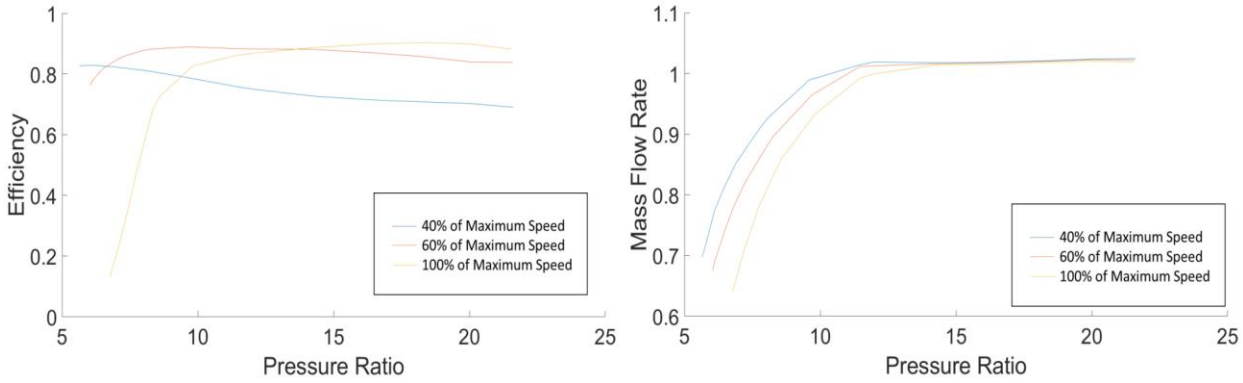

Figure 25 - Turbine map [75]

Using Newton's second law, equation (7) can be derived to connect the thermodynamics of the turbine to its rotational dynamics [83].

$$\frac{d\omega}{dt} = \frac{Turbine\ Power - Load\ - Friction\ Power}{I * \omega} \tag{7}$$

Where I is the moment of inertia of the turbine and ω is its angular speed. The turbine power is the rotational mechanical power produced by the turbine. The load is the electrical power needed to be met by the turbine, and can be understood as the demanded power. The friction power is the power lost due to mechanical friction created by the bearings and other solid components within the turbine. Like the compressor, the turbine will accelerate or decelerate proportional to the net power within the system divided by the by the product of angular speed and moment of inertia. Equation (8) on the next page shows how the turbine power can be calculated, friction power is calculated using equation (4) and the friction factor is provided by the manufacturer, and the load is signal received by the turbine which contains the demanded power.

$$Turbine\ power = \dot{m} * \Delta h \tag{8}$$

Where. $\dot{m}$ is the mass flow rate of air in the turbine and like the compressor, is assumed to be uniform along the machine. Its value is obtained using the turbine map. Δh is the change in enthalpy as a result of expansion. Equations (4) and (8) can be substituted into equation (7) to obtain equation (9) below.

$$\frac{d\omega}{dt} = \frac{(\dot{m} * \Delta h) - Load\ - (F * \omega^2)}{I * \omega} \tag{9}$$

The turbine exit temperature is calculated using equation (10) below, and is required in order to obtain the air exit enthalpy [83].

$$T_6 = T_5 - T_5 * \eta_{isen} * \left[1 - \left(\frac{P_5}{P_6}\right)^{\frac{k-1}{k}}\right] \tag{10}$$

Where $T_5$and P_5 are the turbine inlet temperature and pressure respectively. These values are provided by the cavern and TES model. P_6 is the ambient pressure. η_{isen} is the isentropic efficiency of the turbine and is obtained from the turbine performance map. k is polytropic index. The model is solved numerically, the required inputs are ambient pressure, initial non-zero speed, operating pressure ratio, the turbine friction factor, and the load.

First an initial non-zero value for speed and pressure ratio is used and increased until the operating pressure ratio is reached. For every speed and pressure ratio value, a corresponding mass flow rate and isentropic efficiency value is obtained using the turbine maps. The turbine outlet pressure and friction power is then calculated using equation (4) and (10) respectively. After this equation (9) is solved to find the angular speed of the next time step. Figure 26 on the next page provides a flowchart for the turbine model. Similar to the compressor, it is important to note here that the turbine model can be run independently, or as part of the CAES system. The inputs shown in the dotted boxes can be removed and replaced with representative signals from the other components of the system.

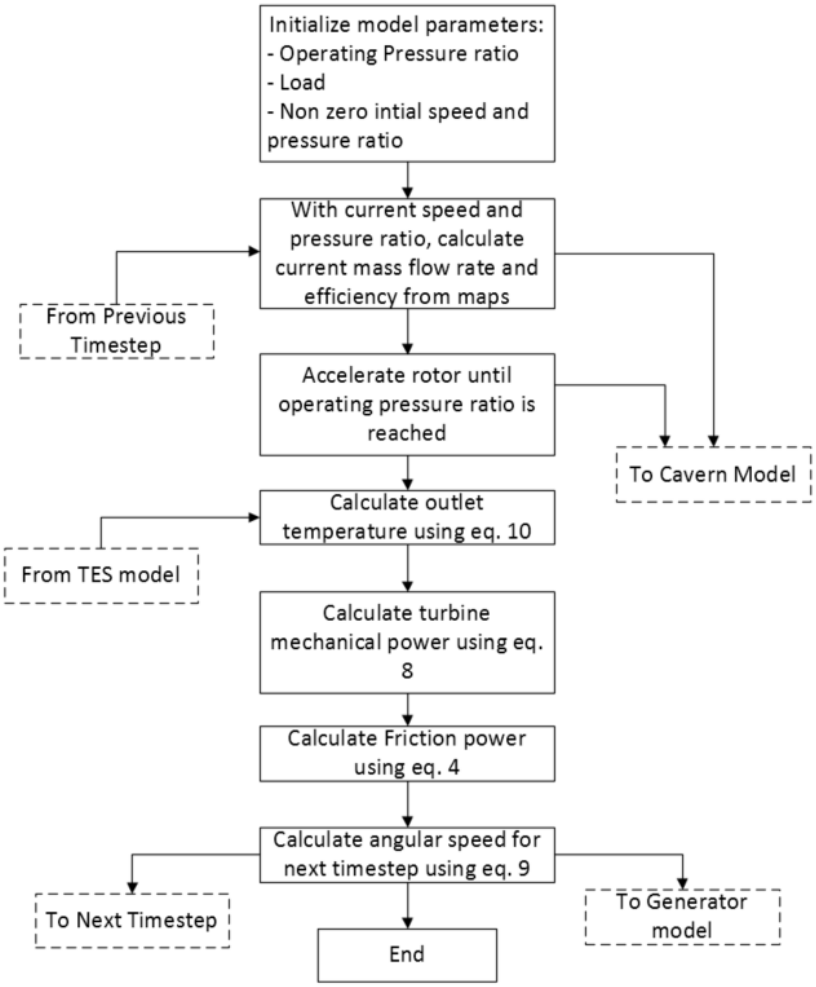

Figure 26 - Turbine model flowchart

3.3 Cavern Model

The air storage is modeled as a cavern and is considered as the control volume and is assumed to be cylindrical in shape. The goal of the model is to capture the thermodynamic response from charging and discharging the cavern. The cavern's walls, and input and output ports are the system boundaries. During charging and discharging, the air flows cyclically in and out of the cavern via the ports. For the purposes of this model, air leakage is ignored; this is a reasonable assumption when the surrounding rock is salt or low-permeability rock. Equation (11) below and equation (12) on the next page are formed based on the mass and energy conservation laws respectively as described by [81].

$$V\frac{d\rho}{dt} = \dot{m}_\iota + \dot{m}_e \tag{11}$$

$$V * \rho * C_v * \frac{dT}{dt} = \dot{m}_\iota \left(h_i - h + ZRT - \rho \frac{du}{d\rho}\Big| T \right) + \dot{m}_e \left(ZRT - \rho \frac{du}{d\rho}\Big| T \right) + \dot{Q} \quad (12)$$

Where V is the volume of the cavern. ρ is the density of air. $\dot{m}_i$ and $\dot{m}_e$ are the mass flow rates of air entering and exiting the cavern respectively. C_v is the constant volume specific heat of air, and for this work, is assumed to be a constant value. T is the temperature of the air in the cavern. h is the enthalpy of the air. Z is the air compressibility factor. R is the universal gas constant. u is the internal energy of the air and $\dot{Q}$ is the heat transfer by convection at the cavern wall. Equations (13) and (14) below show how this heat convection can be calculated, and the generalized gas state law, respectively.

$$\dot{Q} = h_c * A_c * (T_{RW} - T) \quad (13)$$

$$P = Z\rho RT \quad (14)$$

Where h_c is the convective heat transfer coefficient. A_c is the cavern wall surface area. T_{RW} is the cavern wall surface temperature. If the variation of air temperature in the cavern is small, it is reasonable to assume that cavern wall temperature remains constant. Hence in the simulation, the heat lost is modeled as a heat loss to the cavern walls, and not subsequently to the surrounding rock. Equation (15) below along with boundary conditions shown in equations (16) and (17) below can used to calculate the heat condition to the surrounding rock.

$$\rho_R * C_{P,R} * \frac{dT_R}{dt} = \frac{1}{r}\frac{d}{dr}\left(k_R * r * \frac{dT_R}{dr} \right) \quad (15)$$

Boundary conditions:

$$r = R_{RW}, \quad -k_R \frac{dT_R}{dr} = h_c(T - T_{RW}) \quad (16)$$

$$r \to \infty, \quad T_R = T_0 \quad (17)$$

Where ρ_R is the density of the surrounding rock. $C_{P,R}$ is the constant pressure specific heat of the rock. T_R is the temperature of the rock. k_R is the thermal conductivity of the rock. R_{RW} is the radius of cavern.

Upon substituting equation (13) and (14) in equation (12) and making the assumption that air is an ideal gas, equation (18) on the next page is obtained. When air is treated as an ideal gas, the change of internal energy with respect to density is zero, $\frac{du}{d\rho}\Big| T = 0$; Furthermore, the value of the air compressibility factor is 1, Z=1.

$$V * \rho * C_v * \frac{dT}{dt} = \dot{m}_\iota(h_i - h + RT) + \dot{m}_e(RT) + h_c * A_c * (T_{RW} - T) \quad (18)$$

The cavern model, like the compressor and turbine model, is solved numerically. The required inputs and initial conditions are cavern radius and depth, cavern initial pressure and temperature, convective heat transfer coefficient, the mass flow rate and temperature of air entering the cavern, and the mass flow rate of the air leaving the cavern. The mass flow rate and temperature of the air entering the cavern is provided by the compressor and TES model respectively. Mass is allowed to enter the cavern once the compressor reaches the desired operating point on its map. When a mass flow rate input is provided for charging or discharging the cavern, each term within equation (18) is calculated. The instantaneous air density in the cavern is calculated using equation (11). Equation (18) is solved for every time step in order to calculate temperature changes in the cavern with time. The corresponding pressures are calculated using equation (14). Figure 27 below shows the flowchart for the turbine model.

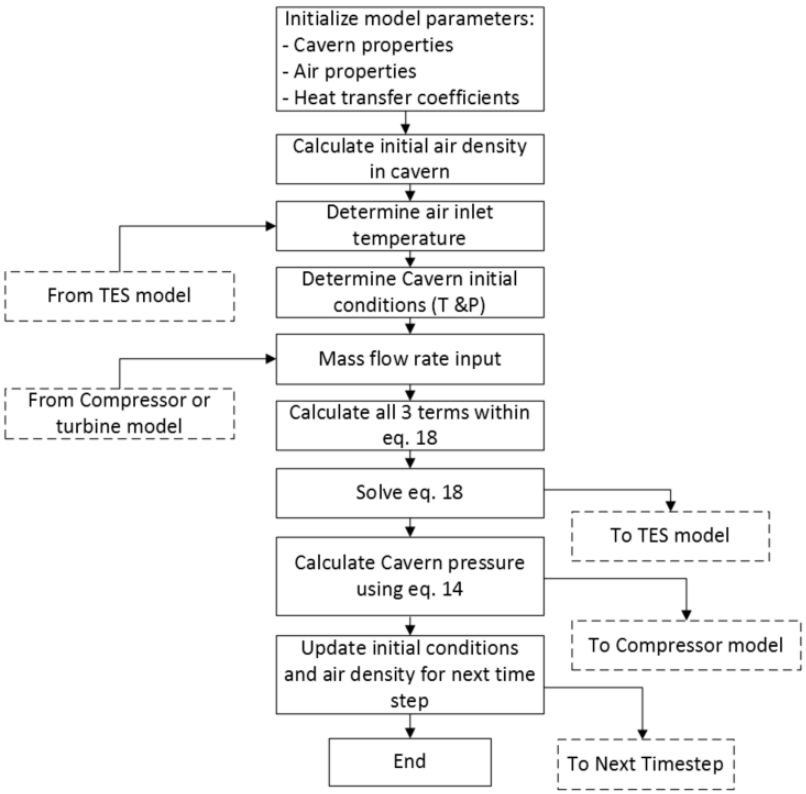

Figure 27 - Cavern Model Flowchart

It is important to note here that the cavern model can be run independently, or as part of the CAES system. The inputs shown in the dotted boxes can be removed and replaced with representative signals from other components of the system.

3.4 Thermal Energy Storage (TES) Model

The Thermal Energy Storage (TES) component is what distinguishes A-CAES from gas fired CAES plants. The TES module cools the air after compression before it enters the cavern. The heat from compression is stored in the TES. During discharging, the air passes through the TES and the air is heated before expansion. For this work, the TES is modeled as a simple and ideal module. The stored thermal energy after compression is calculated according to equation (19) below. The thermal energy that is injected back into the air before expansion is given by equation (20) below[88].

$$Q_{Charging} = \int \dot{Q} dt = \int \dot{m} C_p (T_3 - T_2) dt \tag{19}$$

$$Q_{Discharging} = \int \dot{Q} dt = \int \dot{m} C_p (T_5 - T_4) dt \tag{20}$$

Where T_2 refers to the temperature of the air before entering the TES, after compression. T_3 refers to the temperature of the air before entering the cavern, after it has been cooled. This value can be set by the model user. T_4 refers to the temperature of the air exiting the cavern and entering the TES, during discharge. T_5 refers to the temperature of the air exiting the TES during discharge. This value can be set by the model user. C_P is the constant pressure specific heat of the air. Equation (21) below shows how the efficiency of the TES is calculated.

$$\eta_{TES} = \left(\frac{Q_{Discharging}}{Q_{Charging}} \right) * 100 \tag{21}$$

The required inputs for the model are the desired temperature of the air entering the cavern and turbine respectively, and the constant pressure specific heat of air. Figure 28 on the next page shows the flowchart for the TES model. It is important to note here that the TES model can be run independently, or as part of the CAES system. The inputs shown in the dotted boxes can be removed and replaced with representative signals from the other components of the system.

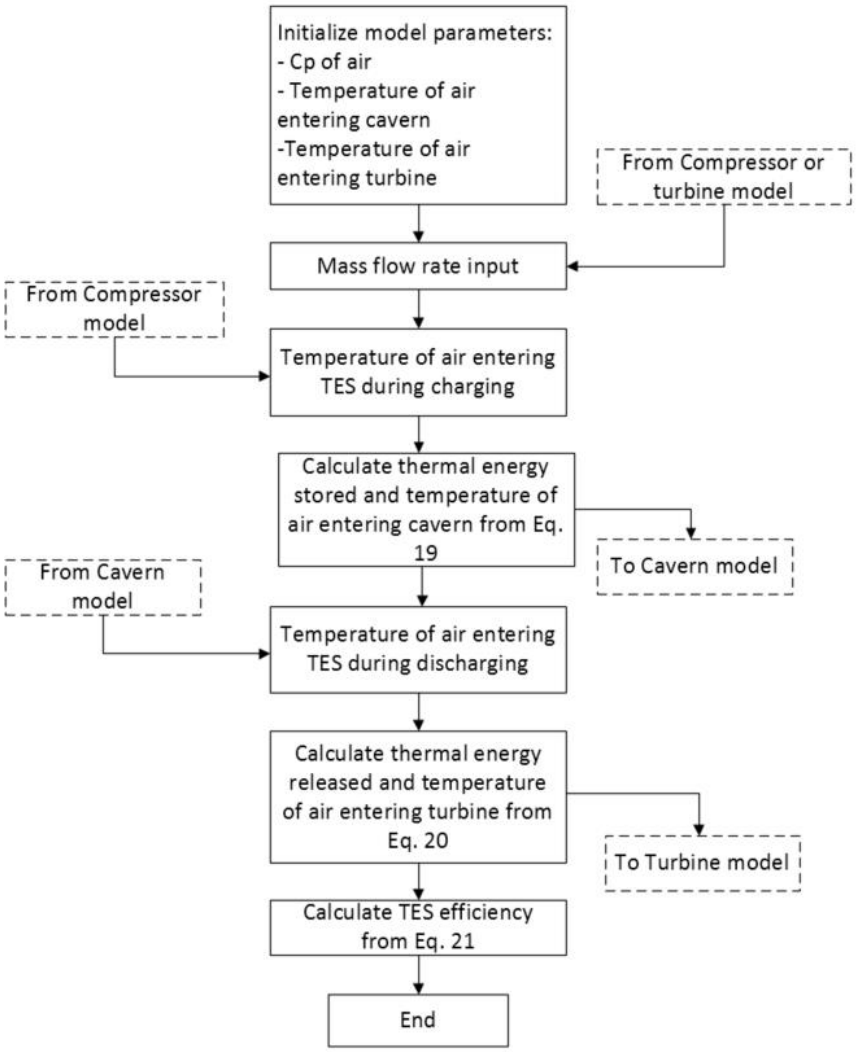

Figure 28 - TES Model flowchart

3.5 Induction Motor & Generator Model

An asynchronous machine consists of a rotor, stator, stator core, stator windings, shaft, bearings and an enclosure. When operating as a motor, an electrical current is sent to the machine and torque is produced by electromagnetic induction from the magnetic field of the stator windings. When operating as a generator, torque is supplied to the machine via the shaft from an external source, and an electrical current is generated [89]. In this work, the induction motor that drives the compressor, and the generator that gets driven by the turbine, are modeled as a three phase asynchronous machine. In order to model the machine, an “Asynchronous Machine” block from the Simulink® library is

chosen. This machine can be used to simulate the behaviour of a generator or motor, depending on what torque input is provided [90]. Figure 29 below shows electrical circuit for the motor.

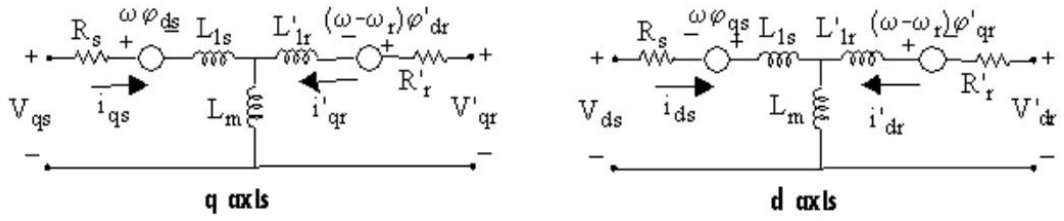

Figure 29 - Asynchronous Machine Circuit [90]

The required inputs are the rated power, voltage, frequency, rotor resistance and inductance, stator resistance and inductance, mutual inductance, moment of inertia, friction factor and number of poles. The characteristic equations, (22) - (32), taken from MATLAB® literature are described below. Equations (22) and (23) below describe the stator.

$$V_{qs} = R_s i_{qs} + \frac{d\phi_{qs}}{dt} + \omega\phi_{ds} \tag{22}$$

$$V_{ds} = R_s i_{ds} + \frac{d\phi_{ds}}{dt} + \omega\phi_{qs} \tag{23}$$

Where V_{qs} is the stator voltage from the q-axis. R_s is the stator resistance. i_{qs} is the stator current from the q-axis. $\frac{d\phi_{qs}}{dt}$ is the back electromotive force from the q-axis. ω is the angular speed and $\phi_{ds}$is the stator flux from the d-axis. Equation (23) is analogous to equation (22). Terms in equation (23) correspond to the d-axis, as opposed to the q-axis. Equations (24) and (25) below describe the rotor.

$$V'_{qr} = R'_r i'_{qr} + \frac{d\phi'_{qr}}{dt} + (\omega - \omega_r)\,\phi'_{dr} \tag{24}$$

$$V'_{dr} = R'_r i'_{dr} + \frac{d\phi'_{dr}}{dt} + (\omega - \omega_r)\,\phi'_{qr} \tag{25}$$

Where V'_{qr} is the rotor voltage from the q-axis. R'_r is the rotor resistance. i'_{qr} is the rotor current from the q-axis. $\frac{d\phi'_{qr}}{dt}$ is the back electromotive force from the q-axis. ω is the angular speed, ω_r is the reference angular speed, and $\phi'_{dr}$is the rotor flux from the d-axis. Equation (25) is analogous to equation (24). Terms in equation (25) correspond to the d-axis, as opposed to the q-axis. Equation (26) below shows the calculation of the electromagnetic torque.

$$T_e = 1.5p(\phi_{ds} i_{qs} - \phi_{qs} i_{ds}) \tag{26}$$

Where T_e is the electromagnetic torque. p is the number of poles. $\phi_{ds}$is the stator flux from the d-axis. i_{qs} is the stator current from the q-axis. $\phi_{qs}$is the stator flux from the q-axis. i_{ds} is the stator current from the d-axis. Equations (27) and (28) below describe how the stators electromagnetic flux is calculated; and equations (29) and (30) describe how the rotors electromagnetic flux is calculated.

$$\phi_{qs} = L_s i_{qs} + L_m i'_{qr} \tag{27}$$

$$\phi_{ds} = L_s i_{ds} + L_m i'_{dr} \tag{28}$$

$$\phi'_{qr} = L'_r i'_{qr} + L_m i_{qs} \tag{29}$$

$$\phi'_{dr} = L'_r i'_{dr} + L_m i_{ds} \tag{30}$$

Where L_s is the total stator inductance and L_m is the total magnetizing inductance. L'_r is the rotor total inductance. Equation (28) and (30), which correspond to the d-axis, are analogous to equations (27) and (29), which correspond to the q-axis. Equation (31) and (32) below describe how the stator and rotor total inductance is calculated, respectively.

$$L_s = L_{ls} + L_m \tag{31}$$

$$L'_r = L'_{lr} + L_m \tag{32}$$

Where L_s is the stator total inductance. L'_r is the rotor total inductance. L_{ls} is the stators leakage inductance and L_{lr} is the rotors leakage inductance.

Chapter 4
Modeling a CAES Plant – Connected Model

In this chapter, it will be presented how the different individual component models from chapter 3 will be connected together to form an A-CAES system. Figure 30 below shows the schematic of the system that is being modeled.

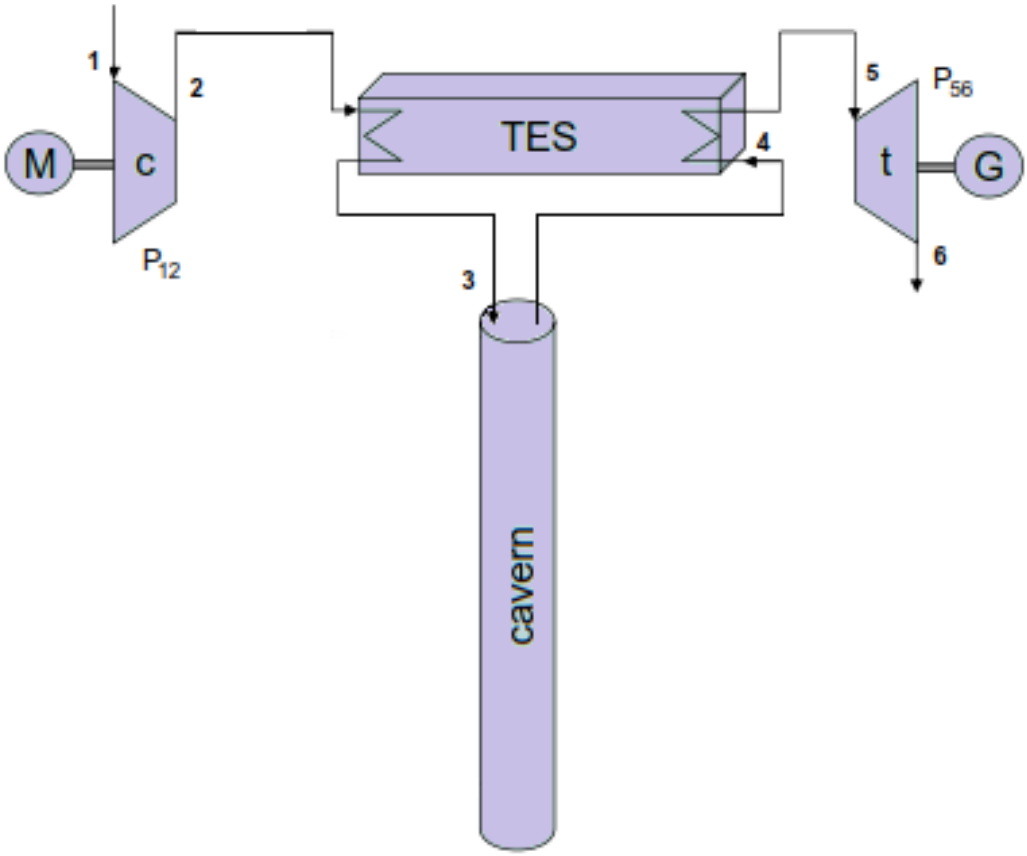

Figure 30 - CAES Schematic

Each component is modeled such that it can be simulated independently, or as part of the overall connected model. This is evident when observing the model flowcharts in Figure 20, Figure 26, and Figure 27. Each component can be easily modified or removed from the system entirely. In this way, the overall model has a modular nature and can facilitate further CAES research. For example, the user of the model can isolate and simulate certain parts of the system in order to study them. The compression train or the expansion train can be studied individually. The user can also change the

fidelity of components within the model, or change the overall system configuration, i.e. simulate D-CAES or I-CAES plants. The connected model is made keeping in mind its future growth to enable further research. Component and system level behaviour during start-up and transient operation can be studied. Furthermore, the model can easily connect to an external control strategy, or be connected to an economic model to study the scope of different CAES plants in different energy markets. The model uses the equations discussed in Chapter 3 in order to represent the behaviour of an A-CAES system. Figure 30 below shows how the different subsystems in the model and the equations governing their behaviour during charge and discharge.

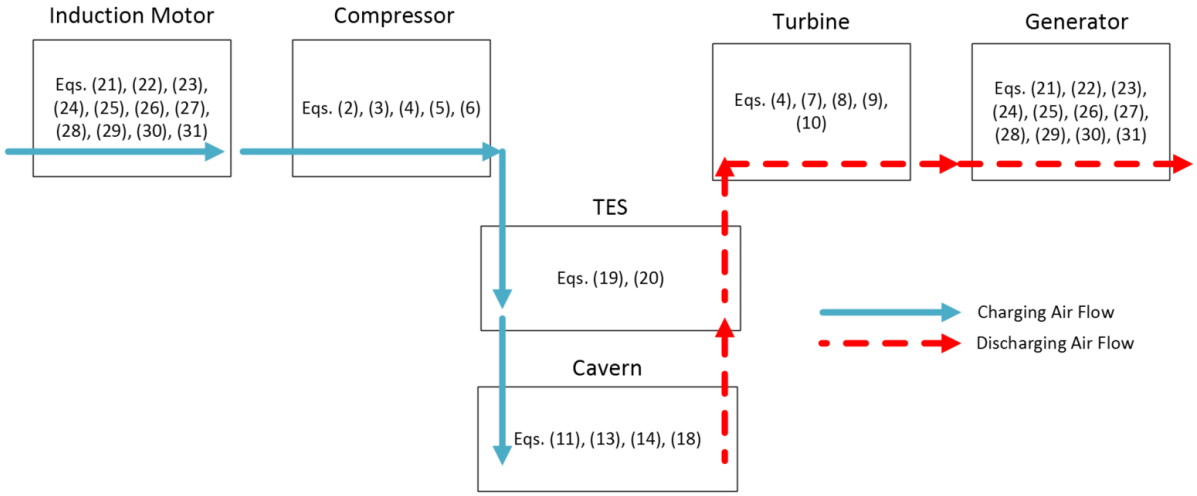

Figure 31 - CAES block diagram with equations

Depending on whether the system is in charge mode, or discharge mode, a different set of equations is to be solved. Figure 30 above shows which components, and consequently which equations will be solved during when the system is in charge or discharge mode. Each of these blocks exchange information in the form of signals, such as mass flow rate, temperature, etc. between them. For the connected model depicted above, the following assumptions are made:

- Air is treated as in ideal gas
- The flow of air is uniform along the compressor and turbine
- Cavern is cylindrical in shape and is underground
- Constant volume specific heat and constant pressure specific heat of air are constant
- Variation of temperature within the cavern is small

- Compressor valve avoiding surge has little to no effect on the overall system
- All the friction within the turbomachinery is proportional to its angular speed and can be represented by the friction factor
- The cavern is underground and heat transfer losses in cavern are lost to cavern wall
- There are no air leakages in the cavern
- When no mass is flowing through the compressor during start-up, it behaves according to the rotor dynamics of the induction motor that is driving it
- The system piping volume after the compressor is 1500 m^3
- Ambient conditions remain constant
- The TES is an ideal device
- Air leaving the cavern during expansion is throttled by a regulator valve so that the turbine can operate at a constant pressure ratio

In the next chapter, the models presented in Chapter 3 and Chapter 4 will be simulated and the results from simulation will be discussed.

Chapter 5
Results

In this chapter, the models presented in Chapter 3 and Chapter 4 are simulated and their key results are presented and discussed. This chapter is divided into three subsections: charging results, storage results, discharging results, and overall system results The results aim to verify that the models behave as expected with regards to start-up behavior, steady-state behaviour, and limits imposed to turbomachinery operation by the surge and stall phenomenon. Since there are no A-CAES plants that are currently operational in the world, the design and simulation of the model was based on adiabatic version of the Huntrof plant. Additionally, there is limited measured data to validate the model against. Therefore, this chapter focuses on ensuring the transient results from each component in the system, and the overall CAES plant model, are reasonable when compared to the Huntorf Plant.

A period of approximately 24 hours is simulated starting with a charging period to fill the cavern to its maximum pressure; followed by a storage and discharge period, which can be considered a typical cycle for a CAES plant [81]. Table 8 below presents the simulation parameters from each period.

Table 8 - Simulation parameters

Period	Parameter	Value & Units	Comments
All	Total time	23.3 hours	-
	Ambient air pressure	101 KPa	-
	Ambient air temperature	25°C	-
	Cavern volume	150,000 m^3	Data from reference [45]
	Cavern surface area	25,000 m^2	Data from reference [45]
	Cavern wall temperature	40°C	Data from reference [88]
	Grid voltage	460V	Data from reference [91]
	Grid frequency	60 Hz	Data from reference [91]
	Heat transfer coefficient	30 $Wm^{-2}K^{-1}$	Data from reference [88]
	Specific air constant	286.7 J/(kg K)	Data from reference [88]
	Constant pressure specific heat of air	1000.4 J/(kg K)	Data from reference [88]
	Constant volume specific heat of air	717.0 J/(kg K)	Data from reference [88]

Charging	Time	12.47 hours	-
	Mass flow rate	107.5 kg/s	Data from reference [45]
	Compressor inertia	2400 kg m^2	Data from reference [83]
	Compressor friction factor	3.94	Data from reference [83]
	Initial cavern pressure	41.9 Bar	-
	Final cavern pressure	72 Bar	-
	Cavern inlet air temperature	55°C	Data from reference [88]
	Initial cavern temperature	35°C	Data from reference [75]
	Nominal motor power	50 MW	Data from reference [75]
	Motor inertia	1200 kg m^2	Data from reference [83]
	Motor friction factor	0.054	Data from reference [83]
Storage	Time	8 hours	-
Discharging	Time	2.83 hours	-
	Mass flow rate	400 kg/s	Data from reference [45]
	Turbine pressure ratio	10	Data from reference [75]
	Turbine inertia	1560 kg m^2	Data from reference [83]
	Turbine friction factor	0.02	Data from reference [83]
	Turbine inlet temperature	1300°C	Data from reference [75]
	Turbine nominal angular velocity	17000 rpm	Data from reference [83]
	Initial cavern pressure	72 Bar	-
	Final cavern pressure	42 Bar	-
	Initial cavern temperature	40.9°C	-
	Nominal generator power	167 MW	Data from reference [75]
	Generator inertia	3510 kg m^2	Data from reference [83]
	Generator friction factor	0.054	Data from reference [83]

In the subsequent subsections, results from the charging, storage and discharge periods will be presented and discussed; followed by results from the overall cycle operation.

5.1 Charging

In the simulation, the cavern is first charged from 42 bar to 72 bar. The components from the system that are active during charging are the compressor, the induction motor, the TES and the cavern. The following subsections present the results pertaining to each component.

5.1.1 Compressor

The compressor operates by receiving power via a rotating shaft from the induction motor. Initially, the power from the induction motor is used to speed up the compressor to 50% of its nominal speed. After this, a valve is opened and air is allowed to flow inside the machine while the pressure ratio is gradually increased until the desired pressure ratio and mass flow rate. For this simulation, the pressure after compression was chosen to be slightly higher than the maximum allowable cavern pressure. Once the compressor speeds up, it operates at the desired operating point with respect to mass flow rate and pressure ratio until the pressure in the cavern is 72 bar. Figure 33 below shows the compressor's operating line on its performance map.

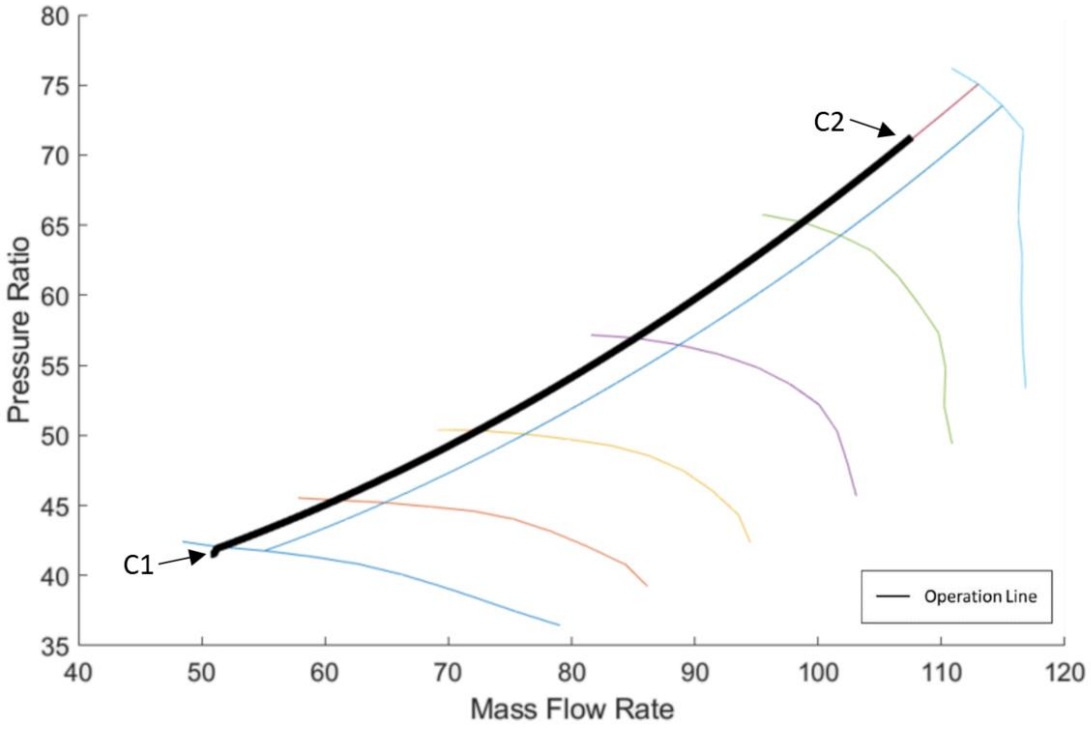

Figure 32 - Compressor operating line on performance map

From the figure it can be observed that the compressor operates as expected within the surge and stall limits imposed by the regulating system. At point C1, the compressor begins to allow the mass to

flow inside it. The initial pressure ratio is 42 and it is increased gradually until 72. At point C2, the compressor has reached its desired operating point with respect to mass flow rate and pressure ratio. The compressor operates at this point until the cavern is fully charged.

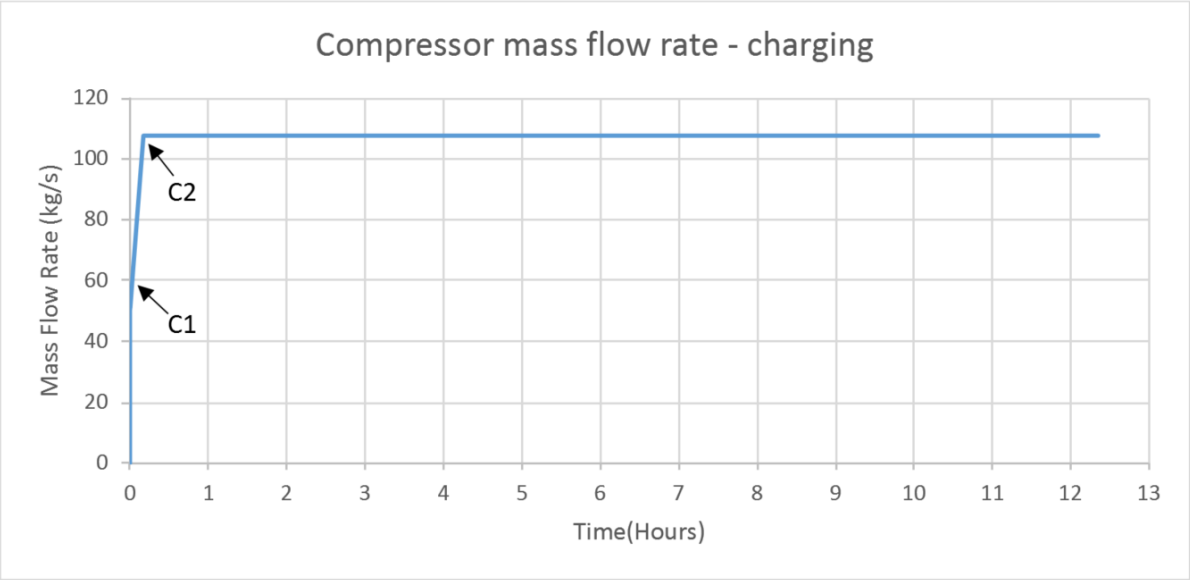

Figure 33 - Compressor mass flow rate during charging

Figure 33 above shows the variation of mass flow rate in the compressor for the charging period. From the figure it can be observed that the mass flow rate initially increases, and then remains constant for the charging period. For the first 2.4 seconds, there is no mass flowing inside the compressor. During this time the compressor is being sped up by the induction motor. The mass flow rate then begins then to increase from 50 kg/s, shown by point C1, to 107.5 kg/s, shown by point C2 and is the desired mass flow rate for charging. The startup of the compressor takes about 619 seconds. The compressor operates at the desired mass flow rate until the cavern is fully charged. It is important to note here that points C1 and C2 in all the compressor figures correspond to the same phenomenon respectively.

Figure 34 on the next page shows the change of compressor angular speed for the charging period. The angular speed of the rotor of the compressor is governed by the induction motor. Initially, the compressor is sped up to 50% of its nominal speed, before opening the valve and allowing mass to enter the machine. The opening of the valve is illustrated at point C1 on the figure. It takes about 2.4 seconds for the compressor to reach 50% of its nominal speed. After this, the compressors speed is increased to about 96% of its nominal speed, illustrated by point C2. As expected, the rate of increase

in compressor speed is lowered after mass is allowed to enter the machine. The compressor operates at about 96% of its nominal speed until the cavern is fully charged.

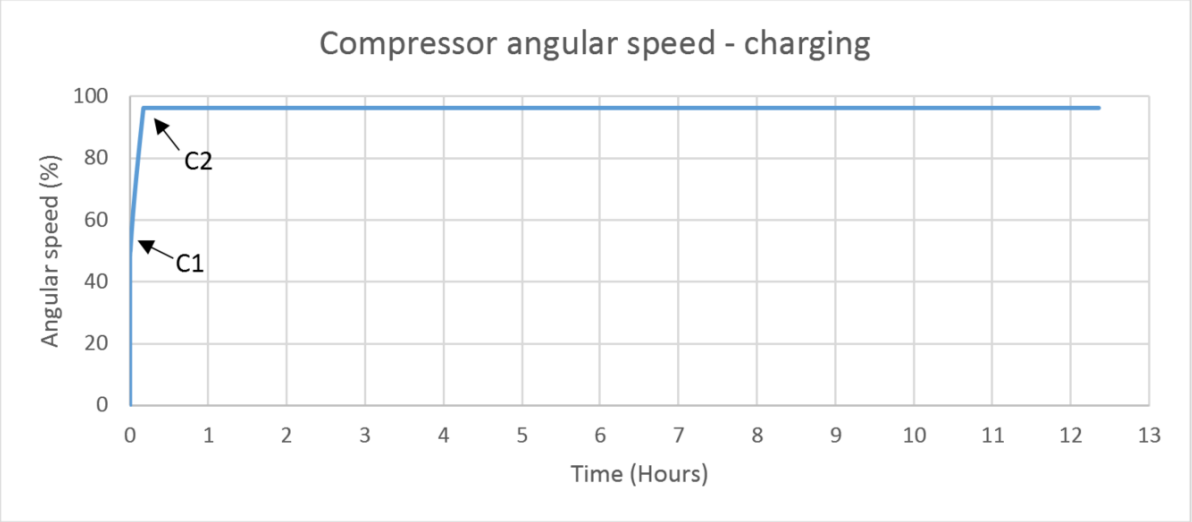

Figure 34 - Compressor angular speed during charging

Figure 35 below shows the change in compressor efficiency during the charging period The efficiency of the compressor is influenced by its operating mass flow rate, speed and pressure ratio. The initial efficiency of the compressor is 70%. During startup, the efficiency reduces with time, to 66.1%. This is because no mass is allowed to enter the machine. At point C1, the value opens and mass enters the machine. The compressor efficiency then rises to 72.6%, illustrated by point C2 and remains constant for the remainder of the charging period.

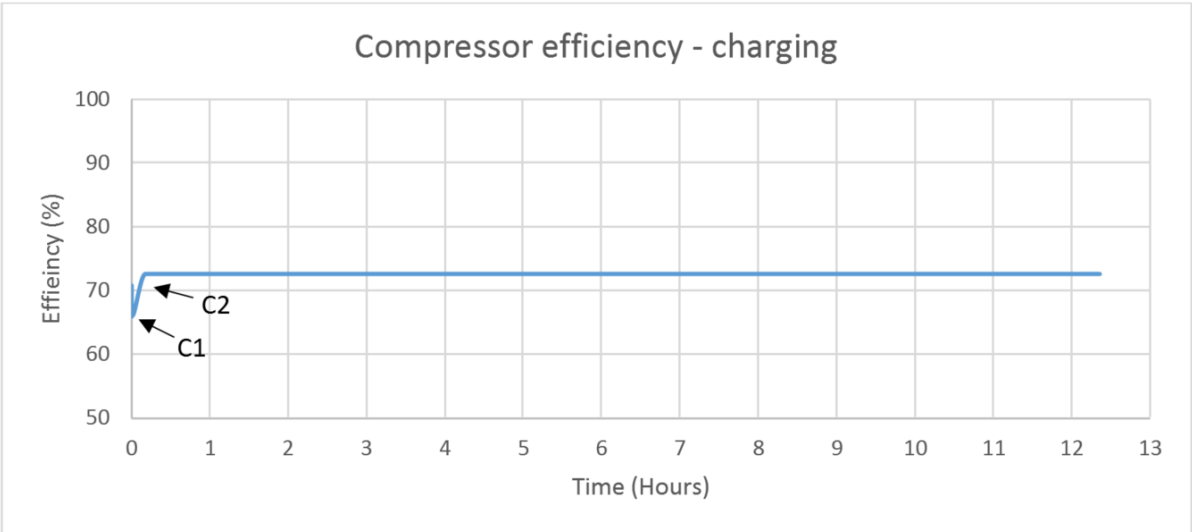

Figure 35 - Compressor efficiency during charging

The average efficiency of the compressor during the charging period is 69.4% However, it operates above 70% for most of the charging period with a peak efficiency of 72.6%. The total variation in compressor efficiency during charging is about 8%, with a less than 1% change during steady state operation showing that the compressor operates in a stable manner.

5.1.2 Induction motor

During charging, the induction motor consumes power from the grid and drives the compressor. Figure 36 below shows the power consumed by the induction motor during the charging period. From the figure it can be observed that there is a large initial power consumed, after which the power stabilizes to about 50 MW. This large power can be attributed to an excessively large current drawn by induction motors during startup, and is a common occurrence [92]. The voltage induced in the motor during startup is at its maximum value because of maximum slip. Due to the low rotor impedance, a very high current is drawn for a short period, and does not damage the motor. This current, and consequently power, can be nearly 6 to 8 times the full load value [92]. The total power consumed by the motor during charging is 615.41 MWh.

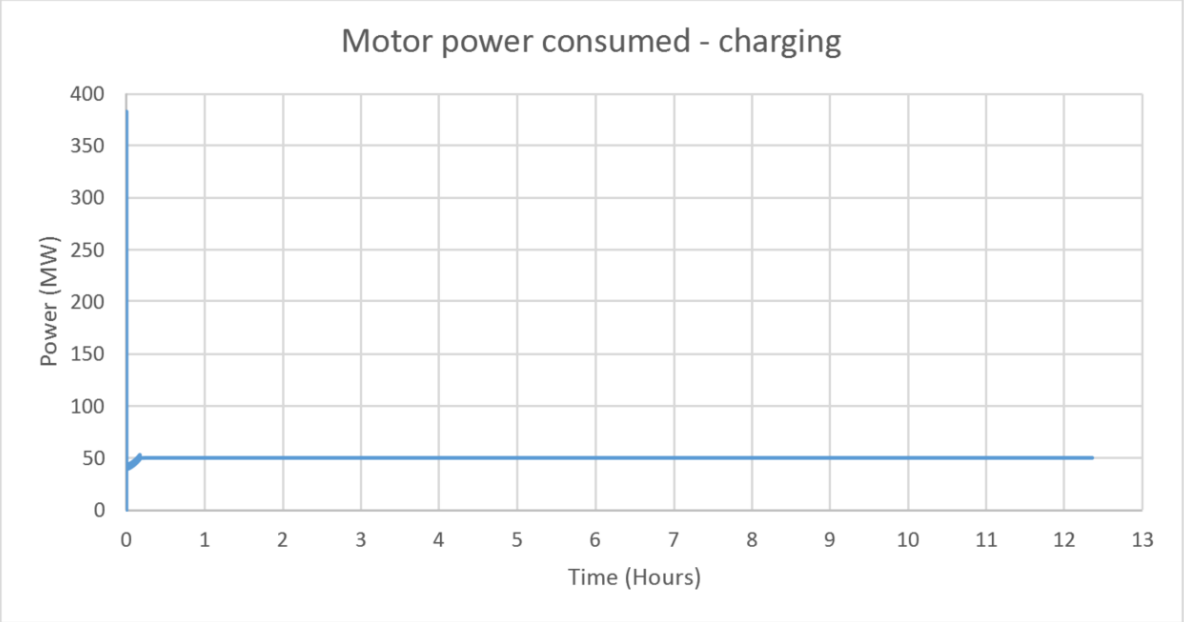

Figure 36 - Motor power consumed during charging

5.1.3 Thermal Energy Storage (TES)

The role of TES during charging is to cool the air after compression before entering the cavern. The desired TES outlet temperature during charging is 55°C. Figure 37 below shows the cumulative energy stored during the charging period. As expected, the plot shows no energy stored for the first 619 seconds followed by a linear increase in stored energy with time. There is no energy stored in the TES during the first 619 seconds because mass is not allowed to enter the device until the compressor has reached the desired operating point on its map, shown by point C2. This is to ensure the pressure at the outlet of the compressor is greater than the pressure in the cavern. The energy stored at the end of the charging period is 4.54 x 10^{12} J, and is used to heat the air entering the turbine during discharging.

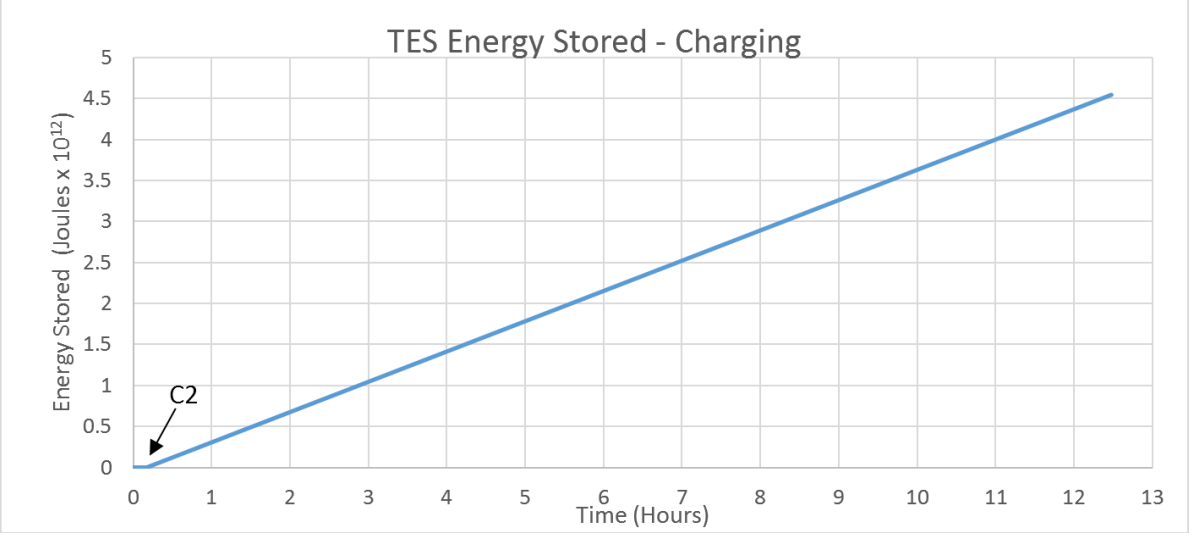

Figure 37 - TES energy stored during charging

5.1.4 Cavern

The cavern is the part of the CAES system that acts as the air storage reservoir. During the charging period, it receives pressurized air from the compressor after it has been cooled by the TES. The cavern is injected with pressurized air until the pressure in the cavern reaches its maximum allowable value. Figure 38 on the next page illustrates the change in cavern pressure during the charging period. From the figure it can be observed that cavern pressure decreases slightly, for the first 619 seconds, and then increases at a constant rate until it reaches 72 bar. The initial reduction in pressure can be attributed to a temperature reduction caused by heat lost to the cavern walls during compressor startup. The pressure at the beginning and end of the charging period is 42 and 72 bar respectively.

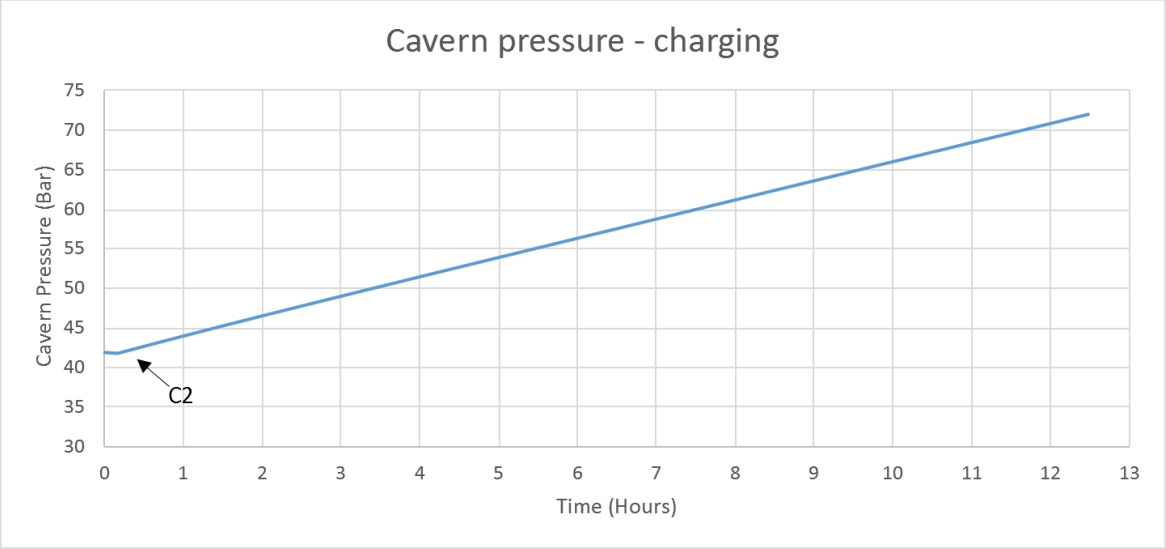

Figure 38 - Cavern pressure variation during charging

Figure 39 below illustrates the change in cavern temperature during the charging period. The initial cavern temperature is 35°C, after which the temperature rises to 53°C. Point C2 on the plot shows the point where the compressor has reached its desired operating point on its map. After this, mass is allowed to enter the cavern and this changes the rate of temperature increase. For the fist 619 seconds, heat is added from the cavern walls to the air in the cavern. At point C2, after passing through the TES, air enters the cavern at 55°C causing the rate of temperature increase to change within the cavern. The highest temperature encountered in cavern during charging is 53°C.

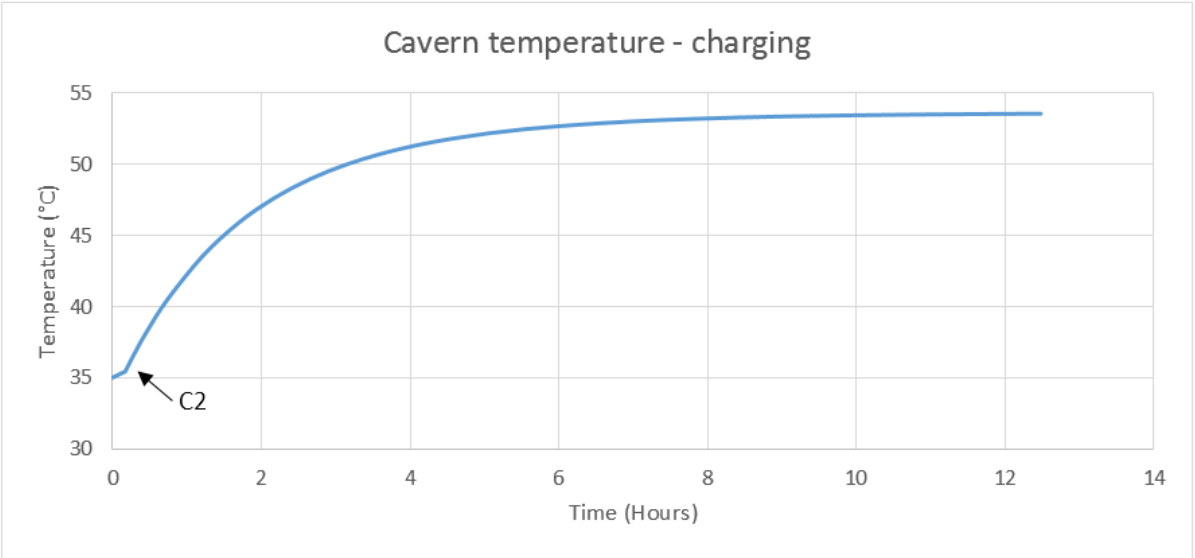

Figure 39 - Cavern temperature variation during charging

5.2 Storage

In the simulation, air is stored in the cavern for a period of 8 hours. The cavern is assumed to be leak proof and therefore, no mass of air is lost during the storage period. Figure 40 below illustrates the change in cavern pressure during the storage period. From the figure it can be observed that the cavern pressure reduces from 72 bar to 69.3 bar during the 8-hour storage period. This pressure loss is a direct consequence of the heat lost during the storage period since no mass is lost.

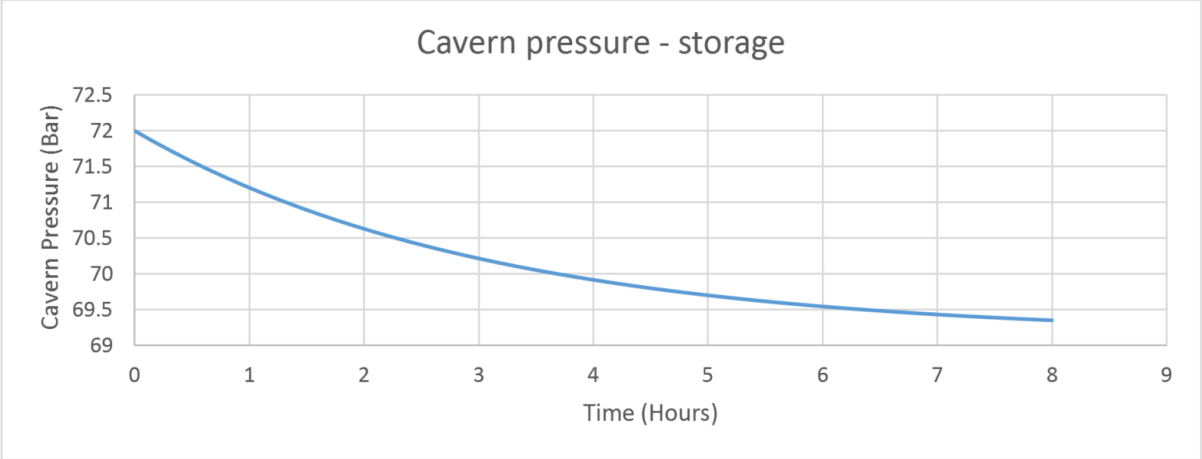

Figure 40 - Cavern pressure variation during storage

Figure 41 below illustrates the change in cavern temperature during the storage period. From the figure it can be observed that the cavern temperature reduces from 53°C to 40.9°C during the 8-hour storage period. The change in temperature can be attributed to the heat lost to the cavern wall, which is at 40°C, during the storage period. The cavern temperature is close to the cavern wall temperature at the end of the storage period.

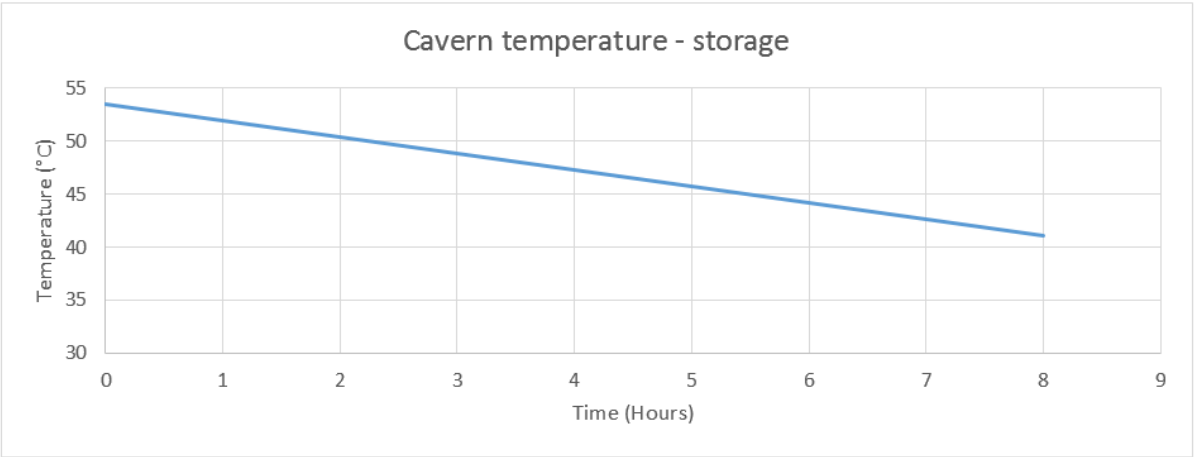

Figure 41 - Cavern temperature variation during storage

5.3 Discharging

After 8 hours of storage, the CAES system operates in discharge mode to produce power. The cavern pressure is decreased to 42 bar while a turbine simultaneously, produces power. The components of the system active during the discharge period are the turbine, the generator, the TES and the cavern. The following subsections present the results pertaining to each component.

5.3.1 Turbine

The turbine is used to convert the potential energy from compressed air in the cavern to rotational mechanical energy by expansion. The generator can then use this rotational mechanical energy to produce electricity for the grid. As described in [75], a turbine for CAES systems operates at a constant pressure ratio and does not require a starter motor. For this simulation, the turbine is operated until the pressure in the cavern reaches its minimum allowable value. Additionally, the load on the turbine is connected after 10 seconds, when the rotor is spinning at about 60% of its nominal speed. Figure 42 below illustrates the change in turbine mass flow rate during the discharge period.

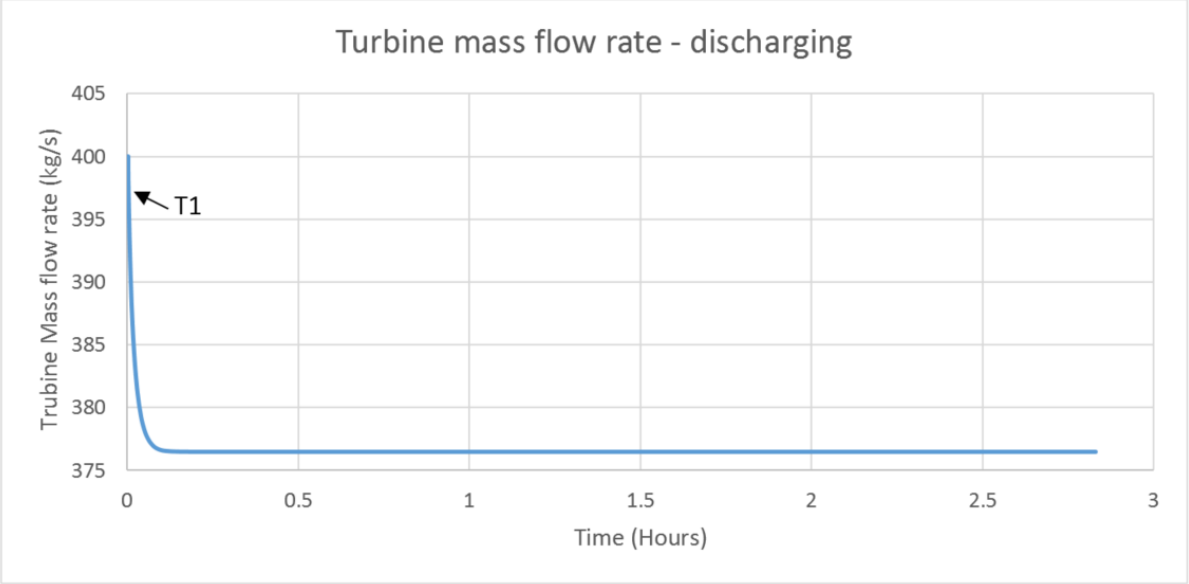

Figure 42 - Turbine mass flow rate during discharging

From the figure above it can be observed that the mass flow rate in the turbine initially begins at 400 kg/s, which is its nominal value. This happens because a large amount of power is required to start moving the turbine from rest. As the turbine speeds up, the mass flow rate then decreases and reaches a steady value of 376.45 kg/s in 760 seconds, which is about 94% of its nominal value. Point T1 represents the instance when the load is connected to the turbine. The turbine's operation with

respect to mass flow rate is as expected because, as per its performance map, an operating pressure ratio of 10 has a corresponding per unit mass flow rate of 94%.

Figure 43 below shows the change in the angular velocity of the turbine rotor during the discharge period. The turbine, has a nominal angular speed of 1780 rpm. From the figure it can be observed that the turbine first begins to spin from rest, after about 10 seconds the turbine reaches 60% of its nominal speed when the load is connected to it. This phenomenon is represented by point T1, and the rate of increase of angular speed is reduced when this happens. After about 760 seconds, the turbine angular speed reaches 100% of its nominal value. This is taken to be the startup time of the turbine. The turbine will accelerate or decelerate based on the difference between the load and its output shaft power.

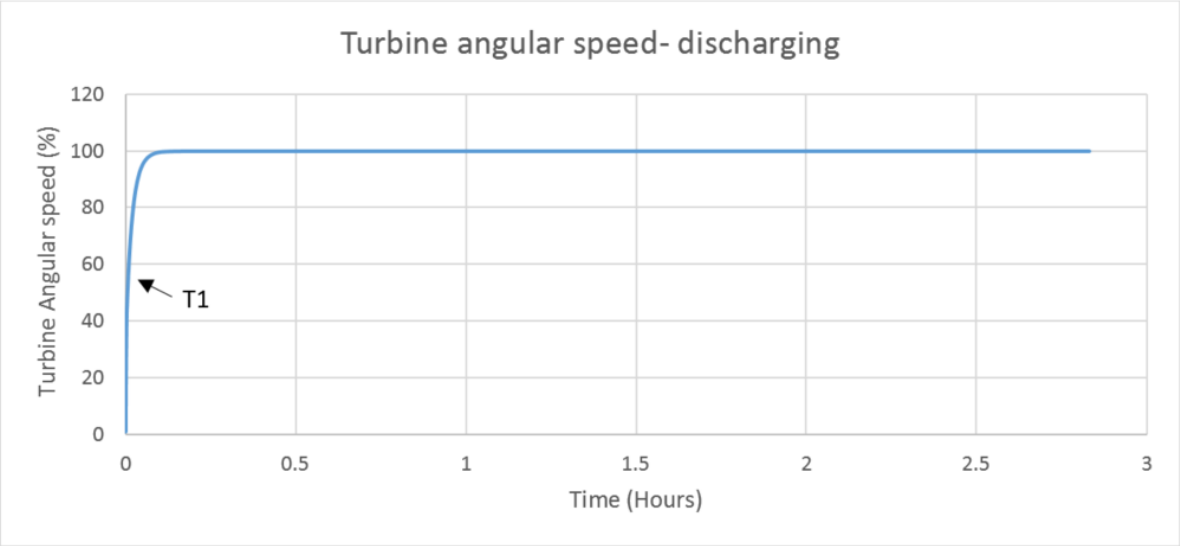

Figure 43 - Turbine angular speed during discharging

Figure 44 on the next page shows the change in efficiency of the turbine during the discharge period. From the figure it can be observed that the turbine efficiency starts at about 70%, peaks to approximately 87% during startup, and stabilizes to around 83% for the remainder of the discharge period. This happens because the turbine has high efficiencies for low angular speeds and high mass flow rates, as verified by the turbine performance maps. Initially, the turbine efficiency increases with increasing angular speed and high mass flow rate. However, after 10 seconds when the load is connected, the turbine efficiency stabilizes as dictated by the decrease in mass flow rate and increase in angular speed. An average efficiency of 81% is obtained during the simulation.

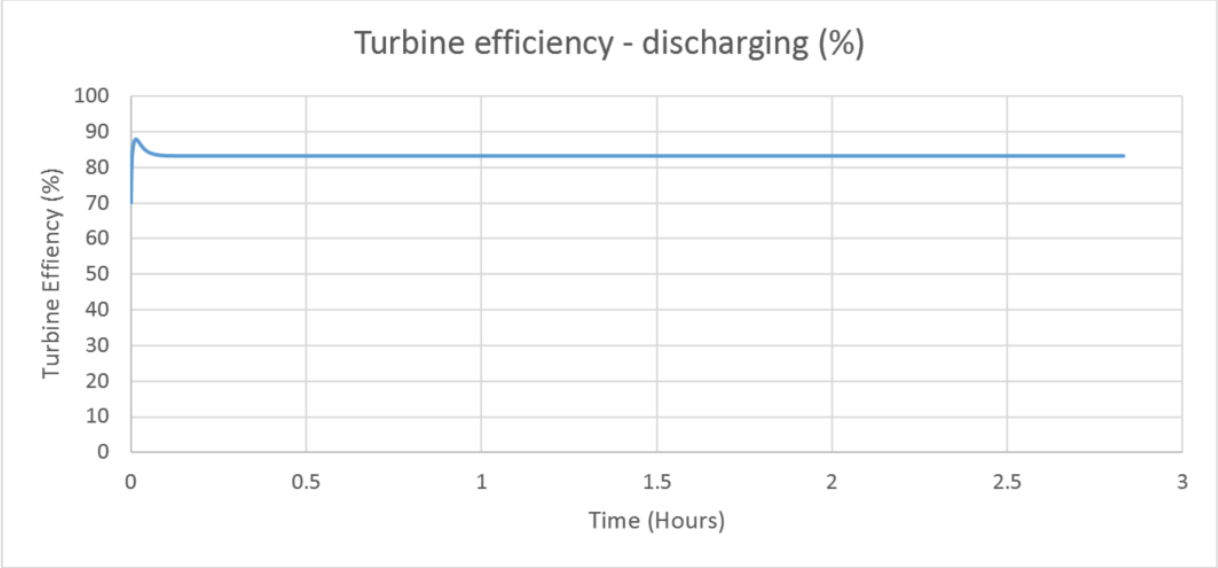

Figure 44 - Turbine efficiency during discharging

5.3.2 Generator

During discharging, the generator receives energy in the form of rotational mechanical energy from the turbine and sends energy to the grid in the form of electricity. Figure 45 below shows the power delivered to the grid during the discharge period by the generator. From the figure it can be observed that delivered power begins from zero, and stabilizes to about 167 MW, and remains constant for the duration of the discharge period. The total electrical power delivered by generator during the discharge period is 469.24 MWh.

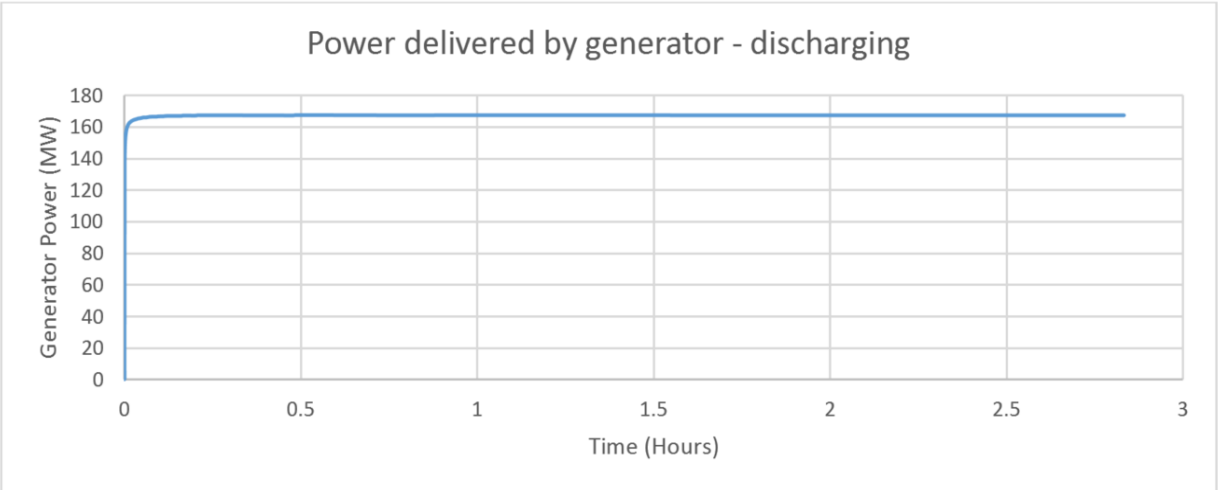

Figure 45 - Power delivered by generator during discharging

5.3.3 Thermal Energy Storage (TES)

During discharging, the role of the TES is opposite to what it was during charging. The TES heats the air after it leaves the cavern, before entering the turbine. The desired TES outlet temperature during discharging is 1300°C. Figure 46 below shows the cumulative energy used in raising the temperature of the air during the discharge period. As expected, the plot shows a linear increase in energy used with time. The total energy used at the end of the discharge period is 4.12 x 10^{12} J.

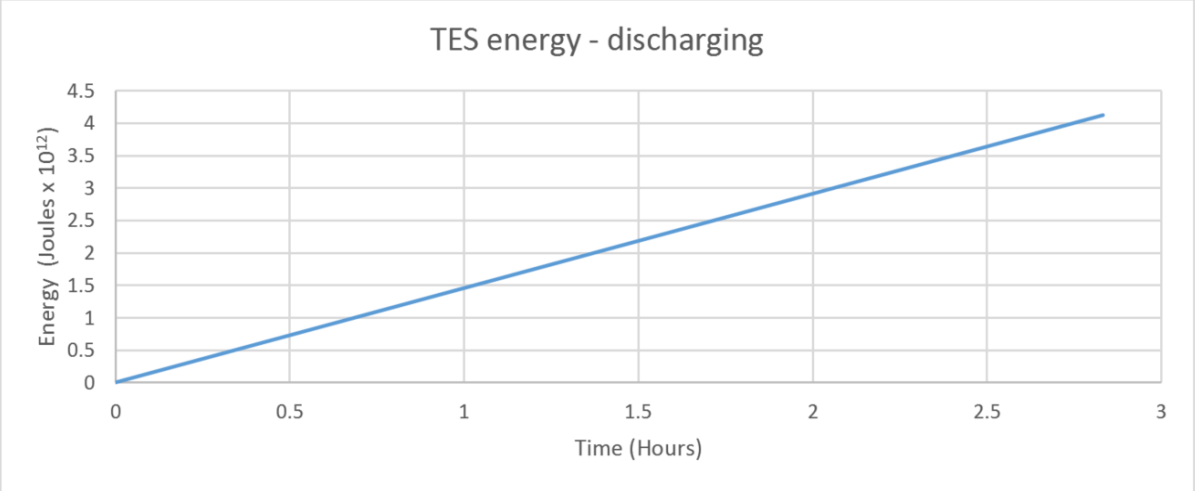

Figure 46 - TES energy used during discharging

5.3.4 Cavern

As previously discussed, the cavern is the part of the CAES system that acts as the air storage reservoir. During the discharging period, it sends pressurized air to the turbine for expansion so that the power produced from the expansion process can be sent to the grid. The cavern discharges pressurized air until its pressure reaches 42 bar. Figure 47 on the next page illustrates the change in cavern pressure during the discharge period. From the figure it can be observed that that the rate of pressure decrease is linear and nearly constant with respect to time. This can be attributed to the fact that after speeding up, the turbine discharges the cavern at a fairly constant rate. The pressure at the beginning and end of the discharging period is 69.3 and 42 bar respectively.

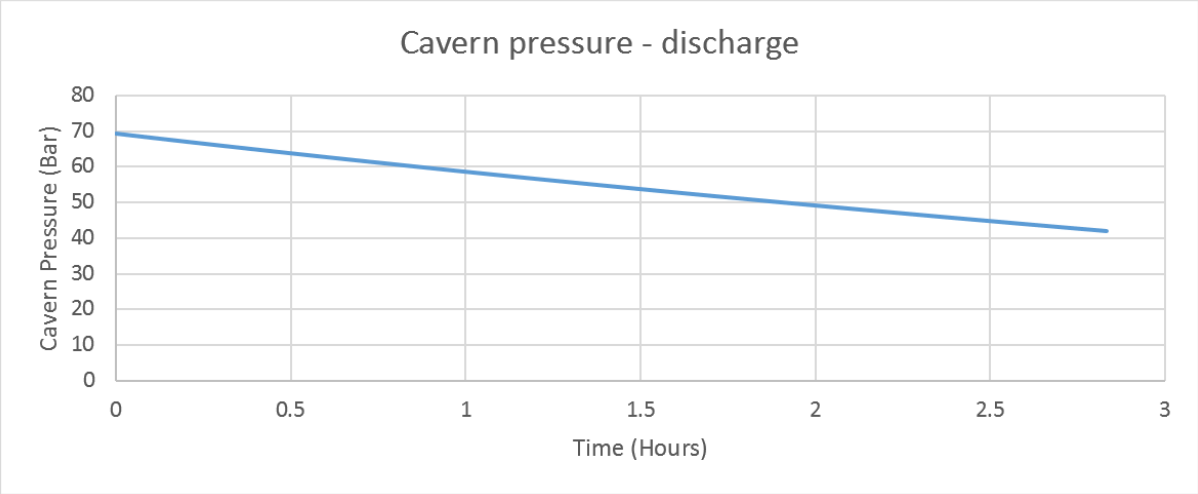

Figure 47 - Cavern pressure variation during discharge

Figure 48 below illustrates the change in cavern temperature during the discharging period. From the figure it can be observed that that the rate of temperature decrease is linear and nearly constant with respect to time. The temperature at the beginning and end of the discharge period is 40°C and 11°C respectively. These temperatures are similar to those observed at the Huntorf plant [53,54]. This low temperature in the cavern at the end of the discharge period is encountered because the rate of heat addition to cavern from its wall and its surroundings, is slower than the rate of heat removal due to discharging. Provided the next charge cycle does not happen immediately, the temperature of the cavern will increase with time. A study of what the ideal wait is before the next charge cycle is not in the scope of this work, however, it is a factor that must be taken into consideration by a CAES plant designer.

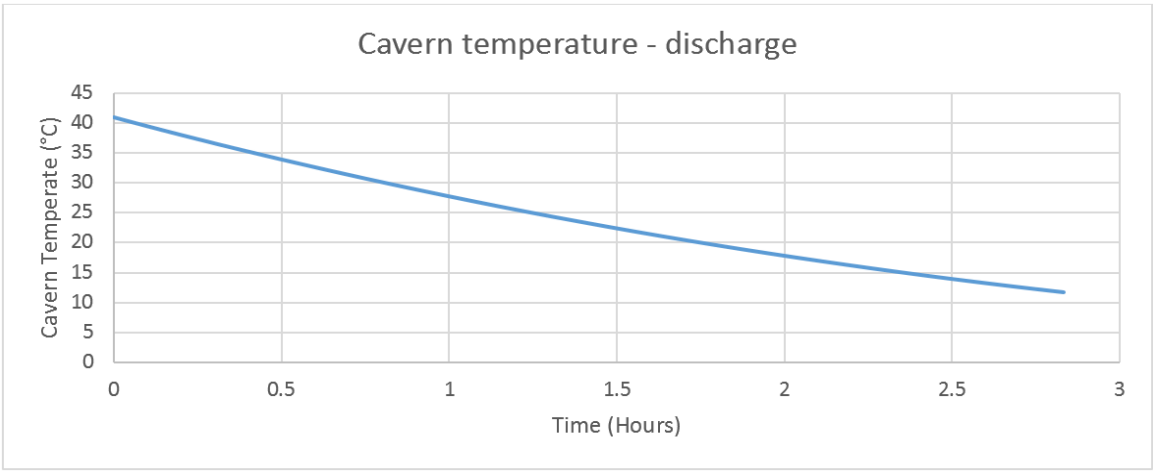

Figure 48 - Cavern temperature variation during discharge

5.4 Overall system results

In this section, the overall key results from the simulation will be presented and discussed. An A-CAES plant was simulated for 23.3 hours comprising of 12.47 hours of charging, 8 hours of storage and 2.83 hours of discharge. Figure 49 and Figure 50 below show the variation of cavern pressure and temperature for the cycle. Since the state of charge (SOC) of a CAES system is indicated by the pressure in the storage reservoir, Figure 49 can also be interpreted as the variation of system state of charge with time.

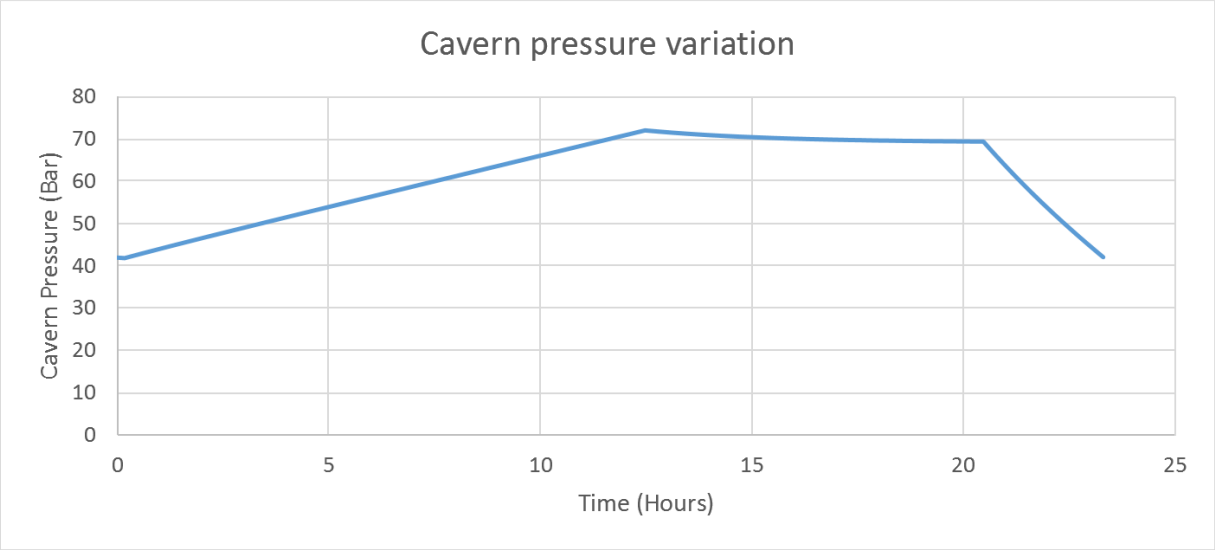

Figure 49 - Cavern pressure variation

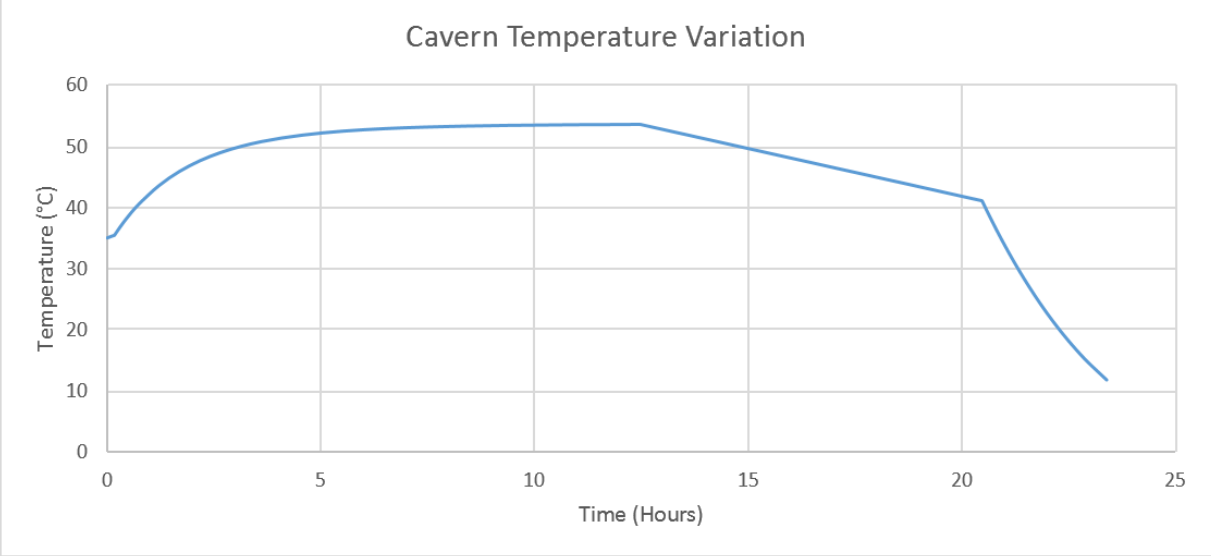

Figure 50 - Cavern temperature variation

Table 9 below summarizes the key results for the simulation. The obtained round trip efficiency of 76.24%, is similar to values published in literature [45, 50], and is higher than the Huntorf plant, which has a round trip efficiency of 42%. The charging and discharge mass flow rates simulated are within 1% of those found at the Huntorf plant.

Table 9 - Summary of results

Result	**Value**
Total power consumed	615.45 MWh
Total power produced	469.24 MWh
Round trip efficiency	76.24%
Compressor train average efficiency	70%
Turbine average efficiency	81%
TES efficiency	91%
Turbine start-up time	760 seconds
Charging mass flow rate	107.5 kg/s
Discharging mass flow rate	400 kg/s

Since there is no published information regarding the efficiencies of the turbines and compressors at the Huntorf plant, these values cannot be compared and commented on. However, they are found to be reasonable for the simulated conditions. In the next chapter, the key conclusions and outcomes from this work are discussed along with recommendations for future work.

Chapter 6
Conclusion and Recommendations

In this work, a technical review of energy storage systems is performed, a literature review on CAES and turbomachinery modeling is performed, and an A-CAES plant is modeled and simulated. The components of the CAES plant that are modeled are the compressor, the turbine, the TES, the cavern, the induction motor and the generator. The models use turbomachinery maps to model the behavior of the compressor and turbine, capturing the complex fluid mechanic phenomena that come about during machine operation. The rotational dynamics of the turbomachines are connected to the aforementioned map-based operation. Additionally, the compressor is connected to the induction motor driving it, and the turbine is connected to the generator. The inertias and friction losses present within each of these components, and their overall connected effect on the system, are captured. The novelty associated with this work is that the aforementioned operation of the compression and expansion train; is connected to cavern thermodynamics and a simple TES. Additionally, the models are made flexible, modular, and extensible; and will aid a CAES plant designer to obtain an accurate first order thermodynamic evaluation of a proposed CAES plant. In the following subsections, the key outcomes from the simulation results are discussed along with recommendations for model development and future work.

6.1 Conclusions

The main objective of this work is to develop a flexible and extensible model of a CAES system for bulk applications, that is dynamic and modular. Since no operational A-CAES plant exists today, the design and simulation of the model was based on adiabatic version of the Huntorf plant. From the simulated results, the following points summarize the main conclusions.

- The results show that an A-CAES plant with a TES can achieve a round trip efficiency of over 70%
- The models simulate the behavior of an A-CAES plant accurately capturing time dependent storage losses as well as start-up and part load behavior of turbomachinery; and the simulation can be run in a relatively short time
- The compressor and turbine models show a behavior that closely resembles their performance maps, therefore, their operation can be considered accurate

- It takes 12.47 hours to increase the pressure of a 150,000 m^3 underground cavern from 42 bar to 72 bar using an axial compressor having a nominal mass flow rate of 107.5 kg/s
- During the charging process, the average efficiency of the compressor train is 70%
- It takes 2.8 hours to decrease the pressure of a 150,000 m^3 underground cavern from 72 bar to 42 bar using a turbine having a nominal mass flow rate of 400 kg/s
- During the discharging process, the average efficiency of the expander train is 81%
- The consumed power by the A-CAES system is 615.45 MWh, and after storage, the produced power is 469.24 MWh leading to a system round trip efficiency of 76.24%
- For a 200 MW turbine with a design speed of 17000 rpm and nominal mass flow rate of 400 kg/s, the start-up time is 760 seconds
- The TES device operates with an efficiency of 91% and absorbs 4.54×10^{12} J of heat during the charging process and dispatches 4.12×10^{12} J of heat during the discharge process
- Although the current simulated scenario is that of the Huntorf plant, the model is flexible enough to simulate and study other charge and discharge scenarios using different turbomachinery, air storage, and TES devices
- The compressor and turbine models can simulate other turbomachines, provided there exists an operation or performance map associated with it

6.2 Limitations

To go with its benefits, the developed model also has limitations. They are outlined below. Eliminating these limitations can lead to an improved model fidelity and provide results that are closer to real world behavior.

- The compressor train currently uses a regulating system that ensures its safe operation, i.e. it does not operate in the surge or stall regions of its performance map. This system is currently not optimized to maximize efficiency, however, when optimized, an increase in round trip efficiency is expected
- The TES device in the model is a simple and ideal device, and does not take into account the specific losses that may influence the system when using a particular type of heat storage (for example, packed bed)
- The cavern pressure and temperature are represented by single values, meaning that the fluctuations of temperature and pressure within the geometry of the cavern is not captured

- The heat transfer between the cavern walls and surrounding rock is currently not calculated since specific information about the heat transfer coefficients of the rock surrounding of the Huntorf plant's cavern was not found in literature. However, the model can easily capture this phenomenon given the heat transfer coefficients
- The model assumes air behaves as an ideal gas however, since in the CAES operational cycle high pressures and low temperatures are encountered, certain deviations from ideal gas behavior can be expected
- The model uses the beta lines method to read axial turbomachinery operation maps with good accuracy. However, if a compressor with variable inlet guide vanes and constant speed is desired to be modeled, an operation map would be required that contains a relation between the compressor angular speed changes with the inlet guide vane angle. Such maps are difficult to obtain and an alternate modeling methodology may have to be considered

6.3 Recommendations for future work

In this thesis, an A-CAES plant was modeled and simulated. The intended use of this model is to assist with the design process of future A-CAES plants. Keeping in mind the existing limitations in this work as mentioned in the previous subsection, the following recommendations can be made for future work.

- An economic model that captures the change in electricity price and demand can be connected to the developed models so that future CAES plants are thermo-economically optimized. Furthermore, this addition will facilitate the study of CAES plants in various energy markets and justify their initial capital investment.
- It is recommended to study how to make best use of the waste heat from the expansion process. This heat can be potentially utilized by domestic homes for space heating or be used by an industrial process
- Property models of air can be added to the current CAES model to increase the overall model fidelity and accurately estimate temperatures and pressures within the system. It is recommended to incorporate the Soave-Redlich-Kwong-Kabadi-Danner (SRK-KD) model for the thermodynamic properties of humid air, the Lucas model to calculate dynamic viscosity, and the Stiel-Thodos model for calculating thermal conductivity

- Integration with other renewable energy technologies such as solar thermal power plants or polygeneration plants can be studied. In such models, a shared heat storage can be incorporated for
- An exergy destruction analysis of the system can be added to the model functionality. This can possibly reveal which components within the system can be considered the weak links leading to focused optimization of those components
- It is recommended to replace the current TES device in the model with a specific high fidelity model of a particular type of heat storage (such as packed bed heat storage) to better capture its interaction with the rest of the system
- To add the effects of variable turbomachinery geometry for performance, as well as operation of the system
- Incorporate overall control strategy to the model in order to maximize component level and system level efficiency
- Use of different turbomachinery and their respective drivers for the study of CAES for short term services such a frequency regulation and spinning reserve
- The cavern model can be expanded to capture the fluctuations in air temperature and pressure with cavern depth
- Within the model, it is recommended to conduct experimental simulations using different kinds of air storage devices (underground, above ground, etc.), different types of turbomachinery (axial, centrifugal, etc.), as well as different types of motors and generators (synchronous, asynchronous, etc.) in order to understand which combination of components under what configuration suits a particular energy storage scenario best
- Since no A-CAES plants have been realized in the world today, it is recommended to develop a laboratory scale A-CAES plant so that results from simulations can be compared with results from performed experiments
- Since the models are easily scalable, its recommended to study the application of CAES for micro grid purposes and de-centralized grid management
- It is recommended to study the suitability of diesel and reciprocating engines in the expansion train for CAES

References

[1] 2015 key world energy statistics. IEA – International Energy Agency. (2015). Retrieved June, 2018, from https://www.iea.org/publications/freepublications/publication/key-world-energy-statistics-2015.html

[2] Fares, R. (2015, March 11). Renewable Energy Intermittency Explained: Challenges, Solutions, and Opportunities. Retrieved June, 2018, from https://blogs.scientificamerican.com/plugged-in/renewable-energy-intermittency-explained-challenges-solutions-and-opportunities

[3] Abdelrahman, A., Lamont, L., &Chaar, L. E. (2012). Energy Storage for Intermittent Renewable Energy Systems. 2nd World Sustainablity Foum. Retrieved June, 2018, from https://sciforum.net/manuscripts/972/manuscript.pdf

[4] Rugolo, J., & Aziz, M. J. (2012). Electricity storage for intermittent renewable sources. *Energy & Environmental Science, 5(5),* 7151-7060. doi:10.1039/c2ee02542f

[5] Nigim, K., & Reiser, H. (2009). Energy storage for renewable energy combined heat, power and hydrogen fuel (CHPH2) infrastructure. *2009 IEEE Electrical Power & Energy Conference (EPEC).* doi:10.1109/epec.2009.5420881

[6] Alamri, B., & Alamri, A. (2009). Technical review of energy storage technologies when integrated with intermittent renewable energy. *2009 International Conference on Sustainable Power Generation and Supply*. doi:10.1109/supergen.2009.5348055

[7] FERC: Guide to Market Oversight - Glossary. (2016, March 15). Retrieved June, 2018, from https://www.ferc.gov/market-oversight/guide/glossary.asp

[8] Rebours, Y. G., Kirschen, D. S., Trotignon, M., & Rossignol, S. (2007). A Survey of Frequency and Voltage Control Ancillary Services—Part I: Technical Features. *IEEE Transactions on Power Systems, 22(1),* 350-357. doi:10.1109/tpwrs.2006.888963

[9] Masters, G. M. (2013). *Renewable and Efficient Electric Power Systems*. Hoboken, NJ: Wiley-Blackwell.

[10] Uddin, M., Romlie, M. F., Abdullah, M. F., Halim, S. A., Bakar, A. H., & Kwang, T. C. (2018). A review on peak load shaving strategies. *Renewable and Sustainable Energy Reviews, 82,* 3323-3332. doi:10.1016/j.rser.2017.10.056

[11] Cleveland, C. J. (2004). *Encyclopedia of energy*. Volumes 1 - 6. Amsterdam: Elsevier, Acad. Press. ISBN 978-0-12-176480-7.

[12] Jonathan R. (2013). *Energy storage technologies*. Ingenia 2013:27–32.

[13] Mahlia, T., Saktisahdan, T., Jannifar, A., Hasan, M., & Matseelar, H. (2014). A review of available methods and development on energy storage; technology update. *Renewable and Sustainable Energy Reviews*, 33, 532-545. doi:10.1016/j.rser.2014.01.068

[14] Zhou, Z., Benbouzid, M., Charpentier, J. F., Scuiller, F., & Tang, T. (2013). A review of energy storage technologies for marine current energy systems. *Renewable and Sustainable Energy Reviews*, 18, 390-400. doi:10.1016/j.rser.2012.10.006

[15] Carbon Fiber Flywheels. (n.d.). Retrieved June, 2018, from http://beaconpower.com/carbon-fiber-flywheels

[16] Grond, L., Schulze, P., & Holstein, J. (2013, June 20). DNV KEMA Systems Analyses Power to Gas a Technology Review. Retrieved June, 2018, from https://www.scribd.com/document/328966622/DNV-KEMA-Systems-Analyses-Power-to-Gas-a-Technology-Review

[17] Hasan, N. S., Hassan, M. Y., Majid, M. S., & Rahman, H. A. (2013). Review of storage schemes for wind energy systems. *Renewable and Sustainable Energy Reviews*, 21, 237-247. doi:10.1016/j.rser.2012.12.028

[18] Chen, H., Cong, T. N., Yang, W., Tan, C., Li, Y., & Ding, Y. (2009). Progress in electrical energy storage system: A critical review. *Progress in Natural Science*, 19(3), 291-312. doi:10.1016/j.pnsc.2008.07.014

[19] Sandén, B., Systems perspectives on renewable power,(2014). Retrieved June, 2018, from http://www.chalmers.se/en/areas-of-advance/energy/documents/Systems%20Perspectives%20on%20Biorefineries/Systems_Perspecticves_on_Renewable_Power_2014_v1.1.pdf

[20] International Energy Agency. Technology roadmap - energy storage. (2014). Report, IEA, 2014. Retrieved June, 2018, from http://www.iea.org/publications/freepublications/publication/TechnologyRoadmapEnergystorage.pdf.

[21] Pumped Hydro Storage - The Ups and Downs of Water. (n.d.). Retrieved June, 2018, from http://www.alternative-energy-tutorials.com/energy-articles/pumped-hydro-storage.html

[22] A project implemented by Consortium MVV decon/ENEA/RTE I/Terna/Sonelgaz. Paving the way for the mediterranean solar plan - state-of-play of large storage technologies: design and application consideration. (2010) Report 248-486, ENIP. Retrieved June, 2018, from https://library.euneighbours.eu/sites/default/files/attachments/Inception-Report.pdf.

[23] Luo, X., Wang, J., Dooner, M., & Clarke, J. (2015). Overview of current development in electrical energy storage technologies and the application potential in power system operation. *Applied Energy*, 137, 511-536. doi:10.1016/j.apenergy.2014.09.081

[24] Wann, A., Leahy, P., Reidy, M., Doyle, S., Dalton, H., Barry, P,. (2012). Environmental performance of existing energy storage installations. Retrieved June, 2018, from http://www.store project.eu/documents/results/en_GB/environmental-performance-of-existing-energy-storage-installations

[25] Guney, M. S., & Tepe, Y. (2017). Classification and assessment of energy storage systems. *Renewable and Sustainable Energy Reviews*, 75, 1187-1197. doi:10.1016/j.rser.2016.11.102

[26] Root, M. (2011). *The TAB battery book: An in-depth guide to construction, design*, and use ;. New York: McGraw-Hill.

[27] Linden, S. V. (2006). Bulk energy storage potential in the USA, current developments and future prospects. *Energy*, 31(15), 3446-3457. doi:10.1016/j.energy.2006.03.016

[28] NGK INSULATORS. (n.d.). *Specs*. Retrieved June, 2018 from https://www.ngk.co.jp/nas/specs/

[29] Du, P., & Lu, N. (2015). *Energy storage for smart grids: Planning and operation for renewable and variable energy resources (VERs).* Amsterdam u.a.: Elsevier u.a. ISBN 978-0-2-410491-4.

[30] Lithium Ion (LI-ION) Batteries. (n.d.). Retrieved June, 2018 from http://energystorage.org/energy-storage/technologies/lithium-ion-li-ion-batteries

[31] Zhao, H., Wu, Q., Hu, S., Xu, H., & Rasmussen, C. N. (2015). Review of energy storage system for wind power integration support. *Applied Energy*, 137, 545-553. doi:10.1016/j.apenergy.2014.04.103

[32] Hadjipaschalis, I., Poullikkas, A., & Efthimiou, V. (2009). Overview of current and future energy storage technologies for electric power applications. *Renewable and Sustainable Energy Reviews,*13(6-7), 1513-1522. doi:10.1016/j.rser.2008.09.028

[33] Khaligh, A., & Li, Z. (2010). Battery, Ultracapacitor, Fuel Cell, and Hybrid Energy Storage Systems for Electric, Hybrid Electric, Fuel Cell, and Plug-In Hybrid Electric Vehicles: State of the Art. *IEEE Transactions on Vehicular Technology*, 59(6), 2806-2814. doi:10.1109/tvt.2010.2047877

[34] J. K. Kaldellis. Stand-Alone and Hybrid Wind Energy Systems - Technology, Energy Storage and Applications. Woodhead Publishing, 2010. ISBN 978-1-84569-527-9.

[35] Uner D Storage of Chemical Energy and Nuclear Materials, Energy storage systems-Volume II., UNESCO-EOLSS sample chapters.

[36] Niaz S, Manzoor T, Pandith AH. Hydrogen storage: materials, methods and perspectives. Renew Sustain Energy Rev 2015;50:457–69.

[37] Ter-Gazarian, A. G. (2008). *Energy storage for power systems (2nd Edition)*. Stevenage: The Institution of Engineering and Technology. ISBN 978-1-84919-219-4

[38] Hydrogen Storage. (n.d.). Retrieved June, 2018, from https://www.energy.gov/eere/fuelcells/hydrogen-storage

[39] Barbir, F. (2013). *PEM fuel cells: Theory and practice*. Amsterdam: Elsevier/Academic Press. ISBN 978-0-12-387710-9.

[40] Dunne, L. J., Brändas, E. J., & Cox, H. (2017). High-Temperature Superconductivity in Strongly Correlated Electronic Systems. Advances in Quantum Chemistry Löwdin Volume, 183-208. doi:10.1016/bs.aiq.2016.06.003

[41] Molina, M. G. (2010). Dynamic Modelling and Control Design of Advanced Energy Storage for Power System Applications. *Dynamic Modelling*. doi:10.5772/7092

[42] Wasterlain, S., A. Guven, H. Gualous, J. F. Fauvarque, and R. Gallay. (2006). Hybrid power source with batteries and supercapacitor for vehicle applications. Retrieved June, 2018, from https://www.researchgate.net/publication/228400689_Hybrid_power_source_with_batteries_and_supercapacitor_for_vehicle_applications/citations

[43] Ibrahim, H., Ilinca, A., & Perron, J. (2008). Energy storage systems—Characteristics and comparisons. *Renewable and Sustainable Energy Reviews*, 12(5), 1221-1250. doi:10.1016/j.rser.2007.01.023

[44] Kalhammer, F. R., & Schneider, T. R. (1976). Energy Storage. *Annual Review of Energy*, 1(1), 311-343. doi:10.1146/annurev.eg.01.110176.001523.

[45] Budt, M., Wolf, D., Span, R., & Yan, J. (2016). A review on compressed air energy storage: Basic principles, past milestones and recent developments. *Applied Energy*, 170, 250-268. doi:10.1016/j.apenergy.2016.02.108

[46] Herbst, CH., Hoffeins, H., Stys, Z. (1983). Air storage system energy transfer (ASSET) plants. *Proceedings of the IEEE*, 71(9), 1079-1085. doi:10.1109/proc.1983.12725

[47] Allen, R., Doherty, T., & Kannberg, L. (1985). Summary of selected compressed air energy storage studies. *Washington: Richland.* doi:10.2172/5872515

[48] Goodson, J. O. (1992). *History of first U.S. compressed air energy storage (CAES) plant (110-MW-26 h).* Palo Alto, CA: EPRI.

[49] Discover renewable energy technology with compressed air energy storage. (2017). Retrieved June, 2018, from https://www.pge.com/en_US/about-pge/environment/what-we-are-doing/compressed-air-energy-storage/compressed-air-energy-storage.page

[50] Wolf D. (2011). Methods for design and application of adiabatic compressed air energy: storage based on dynamic modeling. Oberhausen: Laufen.

[51] Sander, F., Span, R. (2006). First Results of an Adiabatic Compressed Air Energy Storage Power Plant in Laboratory Scale. Poster presented at: Latsis-Symposium 2006, ETH Zürich, Zürich, p. 1.

[52] Glendenning, I., Chew, P.E., Grant, R., Glanville, R., Moye, M.H. (1979). Technical and Economic Assessment of Advanced Compressed Air Storage (ACAS) Concepts, , *CEGB - Central Electricity Generation Board, England for EPRI - Electric Power Research Institute*, Palo Alto, CA, pp. 519.

[53] Radgen P. (2008). 30 years compressed air energy storage plant huntorf – experiences and outlook. *3rd international renewable energy storage conference*. Berlin; p. 18.

[54] Kraftwerk Huntorf. (2018). Retrieved July 2018 from http://www.energystorageexchange.org/projects/1245

[55] Fort, J. (1982). CAESCAP: A computer code for compressed-air energy-storage-plant cycle analysis. *Pacific Northwest Laboratories*. doi:10.2172/6884930

[56] Fort, J. (1983). Thermodynamic Analysis of Five Compressed Air Energy Storage Cycles. *Pacific Northwest Laboratories*. doi:10.2172/6487527

[57] Xia, T., He, L., An, N., Li, M., & Li, X. (2014). Electromechanical transient modeling research of energy storage system based on power system security and stability ananlysis *2014 International Conference on Power System Technology.* doi:10.1109/powercon.2014.6993587.

[58] Dahraie, M. V., Najafi, H. R., Azizkandi, R. N., & Nezamdoust, M. R. (2012). Study on compressed air energy storage coupled with a wind farm. *2012 Second Iranian Conference on Renewable Energy and Distributed Generation*. doi:10.1109/icredg.2012.6190452

[59] Hasan, N. S., Hassan, M. Y., Majid, M. S., & Rahman, H. A. (2012). Mathematical model of Compressed Air Energy Storage in smoothing 2MW wind turbine. *2012 IEEE International Power Engineering and Optimization Conference*. doi:10.1109/peoco.2012.6230886

[60] Martinez, M., Molina, M. G., Frack, P. F., & Mercado, P. E. (2013). Dynamic Modeling, Simulation and Control of Hybrid Energy Storage System Based on Compressed Air and Supercapacitors. *IEEE Latin America Transactions, 11(1),* 466-472. doi:10.1109/tla.2013.6502847

[61] Liu, W., Xu, G., & Yang, Y. (2014). Thermo-Dynamical Analysis on Electricity-Generation Subsystem of CAES Power Plant. J*ournal of Power and Energy Engineering, 02(04),* 729-734. doi:10.4236/jpee.2014.24097

[62] Sciacovelli, A., Li, Y., Chen, H., Wu, Y., Wang, J., Garvey, S., & Ding, Y. (2017). Dynamic simulation of Adiabatic Compressed Air Energy Storage (A-CAES) plant with integrated thermal storage – Link between components performance and plant performance. *Applied Energy,* 185, 16-28. doi:10.1016/j.apenergy.2016.10.058

[63] Grazzini, G., & Milazzo, A. (2012). A Thermodynamic Analysis of Multistage Adiabatic CAES. *Proceedings of the IEEE,* 100(2), 461-472. doi:10.1109/jproc.2011.2163049

[64] Jubeh, N. M., & Najjar, Y. S. (2012). Green solution for power generation by adoption of adiabatic CAES system. *Applied Thermal Engineering*, 44, 85-89. doi:10.1016/j.applthermaleng.2012.04.005

[65] Guo, Z., Deng, G., Fan, Y., & Chen, G. (2016). Performance optimization of adiabatic compressed air energy storage with ejector technology. *Applied Thermal Engineering*, 94, 193-197. doi:10.1016/j.applthermaleng.2015.10.047

[66] Hartmann, N., Vöhringer, O., Kruck, C., & Eltrop, L. (2012). Simulation and analysis of different adiabatic Compressed Air Energy Storage plant configurations. *Applied Energy,* 93, 541-548. doi:10.1016/j.apenergy.2011.12.007

[67] Xiaoshu, Z., & Hong, Z. (2015). Switched reluctance motor/generator simulation research based on compressed air energy storage system. *2015 International Conference on Advanced Mechatronic Systems (ICAMechS).* doi:10.1109/icamechs.2015.7287158

[68] Martinez, M., Molina, M. G., & Mercado, P. E. (2010). Dynamic performance of compressed air energy storage (CAES) plant for applications in power systems. *2010 IEEE/PES Transmission and Distribution Conference and Exposition: Latin America (T&D-LA).* doi:10.1109/tdc-la.2010.5762928

[69] Yu, Q., & Cai, M. (2013). The process of compressed air energy storage (CAES) analysis. *2013 International Conference on Materials for Renewable Energy and Environment.* doi:10.1109/icmree.2013.6893822

[70] Rowen, W. I. (1983). Simplified Mathematical Representations of Heavy-Duty Gas Turbines. *Journal of Engineering for Power, 105(4),* 865. doi:10.1115/1.3227494.

[71] De Mello, F. P., & Ahner, D. J. (1994). Dynamic models for combined cycle plants in power system studies. *IEEE Transactions on Power Systems*, 9(3), 1698-1708. doi:10.1109/59.336085

[72] Al-Hamdan, Q. Z., & Ebaid, M. S. (2006). Modeling and Simulation of a Gas Turbine Engine for Power Generation. *Journal of Engineering for Gas Turbines and Power, 128(2*), 302. doi:10.1115/1.2061287

[73] Bettocchi, R., Spina, P. R., & Fabbri, F. (1996). Dynamic Modeling of Single-Shaft Industrial Gas Turbine. *Volume 4: Heat Transfer; Electric Power; Industrial and Cogeneration.* doi:10.1115/96-gt-332

[74] Crosa, G., Pittaluga, F., Martinengo, A. T., Beltrami, F., Torelli, A., & Traverso, F. (1996). Heavy-Duty Gas Turbine Plant Aerothermodynamic Simulation Using Simulink. *ASME 1996 Turbo Asia Conference*. doi:10.1115/96-ta-022

[75] Gonzalez-Gonzalez, J. (2018, February 20). Modelling Axial Turbomachinery for Cmpressed Air Energy Storage. Retrieved June 2018 from https://uwspace.uwaterloo.ca/handle/10012/13032

[76] Walsh, P. P., & Fletcher, P. (2008). *Gas turbine performance, 2nd edition*. Oxford: Blackwell Science.

[77] Cohen, H., Rogers, G. F., & Saravanamuttoo, H. I. (1987). *Gas turbine theory, 4th edition*. New York: Longman Scientific & Technical.

[78] Estill, J. (2008). Turbocharger Compressor Calculations. Retrieved June, 2018, from http://www.gnttype.org/techarea/turbo/turboflow.html

[79] Razak, A. M. (2007). *Industrial gas turbines: Performance and operability*. Boca Raton: CRC Press.

[80] Tavakoli, S., Griffin, I., & Fleming, P. (2004). An Overview of Compressor Instabilities: Basic Concepts and Control. *IFAC Proceedings Volumes*, 37(6), 523-528. doi:10.1016/s1474-6670(17)32228-0

[81] Kushnir, R., Ullmann, A., & Dayan, A. (2012). Thermodynamic Models for the Temperature and Pressure Variations Within Adiabatic Caverns of Compressed Air Energy Storage Plants. *Journal of Energy Resources Technology*, 134(2), 021901. doi:10.1115/1.4005659

[82] Veres, J. (2009). Axial and Centrifugal Compressor Mean Line Flow Analysis Method. *47th AIAA Aerospace Sciences Meeting including The New Horizons Forum and Aerospace Exposition*. doi:10.2514/6.2009-1641

[83] Mazloum, Y., Sayah, H., & Nemer, M. (2016). Static and Dynamic Modeling Comparison of an Adiabatic Compressed Air Energy Storage System. *Journal of Energy Resources Technology*,138(6), 062001. doi:10.1115/1.4033399.

[84] Nelson, S. A., Filipi, Z. S., & Assanis, D. N. (2003). The Use of Neural Nets for Matching Fixed or Variable Geometry Compressors With Diesel Engines. *Journal of Engineering for Gas Turbines and Power, 125(*2), 572. doi:10.1115/1.1563239

[85] Moraal, P., & Kolmanovsky, I. (1999). Turbocharger Modeling for Automotive Control Applications. *SAE Technical Paper Series.* doi:10.4271/1999-01-0908

[86] Orkisz, M., & Stawarz, S. (2000). Modeling of Turbine Engine Axial-Flow Compressor and Turbine Characteristics. *Journal of Propulsion and Power, 16(2*), 336-339. doi:10.2514/2.5574

[87] Kurzke, J. (1996). How to Get Component Maps for Aircraft Gas Turbine Performance Calculations. *Volume 5: Manufacturing Materials and Metallurgy; Ceramics; Structures and Dynamics; Controls, Diagnostics and Instrumentation; Education; General*. doi:10.1115/96-gt-164

[88] Xia, C., Zhou, Y., Zhou, S., Zhang, P., & Wang, F. (2015). A simplified and unified analytical solution for temperature and pressure variations in compressed air energy storage caverns. *Renewable Energy*, 74, 718-726. doi:10.1016/j.renene.2014.08.058

[89] Asynchronous (Induction) Generators. (2013). Retrieved June, 2018, from http://xn--drmstrre-64ad.dk/wp-content/wind/miller/windpower web/en/tour/wtrb/async.htm

[90] Asynchronous Machine. (2006). Mathworks R2017b Documentation, MATLAB. Retrieved June, 2018, from https://www.mathworks.com/help/physmod/sps/powersys/ref/asynchronousmachine.html

[91] Bowman, C. W., Marceau, R. J., & Griesbach, R. C. (2009). Report of the Canada Power Grid Task Force Volume II – Background and Assessment. Electricity: Interconnecting Canada A Strategic Advantage. Retrieved July, 2018, from https://www.cae-acg.ca/wp content/uploads/2014/01/2010_Power Grid Task Force Vol 2.pdf. ISBN 978-0-9730830-6-4

[92] Garg, A., & Tomar, A. (2015). Starting Time Calculation for Induction Motor. *Journal of Electrical & Electronic Systems, 04(02*). doi:10.4172/2332-0796.1000149

[93] Kurzke, J., & Riegler, C. (2000). A New Compressor Map Scaling Procedure for Preliminary Conceptional Design of Gas Turbines. *Volume 1: Aircraft Engine; Marine; Turbomachinery; Microturbines and Small Turbomachinery*. doi:10.1115/2000-gt-0006

[94] Ma, W., Yongwen, L., & Ming, S. (2007). New scaling method for compressor maps using average infinitesimal stage. *Chinese Journal of Mechanical Engineering (English Edition), 20(06*), 24. doi:10.3901/cjme.2007.06.024

[95] Gholamrezaei, M., & Ghorbanian, K. (2009). Compressor map generation using a feed-forward neural network and rig data. *Proceedings of the Institution of Mechanical Engineers, Part A: Journal of Power and Energy, 224(*1), 97-108. doi:10.1243/09576509jpe792

[96] Tsoutsanis, E., Meskin, N., Benammar, M., & Khorasani, K. (2014). An Efficient Component Map Generation Method for Prediction of Gas Turbine Performance. *Volume 6: Ceramics; Controls, Diagnostics and Instrumentation; Education; Manufacturing Materials and Metallurgy.* doi:10.1115/gt2014-25753

[97] Kong, C., Ki, J., & Kang, M. (2003). A New Scaling Method for Component Maps of Gas Turbine Using System Identification. *Journal of Engineering for Gas Turbines and Power, 125(4),* 979. doi:10.1115/1.1610014

Appendix – Map scaling

Turbomachinery maps are a representation of the phenomenon occurring in a turbomachine. Each turbomachinery map is created for a particular machine, created typically by the manufacturer of the machine by conducting expensive tests in laboratories. Therefore, for the purposes of modeling the behavior of a turbomachine, it becomes difficult to find a turbomachinery map that fits the required system parameters in terms of mass flow rates, pressure ratios, etc.

The scaling of turbomachinery maps is a practice that has existed for several years and shown good results [76]. In literature, a variety of turbomachinery scaling methods can be found ranging from linear scaling methods, which are simple in nature [93,94], to complex methods that require a number of iterations or neural networks [95,96]. Since this work does not focus on the accurate scaling of maps, a relatively simple method, as described by Kong et al. [97] is selected. This method has an accuracy of 6% or less, and has been used successfully for scaling turbomachinery maps for CAES applications by [75]. Turbomachinery maps contain within them information pertaining the machines pressure ratio, mass flow rate and efficiency. When using the scaling method, the factors described by equations (32), (33) and (34) below must first be obtained. Once the map is scaled, so does its corresponding data associated with its beta lines.

$$PR_{Factor} = \frac{PR_D - 1}{PR_{MD} - 1}\,(PR_M - 1) + 1 \tag{32}$$

$$\dot{m}_{Factor} = \frac{\dot{m}_D}{\dot{m}_{MD}}\dot{m}_M \tag{33}$$

$$\eta_{Factor} = \frac{\eta_D}{\eta_{MD}}\eta_M \tag{34}$$

Where PR_{Factor} is the pressure ratio factor that relates the original map and the scaled map. PR_D is the desired pressure ratio of the scaled map. PR_{MD} is the pressure ratio at the design point of the original map. $PR_M$is an arbitrarily selected pressure ratio from the original map. $\dot{m}_{Factor}$ is the mass flow rate factor that relates the original map and the scaled map. $\dot{m}_D$ is the desired mass flow rate of the scaled map. $\dot{m}_{MD}$ is the mass flow rate at the design point of the original map. $\dot{m}_M$ is an arbitrarily selected mass flow rate from the original map. η_{Factor} is the efficiency factor that relates the original map and the scaled map. η_D is the desired efficiency of the scaled map. η_{MD} is the efficiency at the design point of the original map. η_M is an arbitrarily selected efficiency from the original map. Table 10 on the next page shows the data used to scale the compressor maps in this work.

Table 10 - Data for map scaling

Scaling Factor	Value
PR_D	69
PR_M	2.12
PR_{MD}	1.5632
$\dot{m}_D$	6.6
$\dot{m}_M$	20.8234
$\dot{m}_{MD}$	17.2907
η_D	85%
η_M	84.12%
η_{MD}	85.19%

Once these factors have been determined, each beta line obtained from the map is multiplied by its respective factor to obtain a new set of scaled beta lines. Figure 51 below and Figure 52 on the next page show the original map and scaled map respectively.

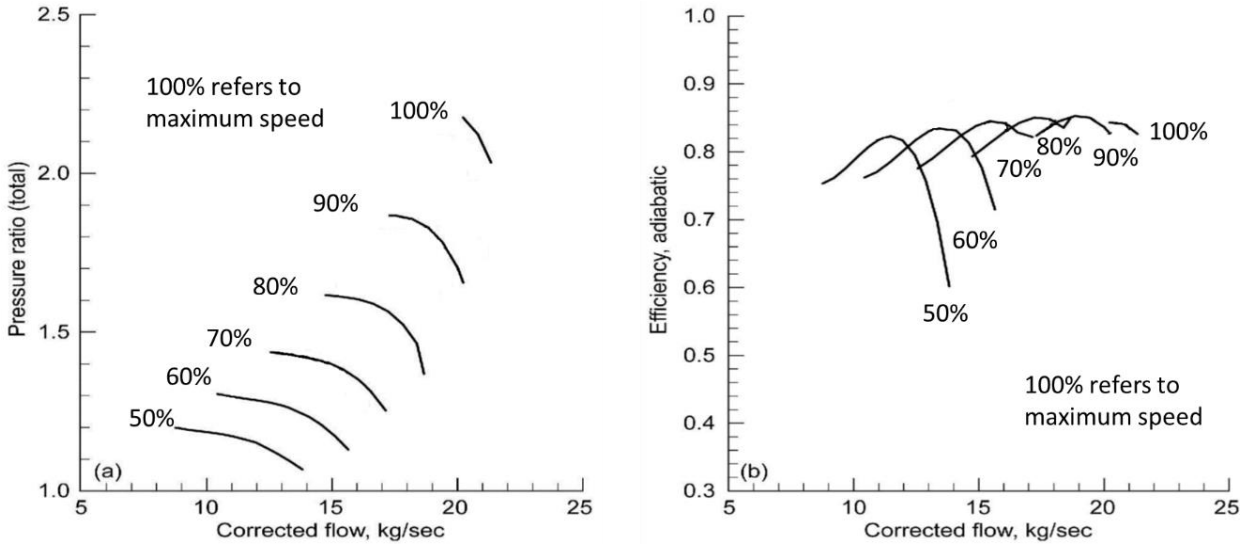

Figure 51 - NASA 37 Original compressor map [82]

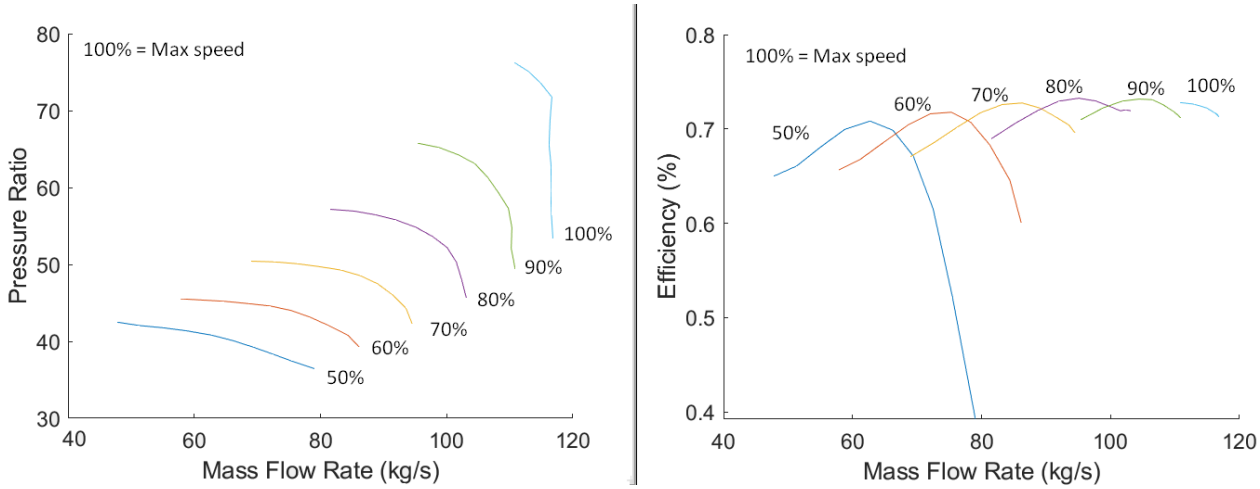

Figure 52 - NASA 37 Compressor map after scaling